THE PECULIAR SPIRAL GALAXY NGC 4258

high resolution radio observations and their interpretation

Geert Dick van Albada

THE PECULIAR SPIRAL GALAXY NGC 4258

high resolution radio observations and their interpretation

proefschrift

ter verkrijging van de graad van Doctor
in de Wiskunde en Natuurwetenschappen
aan de Rijksuniversiteit te Leiden,
op gezag van de Rector Magnificus Dr. D.J. Kuenen,
hoogleraar in de Faculteit
der Wiskunde en Natuurwetenschappen,
volgens besluit van het College van Dekanen
te verdedigen op woensdag 4 oktober 1978
te klokke 14.15 uur

door

Geert Dick van Albada
geboren te Bandung (Indonesië) in 1951

Sterrewacht Leiden

Promotor: Prof. H. van der Laan
Coreferent: Dr. W.W. Shane

Voor mijn moeder,
ter nagedachtenis aan mijn vader.

CONTENTS

The research described in this dissertation was supported by the NETHERLANDS ORGANISATION FOR THE ADVANCEMENT OF PURE RESEARCH (Z.W.O.) through a three year grant to the author.
Z.W.O. also financially supports the Netherlands Foundation for Radio Astronomy (SRZM) which operates the Westerbork Synthesis Radio Telescope.

CHAPTER 1 INTRODUCTION

This thesis is concerned with the large spiral galaxy NGC 4258. A number of observational parameters are listed in Table 1. The reason for undertaking this research was originally to be found in the very unusual radio-continuum and Hα structures found in the galaxy. Radio-continuum and HI observations have been made in order to obtain better insight into the properties of the system. Contrary to the original expectations the neutral hydrogen data provided very little information that seems to be directly connected to the continuum structure, but on the other hand features were found in the HI that are very interesting in their own right. In the following paragraphs I shall give a review of the literature concerning NGC 4258.

1. Discussion of the relevant literature

1) NGC 4258 is also known as M 106, though it was not originally included in Messier's catalogue; it is one of the galaxies that were later added by Méchain.

Table 1

Parameters for NGC 4258	Value		Reference
Right ascension of nucleus	$12^h16^m29^s.42$	(1950)	a
Declination of nucleus	$47^o34'53''.2$	(1950)	a
Distance	6.6 Mpc		b
Holmberg dimensions	24'× 9'.6		c
Position angle	-30^o		d
Inclination	72^o		d
Systemic velocity	450 km s^{-1}		d
Classification	SAB(s)bc		e
HI mass	4.4 10^9 $M_\odot$		d
1412 MHz continuum flux	0.82 ± 0.04 Jy		d
Total mass	2.0 ± 0.2 10^{11} $M_\odot$		d
Blue luminosity	3.0 10^{10} $L_\odot$		f,d

---

a Van der Kruit, Oort and Mathewson, 1972, quoting Schoenmaker

b Burbidge, Burbidge and Prendergast (BBP), 1963, quoting Sandage

c Holmberg, 1958

d This thesis, chapter 3

e De Vaucouleurs, De Vaucouleurs and Corwin (RCBG II), 1976

f Capaccioli, 1973

Therefore the galaxy is not always included in republications of the Messier catalogue. It was, evidently, included in Dreyer's (1890) New General Catalogue. A photograph of the galaxy is shown in Fig.15 of chapter 3. Photographs can also be found in Burbidge et al. (1963, henceforth BBP), Chincarini and Walker (1967), Capaccioli (1973), Holmberg (1937), Sandage (1961), Hubble (1943), Lindblad and Brahde (1946), de Vaucouleurs (1958), Courtès and Cruvellier (1961), Deharveng and Pellet (1970) and Courtès et al. (1965). The last three are Hα photographs.

2) Holmberg (1937) suggests in his catalogue of double and multiple galaxies that NGC 4258 and the much smaller edge-on spiral galaxy NGC 4248 form a double. This was later confirmed by the HI-radial velocity data on NGC 4248 of Van Albada (1977).

3) NGC 4258 is generally classified as a member of the UMa I cloud, which also contains NGC 4736, NGC 4295, NGC 4656, NGC 4449, NGC 4214 (Sérsic, 1960; also refer to Humason et al., 1956).

4) In 1942 Danver published a catalogue giving a morphological description of a large number of galaxies including NGC 4258. The spiral structure is described as irregular and no attempt is made to fit the arms with a logarithmic spiral, as is done in most other cases. Projection parameters are given for NGC 4258 (position angle = 157.5°, inclination = 64.4°) that differ considerably from later determinations using velocity data.

5) NGC 4258 has played an important role in the attempts to determine whether spiral arms are generally leading or trailing. The following papers deal with this subject:
- Hubble (1943), who concludes that spiral arms are trailing;
- Lindblad and Brahde (1946) conclude that they are leading;
- de Vaucouleurs (1958) again states that they are trailing.

In all these papers the same sense of winding was assumed for the arms of NGC 4258 as seen projected on the sky; the discussion centered on which was the near side of the galaxy. Hubble's and de Vaucouleurs' view that this should be the Western side is nowadays generally accepted. The arms referred to in these three papers, however, may well be part of a nearly circular ring-like structure so that the sense of winding would be undefined. But they certainly are not leading if the Western side is the near side, as I will assume throughout this thesis.

6) NGC 4258 is mentioned in a note in Seyfert's (1943) original paper on galaxies with a nucleus showing a U-V excess and broad emission lines, but no further references are given. NGC 4258 was not observed by Mayall (1939) as might be inferred from Seyfert's paper. Later authors rejected NGC 4258 from the list of true Seyfert galaxies on the basis of the rather too small width of the nuclear lines (350 km s^{-1} as compared to about 2000 km s^{-1} for true Seyferts; Burbidge and Burbidge, 1962)

7) In his classical paper (1958) Holmberg published the results of photographic photometry of a large number of galaxies including NGC 4248 and NGC 4258. His most relevant results on NGC 4258 have been included in Table 1.

8) The remarkable nature of NGC 4258 was discovered by Courtès and Cruvellier (1961). They discuss the use of a focal ratio reducer and interference filters in obtaining narrow band (60 Å at Hα) photographs of a number of objects. NGC 4258 exhibited a pair of unique gaseous filamentary arms. These arms contain no young blue stars; the excitation mechanism probably is shock excitation as in supernova shells. These anomalous arms seem to begin very close to the nucleus near the direction of the major axis, go out radially, bend in a trailing sense and cut through the main spiral arms at the edge of the bright "lens". These observations were confirmed by Courtès, Viton and Véron (1965) using a 6 Å wide Hα filter. On this narrow band photograph only one of the arms was visible. This indicated that the anomalous arms show velocities comparable to the rotational velocities in the galaxy itself and have a small internal velocity dispersion.

Deharveng and Pellet (1970) observed NGC 4258 using a two stage image intensifier and a 10 Å Hα filter. From their data they were able to give a quantitative estimate of the Hα emission: 7.7×10^{-8} W m^{-2} $sterad^{-1}$ at 90" from the nucleus in the S-W anomalous arm.

9) The true extent of the anomalous arms was only realized after the publication by Van der Kruit, Oort and Mathewson (1972, henceforth to be referred to as KOM) in which 21 cm continuum observations with the Westerbork Synthesis Radio Telescope (WSRT) are described. They found that in the radio continuum the anomalous arms are the dominant feature in the galaxy. (For a picture of the radio continuum structure see Fig.1 of chapter 2.) The anomalous arms extend all the way to the edge of the galaxy, cutting through all the normal spiral arms. As was already visible on the Hα photographs the anomalous arms are followed (in the sense of rotation of NGC 4258) by plateaux of enhanced emission. In front of the anomalous arms there seems to be a relative lack of emission, both in Hα and radio-continuum. The front edge of the anomalous arms is very steep; it is in fact unresolved in KOM's observations. The N-W anomalous arm is much brighter than the other. The S-W arm is the straighter of the two. The N-W arm splits at the edge of the lens. In Hα both arms can be seen to split, but here it is seen most clearly in the S-W arm.

The spectral index map derived by De Bruyn (1976, 1977) indicates that the radio emission of the anomalous arms is caused by synchroton radiation, as had already been assumed implicitly by KOM.

KOM concluded that the anomalous arms probably lie in the plane of NGC 4258 from a number of facts:

a. In Hα both arms are of comparable brightness, which leads to the conclusion that the extinction cannot be very different, as it would be if they lay on different sides of the plane.

b. The arms extend exactly to the edge of the observable disk.

c. From the data of Courtès et al. (1965) and from spectroscopic data obtained by Schmidt (also published by KOM) it was known that the anomalous arms partake in the rotation of the disk, though not necessarily with the same velocity.

d) At the positions of the anomalous arms the features in the normal arms generally seem a bit weaker.

KOM present two simple models based on the hypothesis that the anomalous arms are the result of the ejection of gas by the nucleus. It seems very well possible to explain the general shape of the anomalous arms in this manner. KOM suggest that we may be seeing the birth of a new set of spiral arms.

10) Fricke (1975) and Fricke and Reinhardt (1975) speculate on the role of supermassive stars in active galaxies such as NGC 4258. As we shall see in chapter 4 of this thesis it seems unlikely that such an object, which would be destroyed in its active phase, could have created the pattern of anomalous arms observed in NGC 4258.

11) In the years following the discovery of the anomalous arms a number of authors published spectroscopic observations of NGC 4258. So far no very consistent picture has emerged, and better and more uniform observations are needed. The best, and certainly the most extensive observations to date are those by Van der Kruit (1974). A large number of spectra have been obtained by him with dispersions of 190 and 144 Å mm^{-1}. Velocities have been determined from the Hα and the [NII] λ6583 lines. Van der Kruit subsequently determined a velocity field and a rotation curve from his measurements.

The following typographical errors have been noted in his published data:

Table 1:

i. δα is given in seconds, not in minutes.

ii. The values for δα for the spectra Q4110 and Q4121 are -1.5^s, $+1.5^s$, respectively, instead of -0.5^s and $+0.5^s$.

Table 2:

The sign of all offsets (d) for spectrum Q4132 must be changed; d then runs from

-27".4 to +26".7.

A number of other papers giving optical velocities are also available:

-- BBP published measurements of velocities derived from Hα, [NII] λ6583 and [SII] λλ6717, 6713 on a number of spectra through the nucleus with position angles between 126° and 169°. Their observations have a dispersion of 330 Å mm^{-1}. According to De Vaucouleurs et al. (1976, Second Reference Catalogue of Bright Galaxies = RCBG II) their velocities are approximately 30 km s^{-1} too high, an estimate that agrees well with my own estimate of 35 km s^{-1} from comparison with other authors and the HI data. BBP also give a new distance of 6.6 Mpc for NGC 4258, determined by Sandage. This distance will be used in all distance dependent quantities throughout this thesis.

-- Duflot (1965) has obtained one spectrum (position angle = 160°, dispersion = 170 Å mm^{-1}) of NGC 4258. She gives velocities determined from Hα, [NII] λ6583 emission lines and from the K (CaII, λ3933) absorption line. (These K-line measurements are the only velocity determinations available for the stellar component to date.) All velocities are consistent, and agree well with the measurements of BBP. Though the RCBG II states that no correction needs to be applied to Duflot's velocities, I find a better consistency with the other measurements if they are lowered by 30 km s^{-1}.

-- Chincarini and Walker (1967) have obtained two sets of spectra in position angles 148° and 58°. One set was made using direct photography and has a dispersion of 96 Å mm^{-1}; the other set was obtained with the Lallemand electronic camera and has a dispersion of 48 Å mm^{-1}. The authors measured the [OII] λλ3726, 3729 doublet. The two spectra in p.a. 148° are not mutually consistent, but those in p.a. 58° are. The velocities of Chincarini and Walker do not seem to be in very good agreement with the velocities determined by other authors. This may be due to the fact that a doublet was measured. Chincarini and Walker also give some photoelectric photometry through diaphragms 17" to 138" in diameter.

-- De Vaucouleurs and De Vaucouleurs (1967) give the redshift for NGC 4258. They state that more extensive measurements of NGC 4258 were to be published. No such publication has been found.

-- Courtès (1972) reports on a number of measurements of velocities from an Hα interferogram. His measurements undoubtedly are the most accurate optical velocity determinations to date. In this case the principal source of uncertainty seems to lie in the manner of publication. The positions where the velocities were measured are given with an accuracy of only 10" in right ascension. The measured velocities themselves are not given; only the velocities that were obtained after an unspecified transformation made in order to allow comparison in a graph with the data obtained in p.a. 148° by Chincarini and Walker. Using the projection parameters of Danver I find that the specified sky coordinates of the measured points convert reasonably well to the distances from the nucleus used in the graph. Some significant differences remain, however. The conversion thus being unknown, the observed velocities cannot be reconstructed.

-- As mentioned previously the paper by KOM contains some velocity data obtained by Schmidt. These data have been obtained in the same way as those of Van der Kruit.

12) High resolution HI observations were published by Van Albada and Shane (1975). Their publication is entirely superseded by this thesis. Evidence for large deviations from circular rotation was indeed found, as well as a lack of HI in the anomalous arms.

13) Photometric observations of the nuclear region have been published by a number of authors. Photometry of the entire disk has been published only by Capaccioli (1973) and by Holmberg (1958). The latter author gives only integrated quantities. Capaccioli presents both a contour map of the blue magnitude and a graph of the blue magnitude versus equivalent radius. Capaccioli finds a break

in the variation of blue magnitude with equivalent radius that is unusual for an Sbc galaxy. This break is, however, often found in galaxies containing a bar-like structure. In such systems the brighter inner region, or "lens", has an oval form. If the position angle and inclination determined from the velocities in the HI for the outer parts of NGC 4258 (position angle = -30°, inclination = 72°) also hold for the lens then it must be concluded that the lens indeed is an oval structure since Capaccioli finds p.a. = -24°, i = $65^{\circ}.2$ from its outline, in good agreement with the value of Danver. (On photographs the lens is easily recognized: it is the bright inner region bounded by the bright "normal" spiral arms.) Inside the lens a narrower structure is visible, reminiscent of a true bar. NGC 4258 is indeed classified SAB(s)bc in RCBG II and Bosma (1978) states that, but for the anomalous arms, the velocity field of NGC 4258 would make it "the type example of an oval distortion in a spiral galaxy" (p.127).

Capaccioli's estimate of the nuclear luminosity is much too high when compared with the available photo-electric photometry. Such photometry has been published by the following authors:

-- Chincarini and Walker (1967): V and B through 17", 25", 28", 59" and 138" diaphragms.

-- McClure and Van den Bergh (1968): five colour intermediate band photometry of a large number of objects, including the nucleus of NGC 4258. 40" diaphragm.

-- Wisniewsky and Kleinmann (1968): UBVRI photometry of a number of Seyfert galaxies and NGC 4258. 27".3 and 54".2 diaphragms were used. Their observations confirm that NGC 4258 has a marked U-V excess.

-- Stebbins and Whitford (1952): photometry of 176 galaxies in the "international system". The data on NGC 4258 are incomplete.

14) Rieke and Lebofsky (1978) report on 10μ observations of a number of bright galaxies. They find 40% detections, including NGC 4258. A 10μ flux of 0.1 ± 0.012 Jy was found, presumably coming from the nuclear region. Though many galaxies, such as M 31, have a much smaller 10μ luminosity, NGC 4258 is not abnormally bright at 10μ. The emission cannot be stellar in origin. With this 10μ flux NGC 4258 fits nicely into the relation between 10μ and 1415 MHz power of the nucleus discussed by Van der Kruit (1973).

15) Pronik (1970) has measured the ratio of Hα to [NII] in the nuclei of a number of galaxies. He finds $I_{H\alpha}/I_{6584} = 0.3$ for NGC 4258, the smallest value measured among the seven "normal" galaxies he observed.

16) The optical emission by the nucleus of NGC 4258 is not polarized (Dombrovsky and Hagen-Thorn, 1968).

17) Beside the 21 cm continuum observations of KOM and the HI observations of Van Albada and Shane radio observations have been published by a number of authors. These observations have generally been obtained with single dish instruments, or short base-line interferometers, so that NGC 4258 is only seen as a point source. Most continuum observations near 1400 MHz must have been contaminated with HI emission (chapter 3, section 1). Observations at other frequencies have been published by the following authors, among others: Braccesi et al. (1967: 408 MHz, 1.3Jy), De Bruyn (1976, 1977: 610 MHz, 1.4Jy and 5 GHz, no flux determined; measurements obtained with the WSRT), De Jong (1965: 750 MHz, 1.1Jy and 1410 MHz; 1967: 2695 MHz, 0.42Jy), Heeschen and Wade (1964: 750 MHz, 1.0Jy; 1400 MHz), Kazès et al. (1970: 2695 MHz, ≥0.46Jy), Sramek (1975: 5 GHz, 0.25Jy). At the higher frequencies resolution effects may have lead to a systematic underestimation of the flux.

The total radio-continuum power is of the order of $4\ 10^{30}$ W, which leads to an emitted energy totalling $5\ 10^{45}$ J in $4\ 10^{7}$ years. De Bruyn (1976, 1977) estimates that the total energy in the magnetic field and the relativistic particles at this moment is in the range of a few times 10^{47} J.

The radio-continuum power thus is very small when compared to that emitted

in the Hα line alone. This emission amounts to something of the order of $1.5\ 10^{33}$ W, or $2\ 10^{48}$ J in $4\ 10^{7}$ y, corresponding to $2\ 10^{7}\ M_{\odot}$ at 300 km s^{-1}.

HI observations with the 2 element Owens Valley radio interferometer have been obtained by Rogstad et al. (1967). Their measurements for NGC 4258 are incomplete.

2. The contents of this thesis

Chapter 2 contains a description of the HI line and the 1412 MHz continuum observations that were obtained with the WSRT and the 100 m telescope of the Max Planck Institut für Radioastronomie in Bonn. The reduction procedures followed are described and a collection of HI maps is presented.

An analysis of the observations that are connected with aspects of NGC 4258 as a fairly normal spiral galaxy can be found in chapter 3. It is demonstrated that both the HI distribution and velocity field are in agreement with the assumption that NGC 4258 is a barred spiral.

In chapter 4 the observations of the anomalous arms are discussed. It is shown that the observational material nowhere contradicts the expulsion hypothesis, but that the isolation of effects that are attributable to the anomalous arms is made difficult by the incomplete understanding of the underlying galaxy. Certain parallels between NGC 4258 and some other types of active galaxies are drawn.

Chapter 5 is a theoretical chapter concerned with the analysis of HI data of a spiral galaxy, and with the effects that the spiral structure will have on the observations. Much of the material in that chapter is not new, but included for the sake of completeness.

In chapter 6 the stability aspects of a very simple model for a cloud moving at supersonic velocities through a dense medium are analyzed. The consequences of this analysis for models of active galaxies like NGC 4258 are discussed briefly.

The conclusions of this thesis are summarized in chapter 7 and some suggestions for further research are given.

References.

Albada, G.D. van: 1977, *Astron. Astrophys. 61*, 297

Albada, G.D. van; Shane, W.W.: 1975, *Astron. Astrophys. 42*, 433

Bosma, A.: 1978, Ph.D. dissertation, University of Groningen

Braccesi, A.; Fanti-Giovanni, C.; Fanti, R.; Formiggini, L.; Vespignani, G.: 1967, *Nuovo Cim. 52 B*, 254

Bruyn, A.G. de: 1976, Ph.D. dissertation, Leiden University

Bruyn, A.G. de: 1977, *Astron. Astrophys. 58*, 221

Burbidge, E.M.; Burbidge, G.R.: 1962, *Astrophys. J. 135*, 694

Burbidge, E.M.; Burbidge, G,R.; Prendergast, K.H.: 1963, *Astrophys. J. 138*, 375

Capaccioli, M.: 1973, *Mem. del. Soc. Astron. It. 44*, 417

Chincarini, G.; Walker, M.F.: 1967, *Astrophys. J. 149*, 487

Courtès, G.: 1972, *Compt. Rend. Acad. Sci. Paris 275, Serie B*, 759

Courtès, G.; Cruvellier, P.: 1961, *Compt. Rend. Acad. Sci. Paris 253*, 218

Courtès, G.; Viton, M.; Véron, P.: 1965, *Quasi Stellar Sources and Grav. Collapse*, ed. Robinson et al., Univ. of Chicago Press, Chicago, p.307

Danver, C.G.: 1942, *Ann. Obs. Lund 10*

Deharveng, J.M.; Pellet, A.: 1970, *Astron. Astrophys. 9,* 181
Dombrovsky, V.A.; Hagen-Thorn, V.A.: 1968, *Astrofisika 4,* 409
Dreyer, J.L.E.: 1888, *New General Catalogue, Mem. R.A.S.,* republished 1953, Royal Astron. Soc., London
Duflot, R.: 1965, *J. des Obs. 48,* 247
Fricke, K.J.: 1975, *Mitt. Astron. Ges. 36,* 86
Fricke, K.J.; Reinhardt, M.: 1975, *Naturwissensch. 62,* 309
Heeschen, D.S.; Wade, C.M.: 1964, *Astron. J. 69,* 277
Holmberg, E.: 1937, *Ann. Obs. Lund no. 6*
Holmberg, E.: 1958, *Medd. Lunds Astron. Obs., Serie II,* 136
Hubble, E.: 1943, *Astrophys. J. 97,* 112
Humason, M.L.; Mayall, N.U.; Sandage, A.R.: 1956, *Astron. J. 61,* 97
Jong, M.L. De: 1965, *Astrophys. J. 142,* 1333
Jong, M.L. De: 1967, *Astrophys. J. 150,* 1
Kazès, I.; Squéren, A.M.; Nguyen-Quang-Rieu: 1970, *Astrophys. L. 6,* 193
Kruit, P.C. van der: 1973, *Astron. Astrophys. 29,* 263
Kruit, P.C. van der: 1974, *Astrophys. J. 192,* 1
Kruit, P.C. van der; Oort, J.H.; Mathewson, D.S.: 1972, *Astron. Astrophys. 21,* 169
Lindblad, B.; Brahde, R.: 1946, *Astrophys. J. 104,* 211
Mayall, N.U.: 1939, *Lick Obs. Bull. 19,* 33
McClure, R.D.; Bergh, S. van den: 1968, *Astron. J. 73,* 313
Messier, C.: 1784, *Connaissance du Temps,* p.227
Pronik, I.I.: 1970, *Sov. A. J. 13,* 593
Rieke, G.H.; Lebofsky, M.J.: 1978, *Astrophys. J. 220,* 37 L
Rogstad, D.H.; Rougoor, G.W.; Whiteoak, J.B.: 1967, *Astrophys. J. 150,* 8
Sandage, A.: 1961, *The Hubble Atlas of Galaxies,* Carnegie Inst. of Washington
Sérsic, J.L.: 1960, *Z. Astrophys. 50,* 168
Seyfert, C.K.: 1943, *Astrophys. J. 97,* 28
Sramek, R.A.: 1975, *Astron. J. 80,* 771
Stebbins, J.; Whitford, A.E.: 1952, *Astrophys. J. 115,* 284
Vaucouleurs, G. de: 1958, *Astrophys. J. 127,* 487
Vaucouleurs, A. de; Vaucouleurs, G. de: 1967, *Astron. J. 72,* 730
Vaucouleurs, G. de; Vaucouleurs, A. de; Corwin, H.G. Jr.: 1976, *Second Reference Catalogue of Bright Galaxies,* Univ. of Texas Press, Austin & London
Wisniewsky, W.Z.; Kleinmann, D.E.: 1968, *Astron. J. 73,* 866

CHAPTER 2 THE OBSERVATIONS *

Summary

In this chapter the results of 21 cm line and continuum observations of NGC 4258 *obtained with the Westerbork Synthesis Radio Telescope* (WSRT) *and the 100 m telescope of the Max Planck Institut für Radioastronomie in Bonn* (MPIfR) *are presented. The reduction of the data is described. An analysis of the data presented here will be given in chapters 3 and 4.*

1. Introduction

In their 1972 paper Van der Kruit et al. (henceforth KOM) described 21 cm continuum observations of NGC 4258 in which the most striking feature proved to be a pair of anomalous arms that cut nearly radially through the entire disk of the galaxy. Parts of the arms had previously been observed by Courtès et al. (1961) in Hα. Neutral hydrogen observations were described by Van Albada et al. (1975). The data in that article have been supplemented by new observations with lower noise. The result is presented in this chapter together with an entirely new set of 21 cm continuum observations. Observations have been obtained with the WSRT and with the 100 m telescope of the MPIfR in Bonn. Those done with the latter instrument have been made by Dr. R.H. Harten, who has also been partly responsible for their reduction.

In this chapter the data and their reduction will be described; an analysis of the HI and continuum data will be given in chapters 3 and 4. In the interest of clarity the reduction of each of the different sets of observations will be described separately, though the actual reduction procedure followed was slightly more complicated, as it proved necessary to apply some of the corrections after all data had been combined.

2. The WSRT observations

Two separate series of 21 cm line observations of NGC 4258 have been obtained with the WSRT. One set dates from 1972 and was described by Van Albada et al. (1975), the other dates from 1974. Although the continuum observations were made during two separate observing periods they may be regarded as one set having the same characteristics. Table 1 contains a catalogue of the WSRT observations. For a description of the WSRT system and the 80 channel line receiver the reader is referred to Baars et al. (1974) and Allen et al. (1974). The continuum receiver is described by Casse et al. (1974). However, the front-ends described in their paper have been replaced by front-ends with a lower system temperature.

The phase drift effect in the line observations described by Van Someren-Gréve has not been corrected for in any way as it does not significantly affect the observations. It is a velocity-dependent shift of all positions which in these observations never exceeds 0".2.

2.1 The 1972 line observations

These observations encompass 5 velocity combs, giving a velocity coverage from +40 km s^{-1} to +960 km s^{-1} with an increment of 20 km s^{-1} between +160 km s^{-1} and

* This chapter has been submitted for publication in *Astron. Astrophys. Suppl.* as the first of a series of papers on NGC 4258.

+800 km s^{-1} and 40 km s^{-1} outside this range. (All velocities quoted in this paper are heliocentric). Due to receiver instabilities certain interferometers in some velocity channels had to be deleted. In the original reduction, in which the continuum measurements of KOM were used to subtract the continuum contribution, a matching continuum map was calculated for each of the velocity channels with an incomplete set of interferometers. In this way the continuum contribution was subtracted correctly, but the coverage of the U,V plane for the H I emission remained incomplete. Examination of the resultant maps and antenna patterns indicated that noise, and not dynamic range, was still the limiting factor in these maps so that no further corrections were applied.

In the subsequent reduction the KOM continuum map was replaced by a better continuum map by subtracting an appropriate difference map (new continuum − KOM continuum) from the maps of the H I emission. Here no distinction was made between the maps with an incomplete U,V coverage and the other maps. The continuum map that was effectively subtracted from the maps published here consists of a weighted average of the 21 cm continuum as observed by KOM (∿ 4%), my own 1976 continuum measurements (∿ 87%) and the mean of the 14 line maps outside the range of

Table 1a The 1972 WSRT line observations.
75 K front-ends in Tel A and B.
260 K front-ends in the fixed telescopes.

Obs. date (YYDDD)	Velocities (km s^{-1})	Spacings (m)	Remarks
72089	40(40)320	36 (72) 684	
72091	180(40)460	"	1
72093	360(40)640	"	
72095	500(40)780	"	
72097	680(40)960	"	
72115	40(40)320	72 (72) 720	2
72117	180(40)460	"	3
72119	360(40)640	"	
72121	500(40)780	"	4
72123	680(40)960	"	5
72135	40(40)320	792 (72)1440	
72137	180(40)460	"	
72139	360(40)640	"	
72141	500(40)780	"	
72143	680(40)960	"	
72146	40(40)320	756 (72)1404	
72148	180(40)460	"	
72150	360(40)640	"	
72152	500(40)780	"	
72154	680(40)960	"	

Remarks:
1. 180 m spacing missing at 380 kms^{-1}
2. 216 and 288 m spacings missing at 240 kms^{-1},
288 m missing at 320 kms^{-1}.
3. 216 and 288 m spacings missing at 380 kms^{-1},
288 m missing at 460 kms^{-1}.
4. 504 and 576 m spacings missing at 660 kms^{-1}.
5. 216 m spacing missing at 960 kms^{-1},
576 m spacing missing at 840 kms^{-1}.

Table 1b The 1974 WSRT line observations. 85 K front-ends in all telescopes, except sometimes in Tel.5.

Obs. date (YYDDD)	Velocities (km s^{-1})	Spacings (m)	Remarks
74198	160(40)440	90(72)738	1
74203	"	"	2, 3
74204	"	"	2, 4
74205	"	"	2, 5
74199	180(40)460	"	
74200	480(40)760	"	
74201	500(40)780	"	6
74202	"	"	2, 7
74205	"	"	2, 8
74206	160(40)440	54(72)702	
74207	180(40)460	"	
74208	480(40)760	"	2
74211	500(40)780	"	2
74336	160(40)440	810(72)1458	
74337	180(40)460	"	
74338	480(40)760	"	
74339	500(40)780	"	
74341	160(40)440	774(72)1422	
74342	180(40)460	"	
74343	480(40)760	"	
74344	500(40)780	"	

Remarks:
1. Observation interrupted, only the hour angles -90 to -61 degrees and -11 to +71 degrees were observed.
2. 260 K front-end in Tel 5. (Longest base line and longest less 72 m)
3. Hour angles +73 to +90 degrees.
4. Hour angles +71 to +90 degrees.
5. Hour angles -61.5 to -12 degrees.
6. All interferometers with telescope B were observed only from -90 to -6 degrees. Hour angle coverage with Tel A was complete.
7. Hour angles +13 to +89.5 degrees.
8. Hour angles -10 to +89.5 degrees.

Table 1c The 1975 and 1976 continuum observations. 85 K front-ends in all telescopes.

Obs. date (YYDDD)	Frequency (MHz)	Spacings (m)	Remarks
75223	1412	54(72)1422	
75230	"	90(72)1458	
76113	"	72(72)1440	
76136	"	36(72)1404	1

Remarks:
1. In this observation the 3YAX channel, with a spacing of 900 m had to be deleted.

+200 km s^{-1} to +700 km s^{-1} ($\sim$ 9%).

Since the line and the continuum maps were observed at slightly different frequencies the effective antenna pattern of the WSRT is somewhat different. There is even a slight difference in antenna pattern between line maps at opposite ends of the observed velocity range. The largest difference is in the position of the grating lobes. Therefore it was necessary to subtract those continuum sources whose grating lobes were above the noise and crossed the region where H I radiation was expected from both the line and the continuum maps using the appropriate antenna patterns. The sources subtracted are the first four sources listed in Table 2.

One more effect that had to be taken care of was a spurious pattern, slightly above the noise, that appeared in the center of each map. It was caused by D.C. offsets in the correlators of the WSRT. These offsets proved to be equal for all correlators to within 30%. (R.S. le Poole, private communication). The phase and gain corrections were nearly equal for all velocity channels for each interferometer spacing, so that the resultant spurious patterns in the line maps were all very similar. Since the effect was not very large it virtually disappeared if any significant differential phase rotation was applied to the D.C. offset of an interferometer. (This technique was used to eliminate the effect in all observations from 1973 onwards). This implied that only the D.C. component that remained after all corrections had been applied was of actual importance in causing the spurious pattern. Therefore I determined this component from the mean difference between the 1976 continuum observations and the "empty" line observations for each interferometer spacing and for the sine and cosine channels separately. Using these mean D.C. offsets a map showing only the spurious pattern and containing virtually no noise was constructed. This map was used to eliminate the spurious pattern from the H I-emission maps, of course only in so far as this had not yet been done by the inclusion of the empty line maps in the subtracted continuum map.

2.2 The 1974 line observations

Because all the outer velocity channels in the earlier observations had proved to be devoid of hydrogen it was decided to observe only four velocity combs this time, giving a velocity coverage from 160 km s^{-1} to 780 km s^{-1} with a velocity increment of 20 km s^{-1} . The reduction of these observations was relatively straightforward since all observations had a complete set of interferometer

Table 2

Subtracted sources.

	α	δ	Φ(mJy)
1	$12^h14^m31^s.450$	$47^\circ31'51''.276$	39.15
2	12 14 46.668	47 28 53.292	42.55
3	12 16 27.350	47 59 57.264	12.95
4	12 18 16.123	47 26 9.024	19.55
5	12 16 50.952	47 46 49.440	6.15
6	12 17 36.674	47 38 25.368	8.70
7	12 17 48.521	47 56 4.560	7.15

Positions and fluxes of the sources were determined from KOM's 21 cm continuum measurements (Willis et al., 1976). The subtracted fluxes are those of the sources as seen by the WSRT, i.e. attenuated by the primary beam.

spacings. As can be seen from Table 1b certain spacings were, at least in part, observed with a higher noise front-end. It would have been possible to obtain a somewhat lower noise (about 10% improvement) than in the maps published here by judiciously giving appropriate weights to all observations before doing the fourier transform to the map plane. This would have resulted in maps having a very irregular antenna pattern, which would have to be cleaned and restored (Högbom (1974), Harten (1974)) before even a continuum map could be subtracted. This method would have been exceedingly laborious. (Extra observations would have been a better and cheaper way to reduce the noise). The subtracted continuum map was derived from the 1975 continuum observations (∿92%) and from the average of the six line maps in this set of observations that showed no H I (∿8%). The seven sources listed in Table 2 were subtracted from the continuum and line observations before doing the fourier transform to the map plane.

2.3 The WSRT continuum observations

The continuum observations were made at a frequency of 1412 MHz in order to make sure that no emission due to H I could cause contamination of the observations. The use of a non-standard frequency resulted in fewer calibration observations being available. With some difficulty it was possible to obtain calibrations that were sufficiently good to allow subtraction of the continuum map from the line observations and the determination of the spectral index between 21 and 50 cm, since in both these cases the actual limitations came from the noise in the other maps. The 21 cm continuum maps do, however, suffer visibly from dynamic range limitations.

In one 12^h period the 3YAX interferometer could not be used. (The "X" and the "Y" indicate the dipole used in Tel. 3 and Tel. A respectively). Since in the configuration of the dipoles used in continuum observations the Stokes "V" is found from the combination XX+YY-XY-YX, and since, as expected, no circular polarisation was found, the 3YAX interferometer was replaced by the combination 3XAX+3YAY-3XAY when necessary. A number of different maps was derived from the observations.

1) For subtraction from the line observations, maps were made using only the XX and YX interferometers. This was done because the continuum radiation of NGC 4258 is slightly polarized (chapter 4) so that it was necessary to construct a continuum map with the same polarization characteristics as the line observations in which only one dipole per telescope was used. The 40% increase in the noise in the continuum map resulting from the use of only half of the interferometers affects all HI maps and combinations thereof, such as the integrated HI map, much less than the noise contribution of the line observations.

2) A set of 4 maps of all Stokes parameters was made using all observed interferometers. Spacings of 0 m and 18 m derived from the measurements with the 100 m telescope were included in the "I" map. From the "I" map the seven sources listed in Table 2 were subtracted. The "I" map was subsequently cleaned. It was restored with the central peak of the synthesized beam. Because of the much lower signal present in the "Q" and "U" maps cleaning and restoring was not necessary for these. The "V" map was indeed empty and was used for determining the noise in the observations (1σ = 0.15 K). The "I", the "Q" and the "U" map were subsequently corrected for the primary beam of the WRST antennae. The same pattern was assumed for all three maps, though it seems probable that the correction applied is strictly valid only for the "I" map. Since, however, the correction is rather small in the region where 21 cm continuum radiation of NGC 4258 was observed, and since the corrections that should have been applied to the "Q" and "U" maps certainly are equal to the first order to that for the "I" map, no serious error has been introduced in this manner. The "I" map is shown in Fig. 1. Other maps derived from the continuum data will be presented in chapter 4.

3. The observations with the 100 m telescope

Fig. 2 indicates the essential parts of the receiver configuration that was used for the observations with the 100 m telescope. It is a slightly modified Dicke

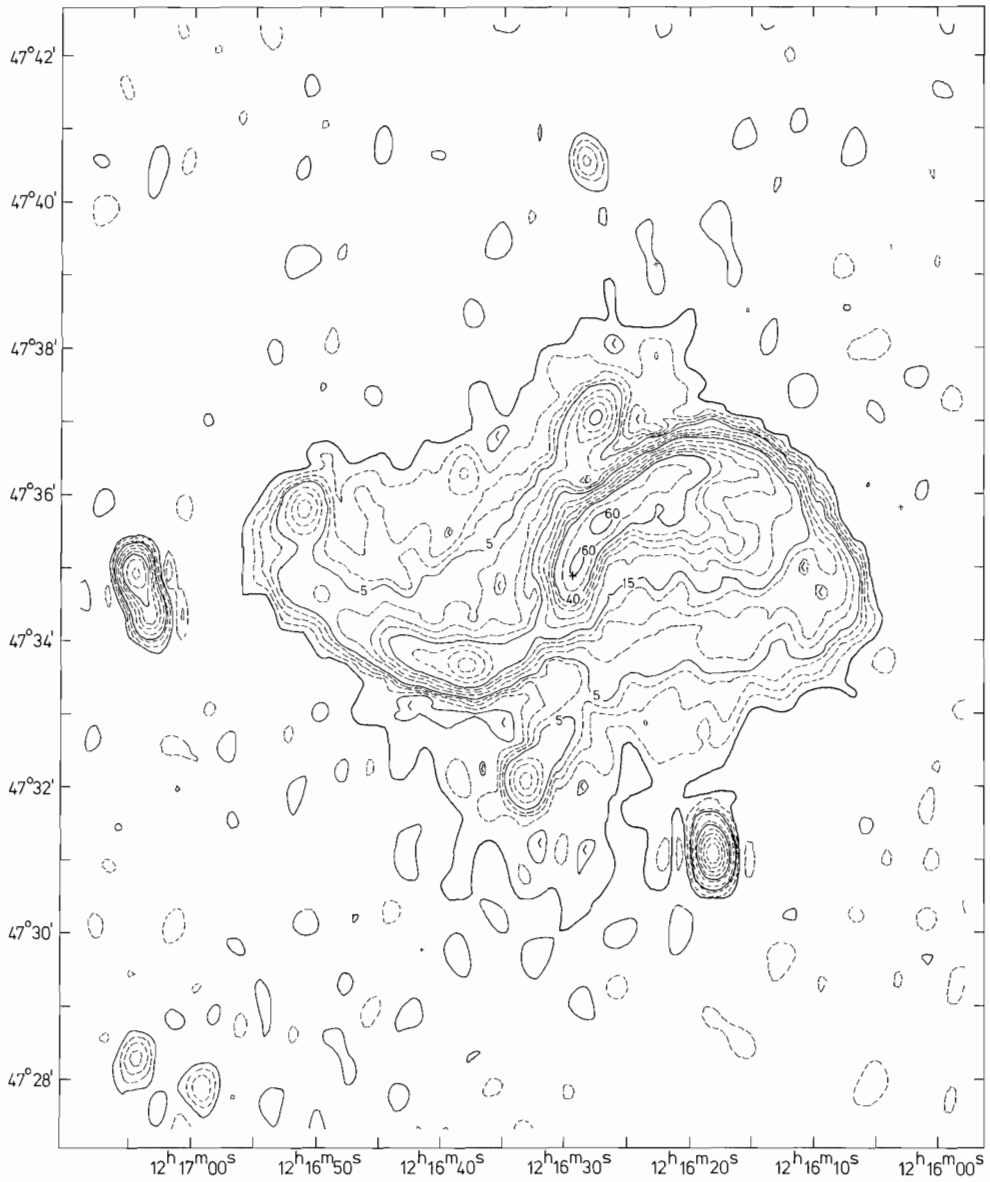

Figure 1.

The full resolution 1412 MHz continuum map. The map has been corrected for the attenuation of the WSRT primary beam. The full drawn contours are labelled in units of 0.333 K (2.2 σ). The dashed contour lines have been drawn at regular intervals between these, i.e. at (2, 3, 4; 7.5, 10, 12.5; 20, 25, 30, 35; 50) × 0.333 K. Relative minima have been marked with a "<". Negative contours are also dashed, they lie at (-1, -2) × 0.333 K. The nucleus has been marked with a "+".

switch system. The parameters for the observation are listed in Table 3. The passbands for the back-ends were shifted by 22 km s^{-1} relative to each other, so that they overlapped almost entirely. In this way the noise contribution due to the I.F. system was lowered.

A measuring sequence of 9 s consisted of four equal intervals during which different quantities were measured:

$(\overline{T}_{ant} + T_{bal} + T_{sys}) \times G \equiv$ CSF (1^{st} interval) (1)

$(\overline{T}_{ant} + T_{bal} + T_{sys} + T_{cal}) \times G \equiv$ CSN (2^{nd} ") (2)

$(T_{ref} + T_{sys}) \times G \equiv$ CRF (3^{rd} & 4^{th} ") (3)

$\{2 \times (T_{ant,i} + T_{bal} + T_{sys}) + T_{cal}\} \times G \times F_i \equiv SIG_i$ (1^{st} & 2^{nd} ") (4)

$2 \times (T_{ref} + T_{sys}) \times G \times F_i \equiv REF_i$ (3^{rd} & 4^{th} ") (5)

($\overline{T}_{ant}$ = antenna temperature averaged over all channels; T_{bal} was adjusted so that $\overline{T}_{ant} + T_{bal}$ averaged over a scan would be approximately equal to T_{ref}; G = overall gain (except for the antenna gain); F_i is the filter gain for the i^{th} velocity channel).

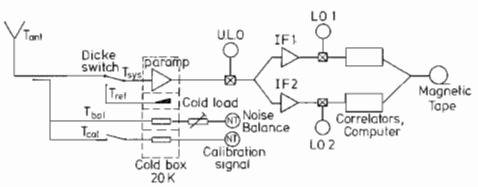

Figure 2.

Schematic drawing of the line receiver used in the 100 m telescope of the MPIfR in Bonn. The drawing is intended as a guide to the meaning of the measured quantities and not in any way as an exact representation of the receiver system.

Table 3

Parameters for the 100 m observations:

FWHPB in elevation	9!0
FWHPB in azimuth	8!8
T_{sys}	50 - 60 K
T_{cal}	5.8 K
LO1	45 MHz
LO2	45.104 MHz
ULO	89.547821 MHz × 15
Channel spacing	5.5 km s^{-1}
Number of channels	2 × 200
Number of channels used	2 × 168
Velocity of center of passband	
rec. 1	442 km s^{-1} (Heliocentric)
rec. 2	420 km s^{-1} (Heliocentric)
Integration time per point	½ × 9s (for single Dicke switch)
Observation date	June 24-25 1974

The measurements consisted of two separate observing runs on an area of the sky bounded by $\alpha = 12^h\ 13^m.1$ and $\alpha = 12^h\ 17^m.8$ and by $\delta = 46^0\ 59'$ and $\delta = 43^0\ 11'$. The runs were made with different focus settings ($\pm\ \lambda/3$) in order to compensate for interference effects between the primary and secondary mirrors and the feed of the telescope that would have caused a frequency-dependent ripple in the gain and the zero level. Analysis of the data indicated that:

a. T_{cal} showed slow 5% variations during one observing run, which may be attributable to a cold solder joint that was later found. For the other run no variations exceeding 2% were found. Variations up to 0.5% were present on short time scales during both runs.

b. CRF and (CSN - CSF) both showed a 10% drift during both runs. As the time dependence of the variations in these quantities showed the same behaviour, these variations were probably caused by a drift in G. CRF, however, was much more stable on short time scales. (Less than 10^{-3} variation from point to point).

c. From the reduced data evidence was also found for variations in T_{bal} and in the form of the passband, i.e. in F_i. The latter variation may have adversely affected the continuum map, which was also derived from these observations.

As it proved to be impossible to derive a sufficiently accurate instantaneous gain from (CSN - CSF) $\times\ T_{cal}^{-1}$, while $(T_{ref} + T_{sys})$ was quite stable, but not accurately known, it was decided to calculate G in the following way:

The time averaged gain is given by (<x> denotes a time average of x)

$$\langle G \rangle = \frac{\langle CSN - CSF \rangle}{T_{cal}} \quad , \tag{6}$$

which can be converted to the instantaneous gain

$$G = \langle G \rangle \times \frac{CRF}{\langle CRF \rangle} \simeq \frac{CRF}{T_{cal}} \times \left\langle \frac{CSN - CSF}{CRF} \right\rangle \quad . \tag{7}$$

The filter gain can be corrected for in the following way:

$$SIG'_i = \langle CRF \rangle \times \left(\frac{SIG_i}{REF_i} - 1 \right) \quad , \tag{8}$$

where the subtraction of 1 serves as a first order correction to the zero level, so that, except for a fairly small zero level error, nearly independent of channel and time, the antenna temperature is given by:

$$T_{ant,i} \simeq SIG'_i / G \tag{9}$$

The time averages occurring in these formulae were taken over all points in a run for the determination of the continuum map, so that no steps occurred in the correction for (filter) gain and especially in the zero level. For the line profiles the continuum level was of no interest so that a zero level could be determined for each profile separately, and small steps in the gains were unimportant. Therefore the scans were split into groups of one hundred points and the averages were taken over these groups. Having thus determined the antenna temperatures and before any correction was applied to the zero level the data were regridded to a regular grid and added. The regridding procedure involved convolution with a Gaussian beam with 9' × 9' and 7' × 7' full width to half power for the line and the continuum respectively so that the effective observing beam became a 12!6 × 12!6 or 11!5 × 11!5 FWHP beam. Subsequently the exact zero level had to be determined. For the line this was done by determining, from a sufficiently large number of profiles, in what velocity ranges no HI was detectable. Now a straight, sloping base line could be determined and subtracted for all profiles separately. All profiles also contained emission due to local galactic hydrogen on the low velocity side. This part of the profiles was deleted. The profiles were then convolved to the WSRT velocity resolution and converted to sky maps corresponding to the velocity channels observed with the WSRT. In these maps the regions showing no HI emission were located and used for a last correction of the zero level. The continuum map was determined from the averages of those parts of the profiles that did not show evidence for HI emission in any of the profiles. Since the observing runs

consisted of subscans at constant declination it was assumed that the zero level varied linearly with right ascension for each series of points at a constant declination. It proved to be possible to obtain a good estimate for the zero level for nearly all such series, but for a few the continuum emission was so extended that it was not possible to be sure that the assumed zero level was correct. The integrated flux in the map, however, agrees very well with the values found in the literature (0.9 ± 0.1 Jy).

At this point a correction for the antenna gain was applied, derived by Dr. R.H. Harten from observations of the standard region S8. (Harten et al., 1975).

From the sky maps thus obtained imitation WSRT observations were constructed using an adaptation of a program originally developed by E. Bajaja (Bajaja and Van Albada, in preparation). This program corrects for the beam of the observing instrument and for the primary beam of the WSRT. The interferometer spacings for which these calculations were performed are 0.225 m, 18 m and 36 m. The two shortest spacings served to supplement the WSRT observations and to make the coverage of the center of the U,V plane complete. The 36 m spacing was compared with the corresponding WSRT observation. The data proved to be very nearly equal for the HI data. For the continuum data this agreement was not quite so good. This cannot be explained by the fact that only one polarisation was observed, the percentage polarisation in NGC 4258 is much too small for that; the explanation is to be found in the much larger uncertainties in the reduction procedure.

Since they contain no continuum emission the maps derived from the line data were used to supplement the HI emission maps rather than the line maps still containing continuum emission. In the HI maps no effects due to incorrect incorporation of the 0.225 m and 18 m baselines could be found, even after strong convolution.

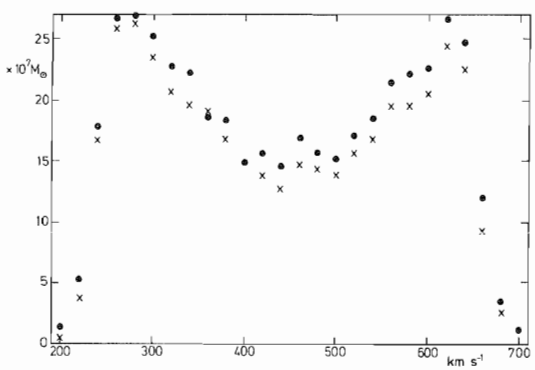

Figure 3.

Integrated line profiles as derived from the measurements with the 100 m telescope (×) and as derived from all observations combined (•). Both line profiles have the same velocity resolution.

Another check on the correctness of the procedure can be found in Fig. 3 where the integrated line profiles as determined from all observations together, and as determined from the 100 m observations alone are compared. The profile for all observations combined was derived from the full resolution maps after correction for the WSRT primary beam and after multiplication by the masks mentioned in section 4. The small differences may well be due to inaccuracies in the determination of the gain of the 100 m telescope system or of that of the WSRT synthesized beam. They may also be due to errors in the determination of the zero levels of the 100 m telescope single velocity maps. Since the profile determined from all

measurements combined lies above the other, the differences cannot be due to a failure to include all HI emission in the areas selected by the masks. The line profile derived from all observations combined probably is the more accurate one.

4. Combination and further reduction of the maps

The maps derived from the different sets of observations were combined to a single set of single velocity maps covering the range in velocity from +160 km s^{-1} to +780 km s^{-1} with an increment of 20 km s^{-1}. The maps were combined in such a way as to eliminate all grating responses out to 40' completely. This was considered to be more important than obtaining the lowest possible noise level in view of the large apparent size of NGC 4258 and of the possibility of finding hydrogen companions. Minimum noise was nevertheless approached to within 10%. Masks were derived using the single velocity maps after convolution to a 70" × 70" FWHP beam. By using these masks it became possible to derive integrated quantities with a much smaller noise contribution (e.g. the total HI map and the integrated line profile). As the masks were derived from maps obtained from an earlier version of the reduction, they are not optimal, but they are sufficiently good.

Fig. 4 shows the full resolution single velocity maps after all corrections had been applied. Only the parts of the maps where HI emission is visible are shown, but the masks have not been applied.

Another very useful way to display the data is in the form of "l-v" maps. In these maps the brightness temperature of the HI emission is displayed as a function of position along a line on the sky and of velocity. All kinds of velocity structures are more readily recognized on such maps. Fig. 5 shows a number of l-v maps, the positions of the separate maps relative to the different features in NGC 4258 is indicated in Fig. 6; the maps all lie at a position angle of $+60^0$, i.e. parallel to the minor axis. (The position angle of -30^0 for the major axis will be derived in chapter 3; the position of the dynamical center of the galaxy is assumed to be that of the optical nucleus as derived by A.A. Schoenmaker (quoted by KOM). Note the very large deviations from circular rotation and the very steep velocity gradients that occur near the nucleus; also note that these anomalous velocities are not strongly correlated with the anomalous arms.

References.

Albada, G.D. van; Shane, W.W.: 1975, *Astron. Astrophys. 42*, 433

Allen, R.J.; Hamaker, J.P.; Wellington, K.: 1974, *Astron. Astrophys. 31*, 71

Baars, J.W.M.; Hooghoudt, B.G.: 1974, *Astron. Astrophys. 31*, 323

Casse, J.L.; Muller, C.A.: 1974, *Astron. Astrophys. 31*, 333

Courtès, G.; Cruvellier, P.: 1961, *Compt. Rend. Acad. Sci. Paris 253*, 218

Harten, R.H.: 1974, *Synthesis Radio Telescope Project, ITR no. 121* (revised 1975)

Harten, R.H.; Westerhout, C.; Kerr, F.J.: 1975, *Astron. J. 80*, 307

Högbom, J.A. : 1974, *Astron. Astrophys. Suppl. 15*, 417

Kruit, P.C. van der: 1974, *Astrophys. J. 192*, 1

Kruit, P.C. van der; Oort, J.H.; Mathewson, D.S.: 1972, *Astron. Astrophys. 21*, 169

Someren-Gréve, H.W. van: 1976, *Netherlands Found. for Radio Astron. Note no. 220*

Willis, A.G.; Oosterbaan, C.E.; Ruiter, H.R. de: 1976, *Astron. Astrophys. Suppl. 25*, 453

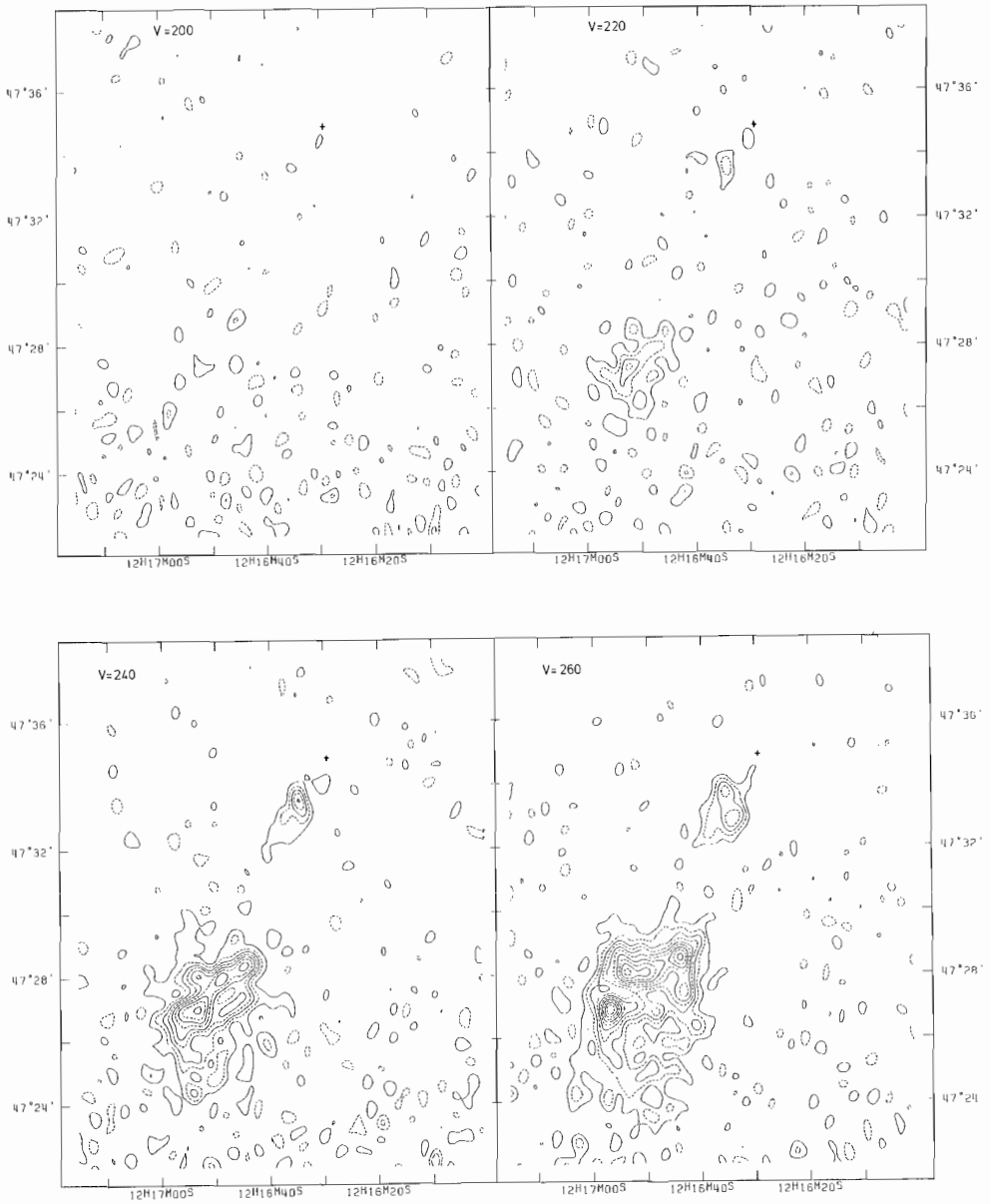

Figure 4.

The full resolution single velocity maps. The maps shown have been corrected for the attenuation of the WSRT primary beam. The plotted contours are ± 1,2,3, ... × 3 K. They are alternately dashed and full-drawn; the first positive contour is full-drawn. The assumed center of the galaxy has been marked with a "+".

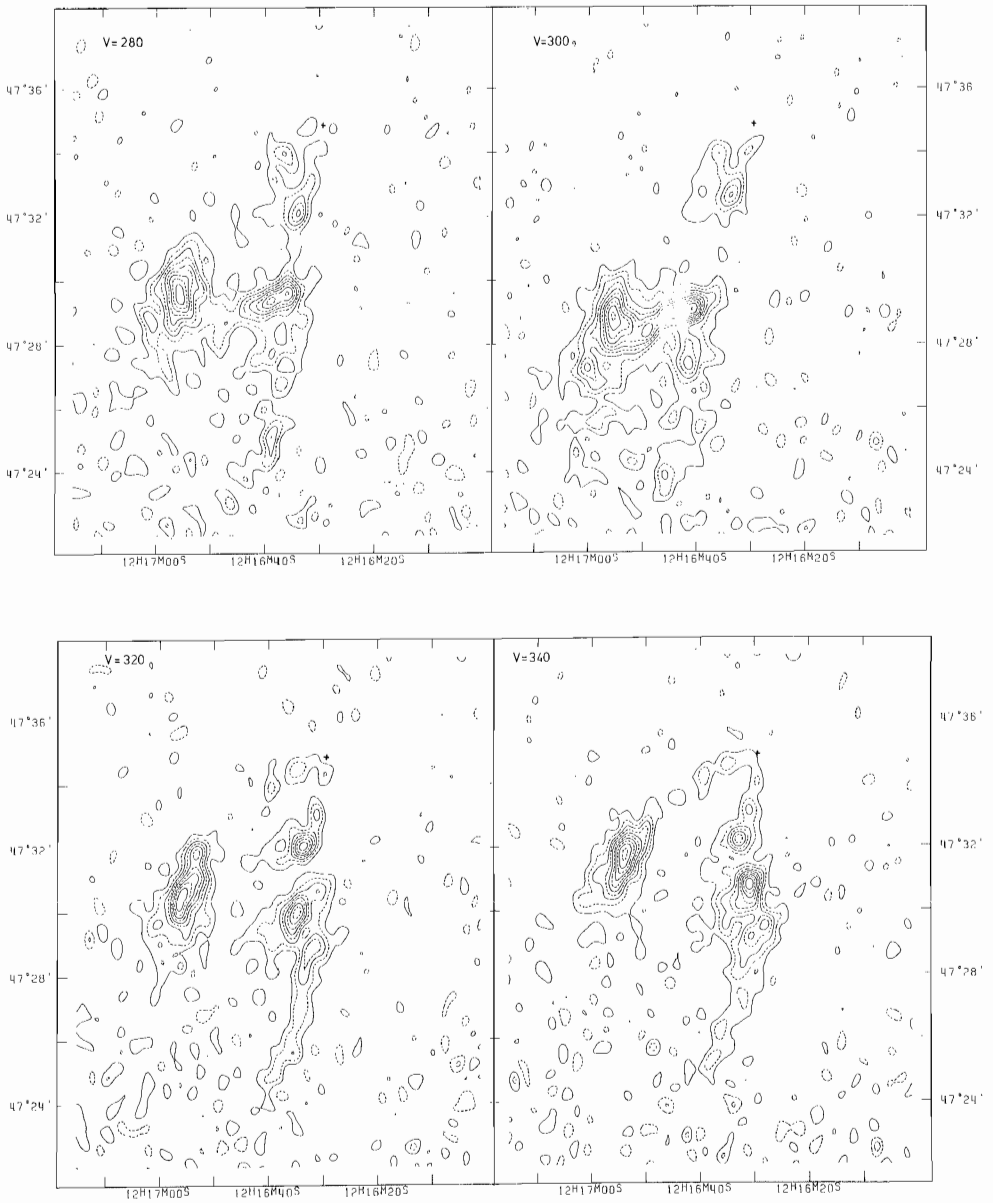

Figure 4 continued.

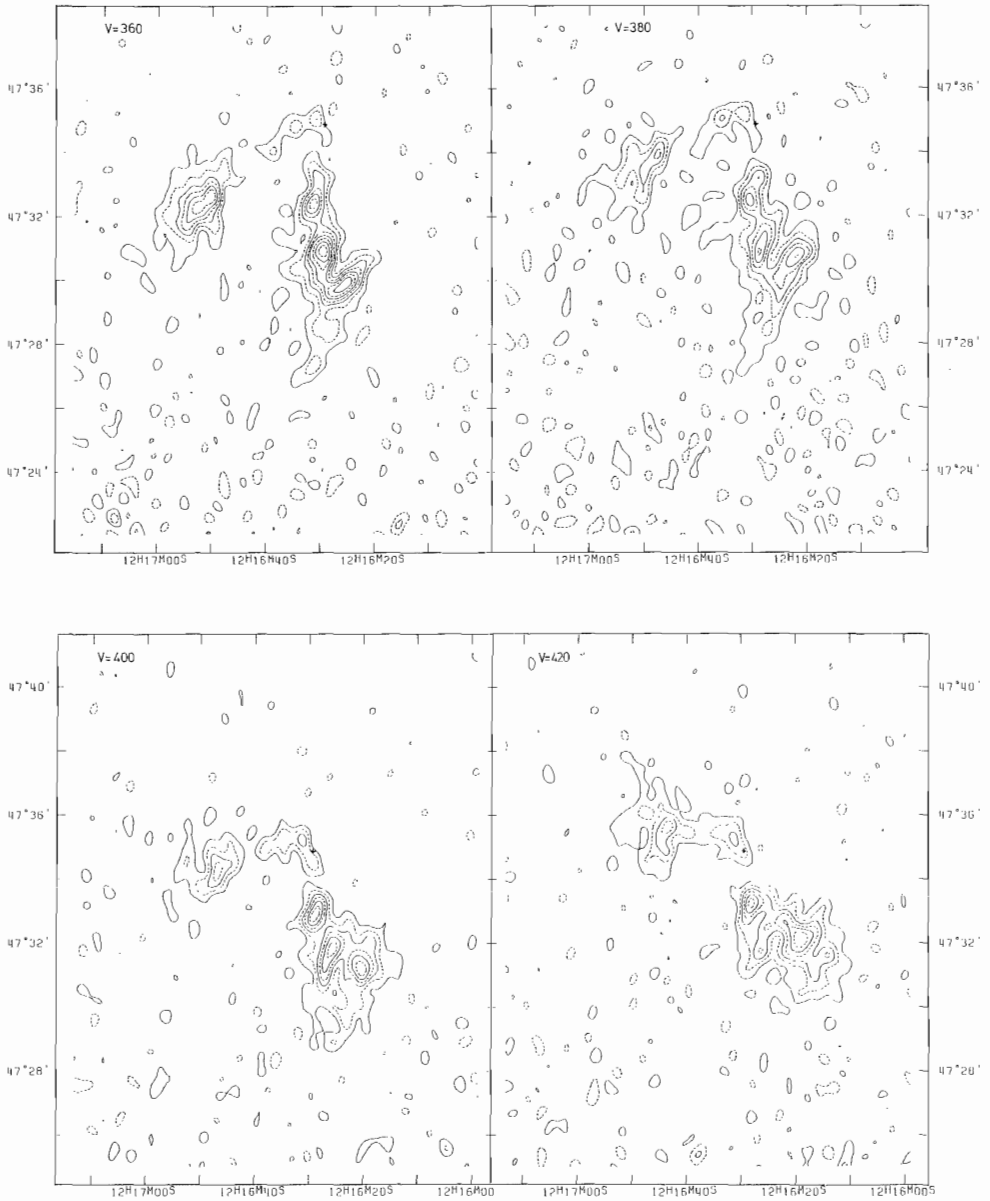

Figure 4 continued.

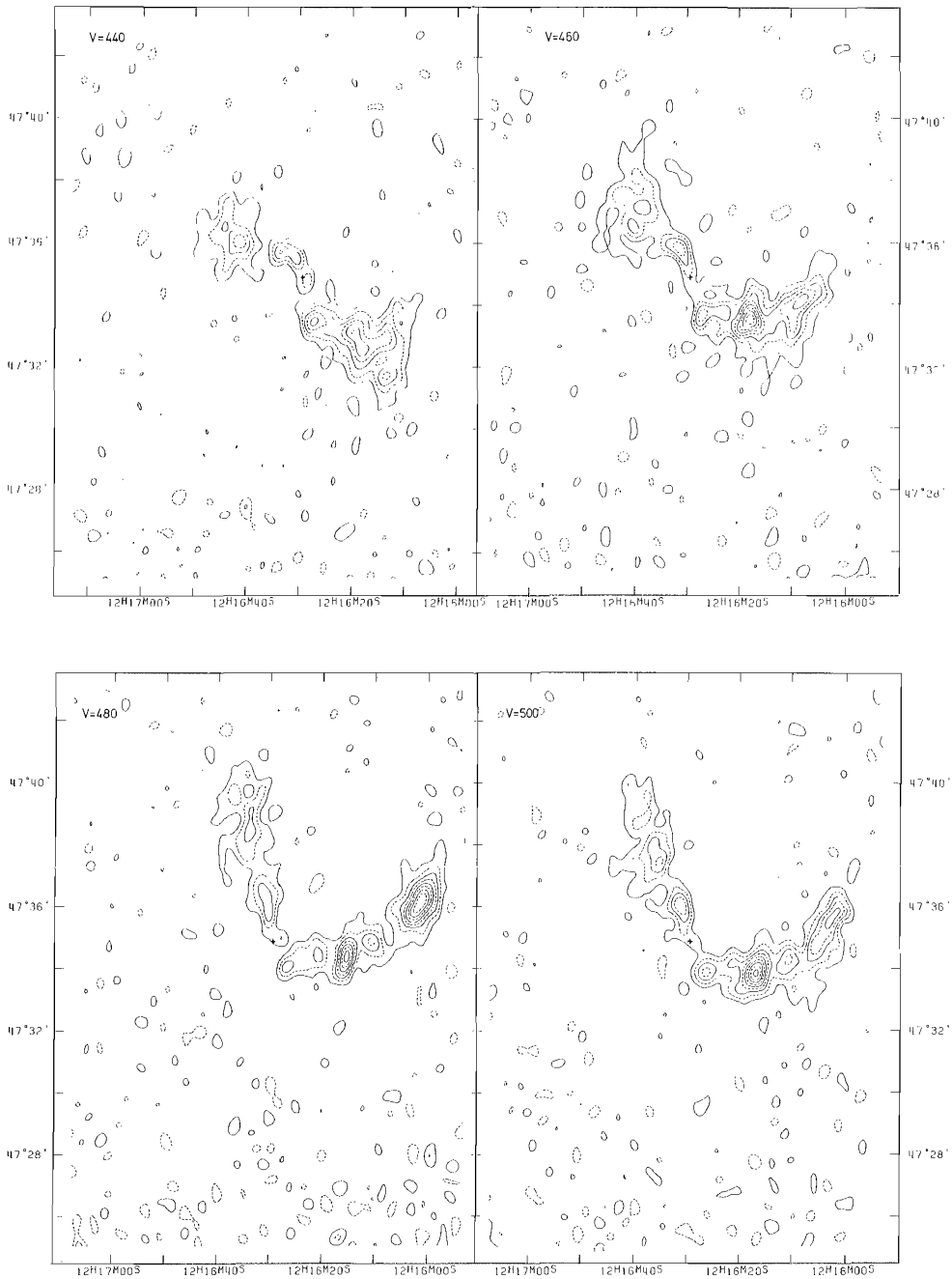

Figure 4 continued.

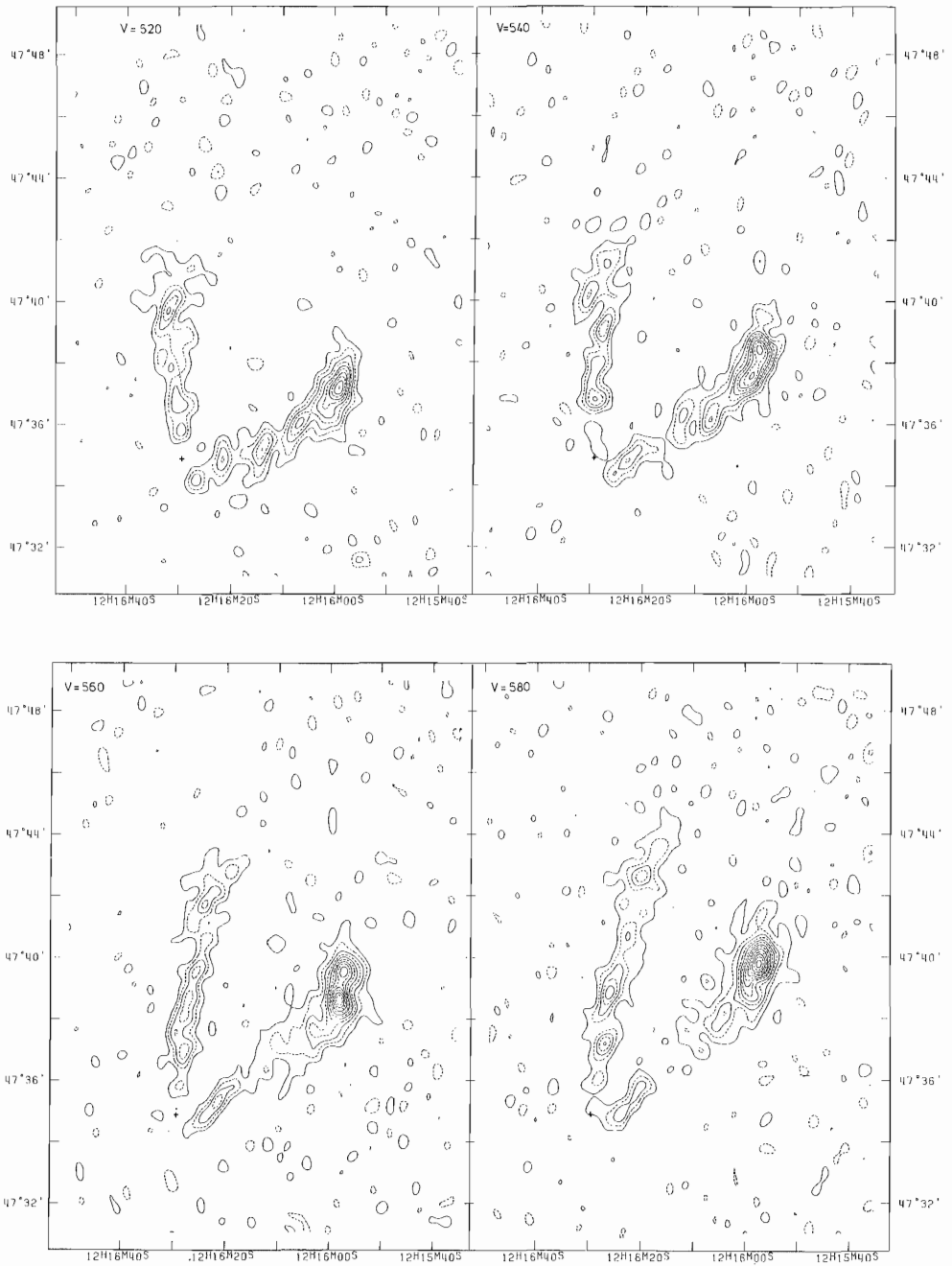

Figure 4 continued.

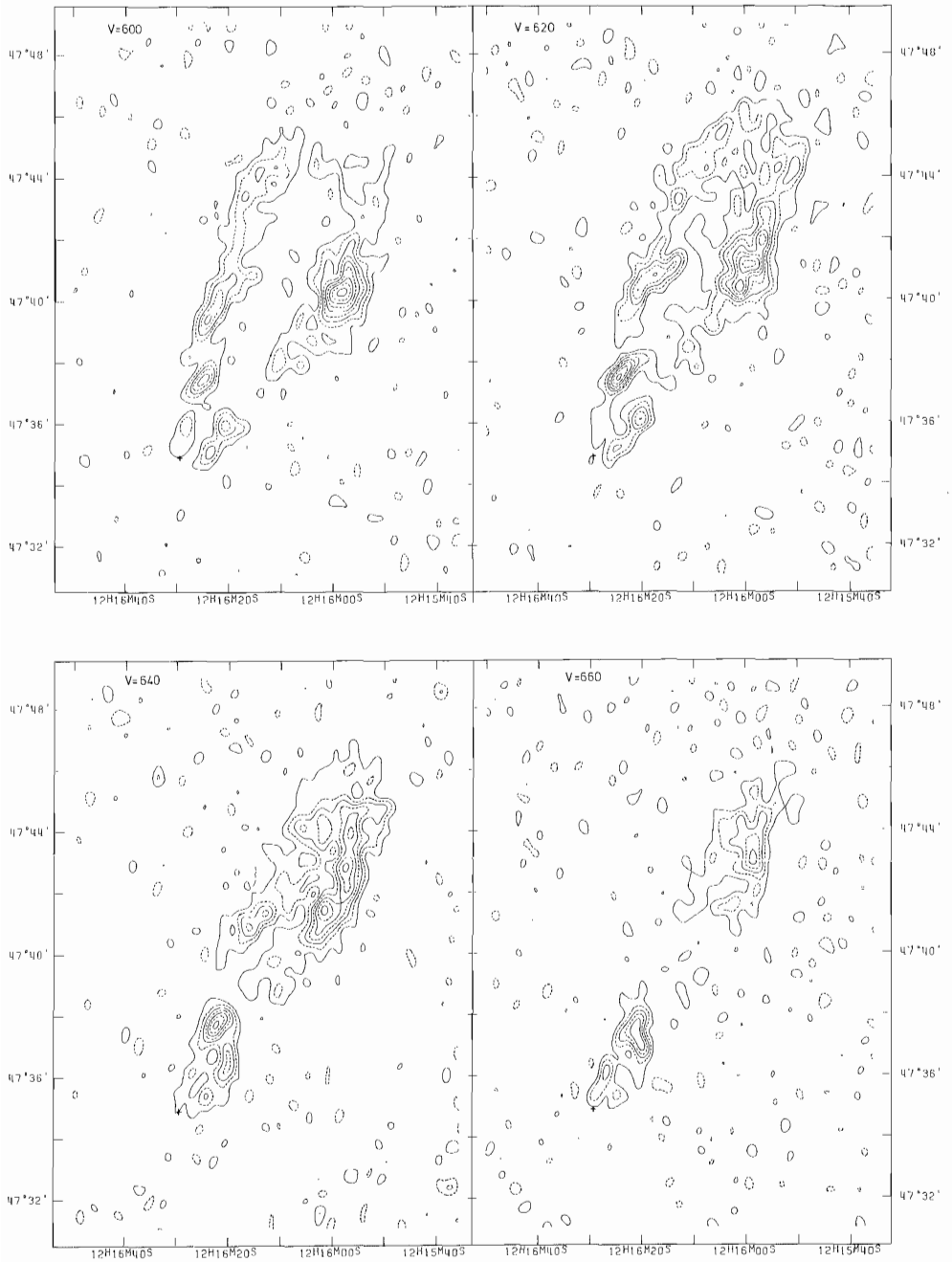

Figure 4 continued.

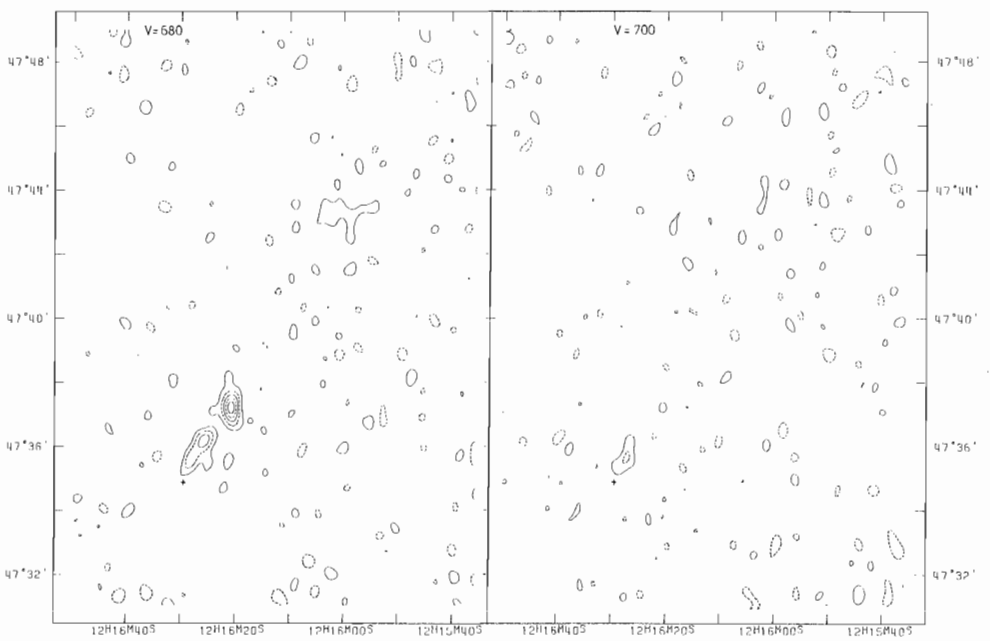

Figure 4 continued.

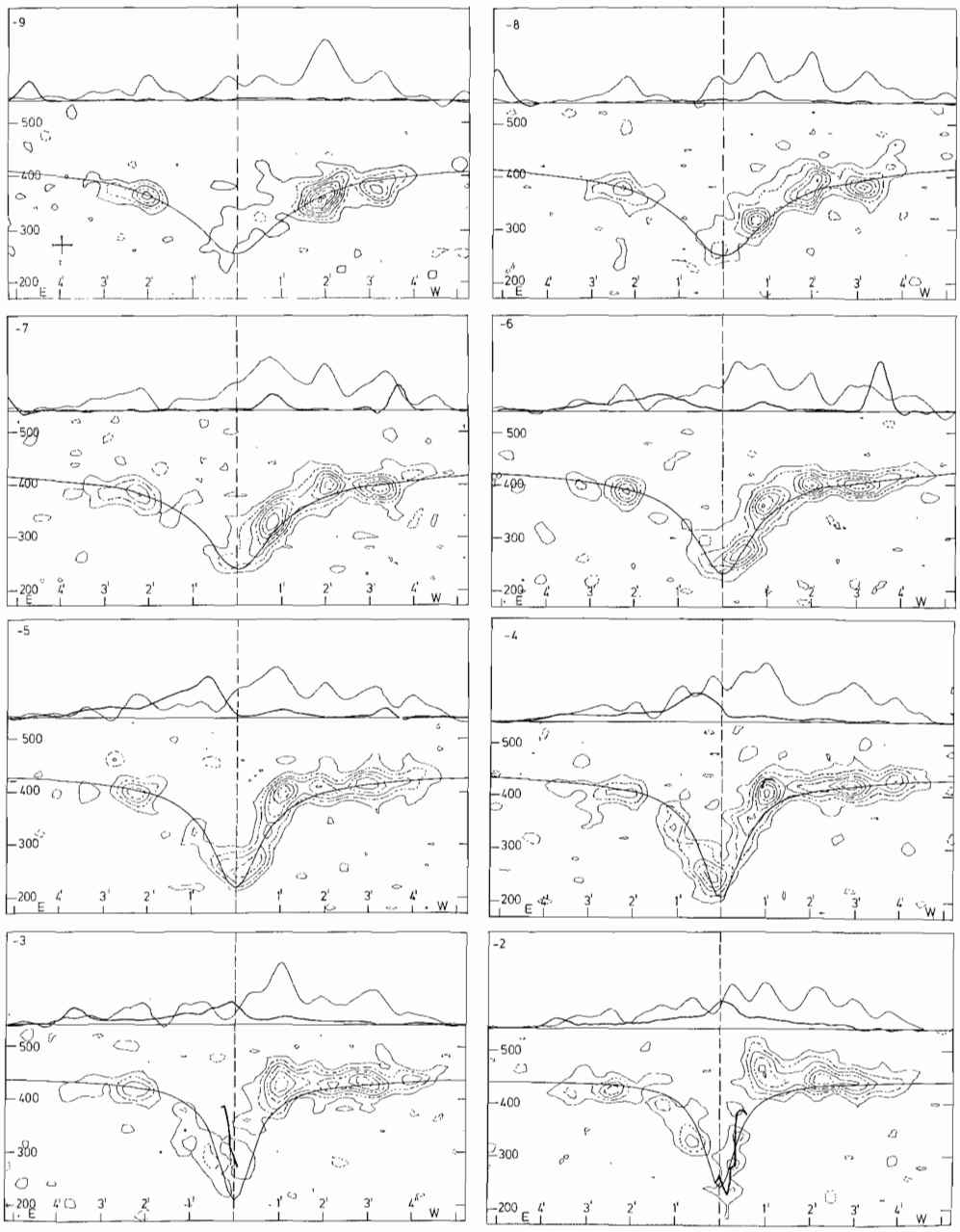

Figure 5.

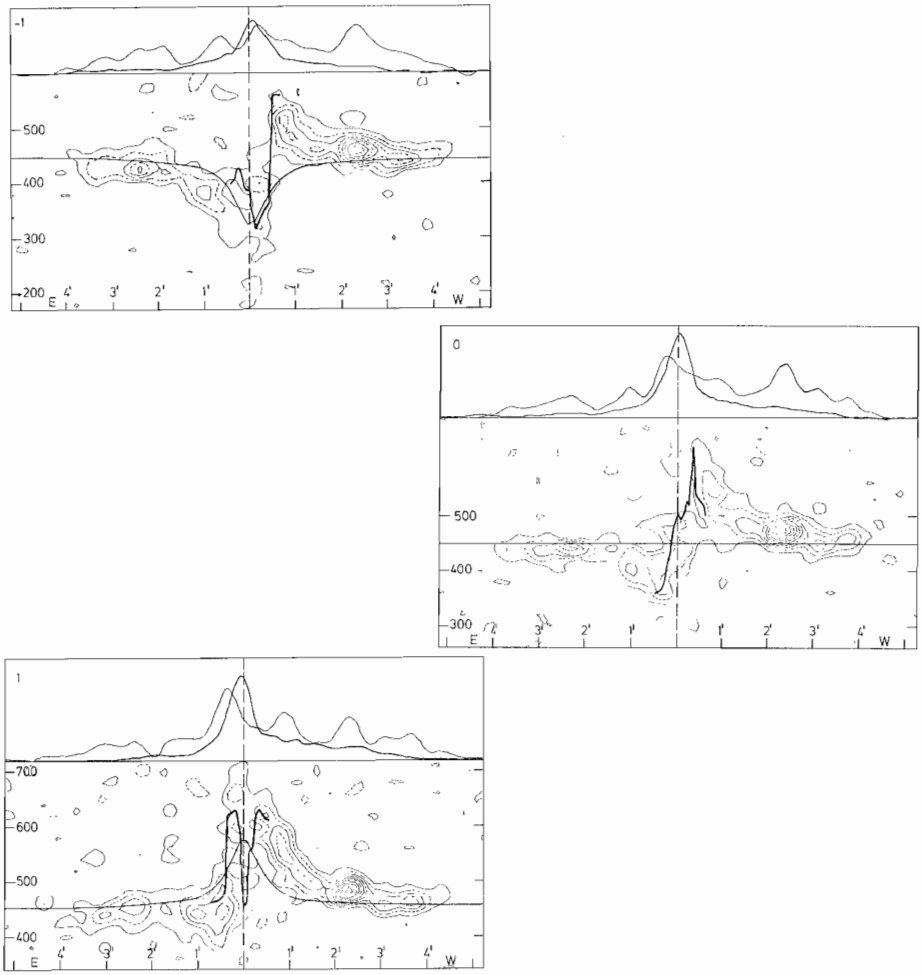

Figure 5.

A set of l-v maps.
The run of some other quantities on the same lines on the sky has also been drawn in:

1) Thin line in the l-v map proper: expected velocity according to a model rotation curve (Curve 2b from Fig.9 of chapter 3).
2) Thick line in the l-v map proper: Hα velocities derived from the measurements of Van der Kruit (1974) by interpolation. (Due to a sign error in the positions published for spectrum Q 4132 the velocities in the N-W anomalous arms are slightly wrong).
3) Thick line above the l-v map: 1412 MHz continuum emission.
4) Thin line above the l-v map: integrated HI (chapter 3).

The cross in the first l-v map indicates the FWHP "beam" for these maps.
The half power widths for the integrated HI and the continuum as plotted above the maps are equal to that of the spatial part of the beam.

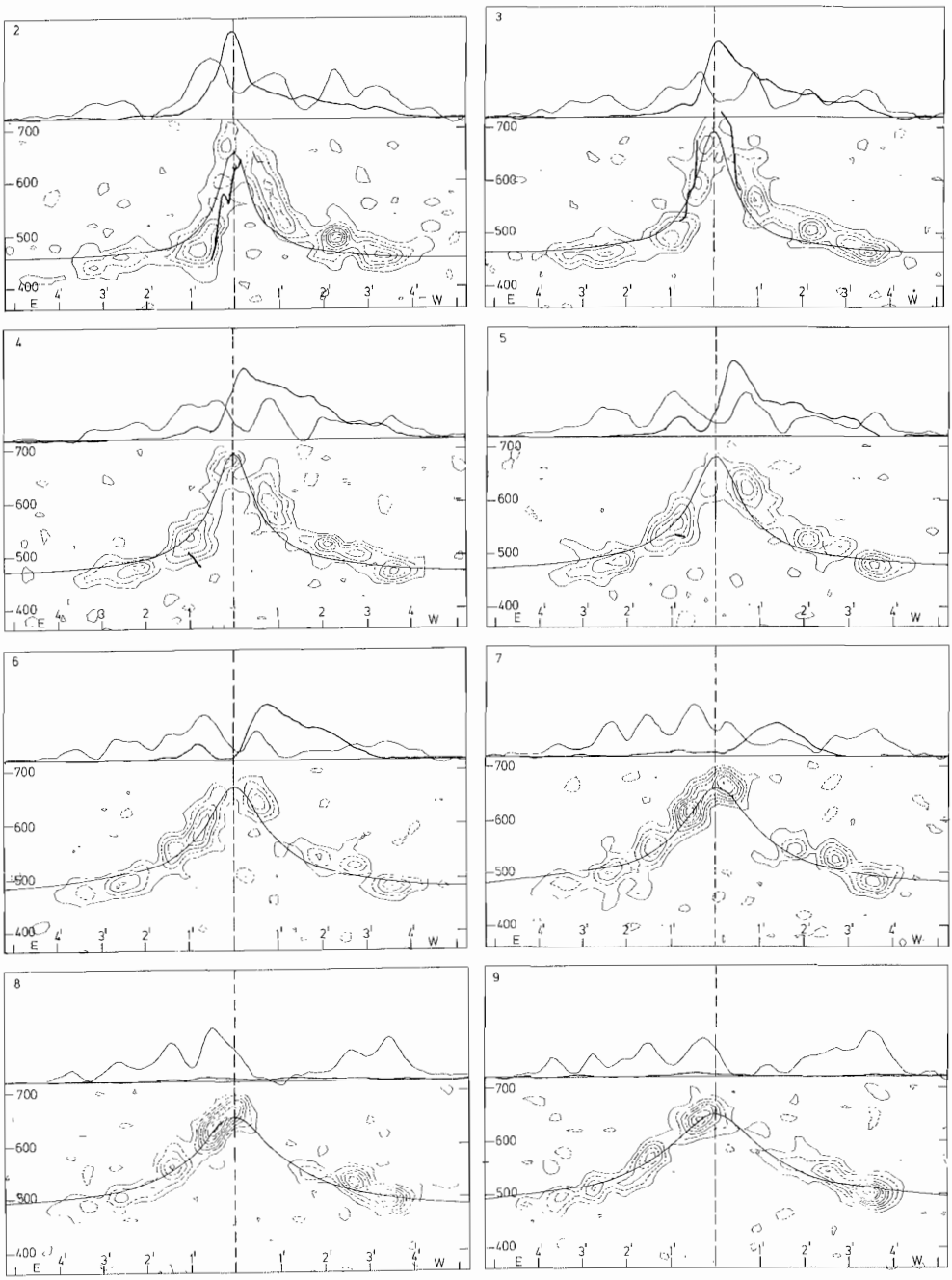

Figure 5 continued.

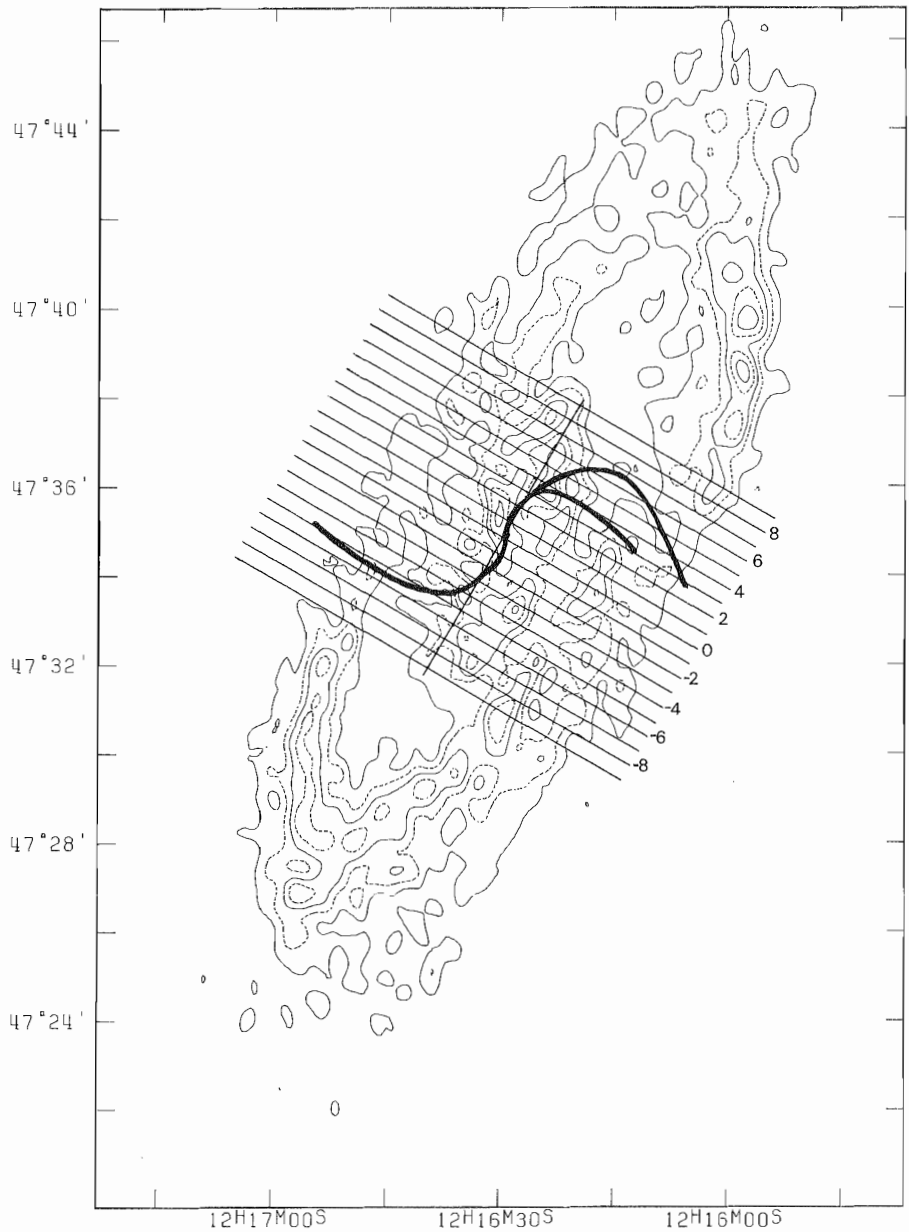

Figure 6.

Positions of the l-v maps of Fig. 5 relative to the integrated HI (contour map) and the continuum ridges (thick lines). The numbers indicate the positions relative to the minor axis. The relative distances of the cuts are 22.5, i.e. slightly less than one beam half power fullwidth.

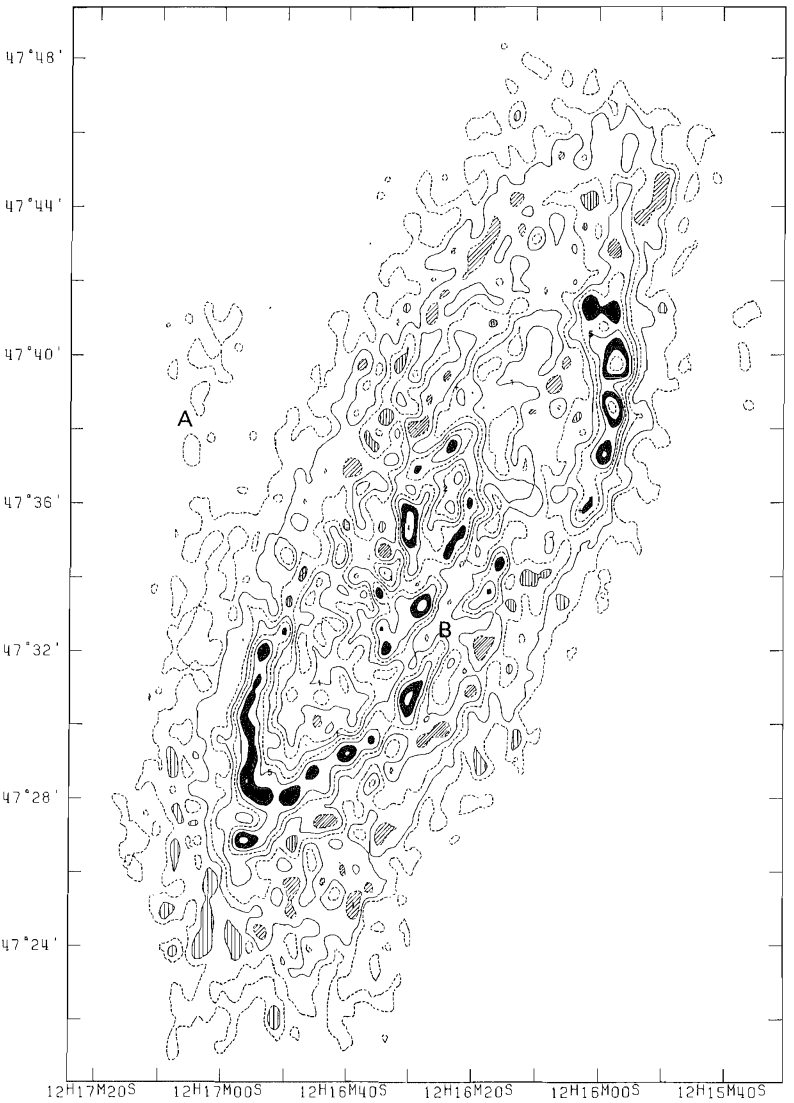

Figure 1.

Contour map of the integrated HI in NGC 4258. The contours have been drawn at intervals of 4 10^{24} H-atom m^{-2} (assuming small optical depths) starting at 4 10^{24} H-atom m^{-2}; a low contour of 10^{24} H-atom m^{-2} has been added. (10^{24} H-atom m^{-2} = 3.1 10^{23} H-atom m^{-2} face-on = 0.245 $M_\odot$ pc^{-2} face-on.) Local maxima have been shaded; the type of shading is an indication of the height of the peak. Alternating contours have been dashed.

All maps in this and in the next chapter except the l-v maps have been made to the same scale; the positions of the nucleus and each of the three reference stars used in making the overlay in Fig. 2 have been marked with a "+".

CHAPTER 3 NGC 4258 AS A SPIRAL GALAXY

Summary
In this chapter the properties of NGC 4258 as a spiral galaxy will be discussed. It will be demonstrated that NGC 4258 contains a bar-like structure that has a large influence on the observed velocities.

1. The integrated HI and the continuum emission of the disk

The integrated HI map is shown in Figs. 1 and 2. It was derived from the full resolution single-velocity maps after these had been multiplied by the masks described in chapter 2, section 4.

A number of features are immediately evident from the map:

-- The HI emission is much stronger, compared to the optical brightness, in the outer parts of the galaxy than in the inner parts (Refer also to Fig.14). This effect is generally seen in spiral galaxies. The center of NGC 4258 is not, however, devoid of HI, as is e.g. the center of M 81 (Rots and Shane, 1975); if the HI density is averaged in annuli in the plane of the galaxy one even finds the maximum density in the center (Fig.3). The total amount of HI observed in NGC 4258 is $4.4\ 10^9\ M_\odot$. Optical depth effects will cause this to be an underestimate of the amount of HI actually present.

-- Also different from the situation in M 81 is the sharp decrease of the observed HI surface density outside the optical boundary; above the level of $10\ K\ km\ s^{-1}$ only two features are visible:

i. At the S-E side of the galaxy a faint spiral arm can be seen, the feature marked "A" in Fig.1. It seems to rotate normally with the galaxy.

ii. There may be a faint, short bridge between NGC 4258 and its companion NGC 4248. However, the relevant single-velocity maps have some dynamic range problems at that level.

-- The same irregular spiral structure is visible in HI as in the optical photographs. The minima around 10 kpc on the major axis are even more pronounced in HI than in the optical photograph shown in Fig.15. It is not possible to give a quantitative estimate of the density contrast between the arms and the interarm regions. This is due to the fact that the spiral arm maxima are barely resolved and to the non-uniformity of the HI surface density in those regions that may be called interarm regions. A quantity much better defined is the peak over the mean density ratio, which is also shown in Fig.3. One must keep in mind, however, that the peak densities tend to be underestimated due to resolution and optical depth effects.

-- The HI in the two optically bright spiral arms lies at the inside edge of these arms, i.e. at the side nearest to the nucleus. The HI coincides well with the dust-lanes. Following Capaccioli (1973) I will henceforth refer to the optically bright region bounded by these arms as the "lens". Except for these two bright arms no clear spiral structure is discernable in this region.

-- Of the arms that lie further out, a dust-lane is visible only in the arm marked "B" in Fig.1. This dust-lane has a fairly irregular structure but generally it seems to lie at the outside of the arm. Also in this case the HI and the dust coincide very well. In this arm, as in the other outer arms, the HII regions generally cluster around peaks in the HI. The spiral arms will be discussed more extensively in section 5.1.

-- In the central region a bar-like feature is visible. In section 5.2 it will be argued that NGC 4258 is, in fact, a barred spiral.

-- As can be seen from Fig.6 of chapter 2 the region of the anomalous arms seems

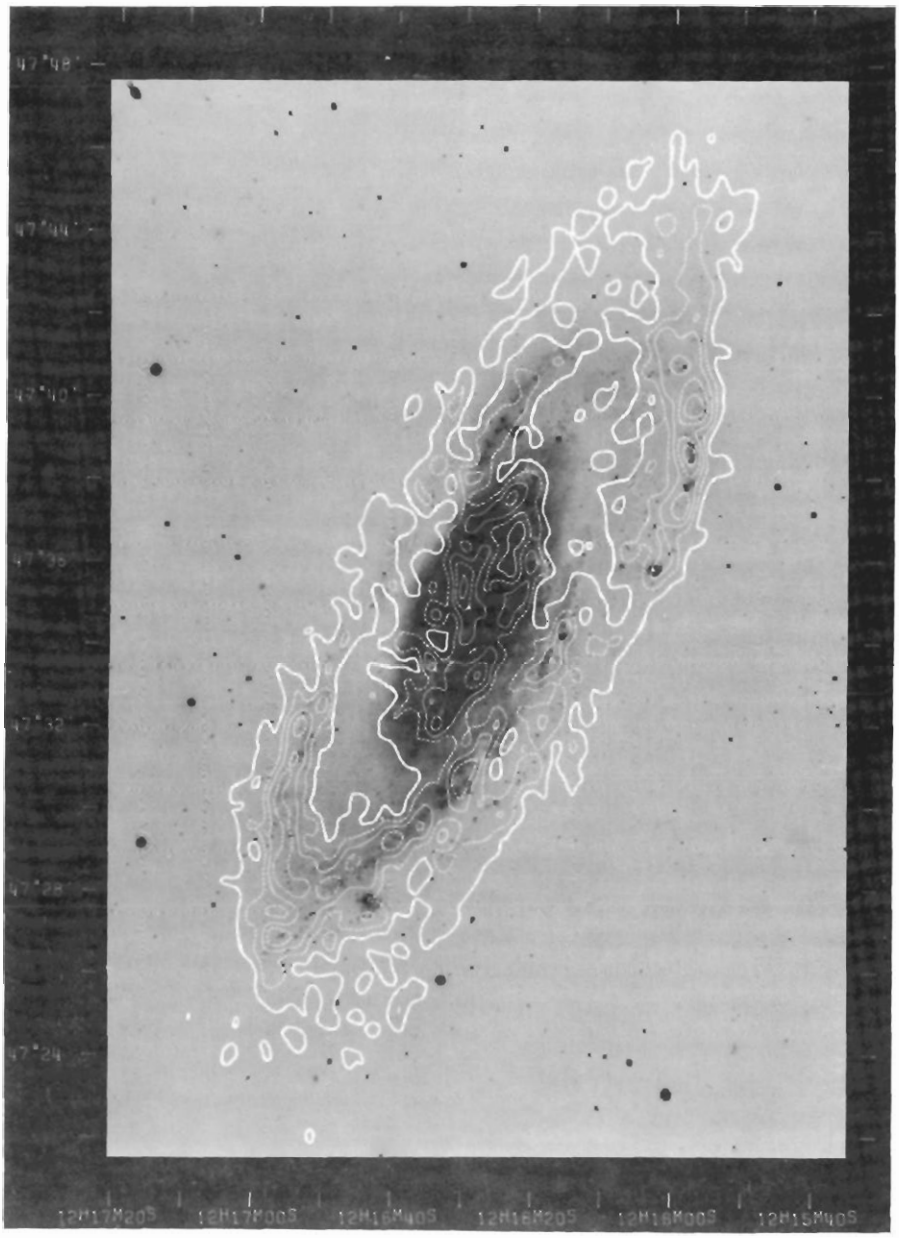

Figure 2.

Contour map of the integrated HI superposed on a photograph (courtesy A.R. Sanders and W.C. Miller). The contours have been drawn at intervals of 6 10^{24} H-atom m^{-2}, starting with 6 10^{24} H-atom m^{-2} (heavy contour). In order to retain the structure in the lens, without losing the outer arms, the two components were given different exposures in producing the print.

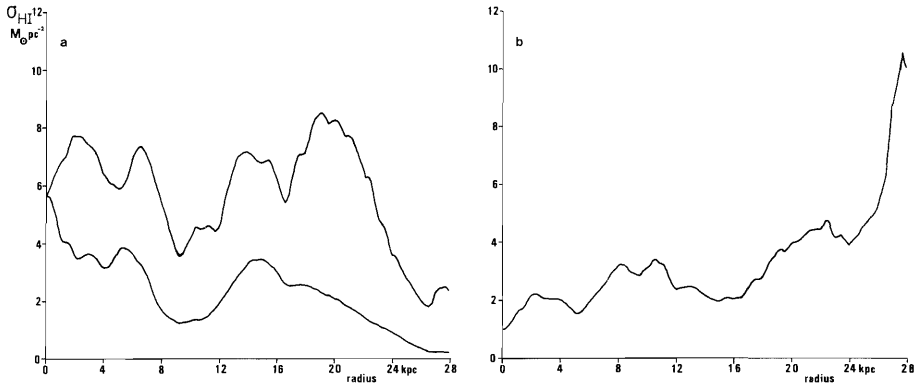

Figure 3.

a) The face-on surface density of HI averaged in circular annuli in the plane of NGC 4258 and the peak intensities in the same annuli. Both curves have been smoothed slightly. b) The ratio of the peak to the mean density of HI.

Table 1

Other 1.4 GHz observations of NGC 4258

Freq. MHz	Bandw. MHz	Flux Jy	HI -,?,!	Author	Notes
1420	?	0.93	!	Lequeux, 1971	
1415	4	1.1	!	De la Beaujardière et al., 1968	
1400	8	0.9	-	Heeschen and Wade, 1964	
1410	8	0.97	!	De Jong, 1965	
?	?	0.88	?	Rogstadt et al., 1967	1
1400	60	0.84	!	Maslowski, 1972	2
1415	4	0.82	!	De Bruyn, 1977	

Notes:

1. Interferometric observation with a base-line of 30 m. Both HI and continuum were measured. Neither the bandwidth nor the central frequency for the continuum band were given, but quite probably no HI was included in the band. The flux may have been slightly underestimated due to the use of an interferometer.
2. Observation with the 300 foot telescope at Greenbank. No beam broadening was observed, which may indicate that the flux may be slightly too low. Due to the very large observing bandwidth the contribution of the HI amounts to no more than approximately 5%.

to lack in HI. This is most clearly seen where the anomalous arms cross the normal arms. Although similar gaps in the HI density are observed at other places along the normal arms, the systematic association between such gaps and the anomalous arms indicates a physical connection. In principle it is possible that the observed lack of HI, which amounts to something of the order of 40% when compared to the HI surface density just outside the anomalous arms, is due to absorption. This means that part of the continuum emission at the frequency of the line is absorbed in the HI, causing an over-correction for the continuum if the normal reduction procedure described in chapter 2 is employed.

If we assume that all HI lies in a uniform layer between us and the continuum arms we can estimate the excitation temperature of the HI. The highest emission temperature observed in the 1412 MHz continuum map (chapter 2, Fig.1) is slightly over 20 K. A significant reduction of the HI surface density is, however, also observed in regions where this temperature does not exceed 10 K. In order to explain a 40% reduction in the HI surface density an excitation temperature of no more than 25 K would have to be assumed for the HI. Any other assumption for the distribution of the HI and the continuum emitting regions would lead to an even lower value for this temperature. This indicates that the observed lack of HI emission is due to a real lack of HI. The anomalous arms will be discussed more extensively in chapter 4.

Disregarding the anomalous arms it is evident from the continuum map (chapter 2, Fig.1) that only the spiral arms at the edge of the lens show an appreciable amount of continuum emission, coinciding with the bright HII regions at the outside edges of those arms. Some emission can be seen in arm "B", especially in the 49.5 cm continuum map published by De Bruyn (1977). This emission cannot be thermal in origin, otherwise it should have been much stronger at 1412 MHz. No other emission exceeding the dynamic range limit of 0.1 K is visible outside the lens at 1412 MHz, not even from the complex of HII regions in the N-W arm. This cannot be due to a failure to estimate the contribution of the 0 m or the 18 m base-line correctly; the contrast with the interarm region should be visible even if the local zero-level is wrong.

Quite probably the 18 m base-line contribution has in fact not been estimated entirely correctly since I find an integrated flux for NGC 4258 of only 0.68 Jy instead of 0.9 Jy as generally reported in the literature. The continuum flux in NGC 4258 was determined by integrating the flux in annuli around the nucleus of NGC 4258 out to the first annulus having a negative integrated flux. Annuli of different shapes were tried, viz circles and annuli that would be circular in the plane of NGC 4258. The total flux found was virtually independent of the shape of the annuli. Adding a small offset in the zero-level determined from the first negative annuli made only an insignificant difference. The most probable cause of the trouble is that the base disk of NGC 4258 has an average emission temperature of approximately 0.15 K and that this contribution has been missed in determining the 18 m base-line response. This would cause a very shallow bowl in the map where in fact a small, but positive mean flux should have been measured.

It must, however, also be remarked that most of the continuum observations near 1400 MHz have been contaminated with HI emission, which occurs between 1416.9 MHz and 1419.5 MHz. Only observations more than a full bandwidth away from this frequency range should not be contaminated (Table 1). Considering all evidence I think that the correct flux for NGC 4258 is 0.82 Jy with a probable error of 0.04 Jy.

2. The velocity field of NGC 4258

2.1 Determination of the velocities

The velocities were determined from the masked maps using the profile fitting technique described in chapter 5. The resultant velocity field is shown in Fig.4. The first thing that catches the eye is the fact that, except for the innermost region, the velocity field is quite regular. In the central part, however, the iso-velocity contours make a considerable angle with the minor axis and indicate

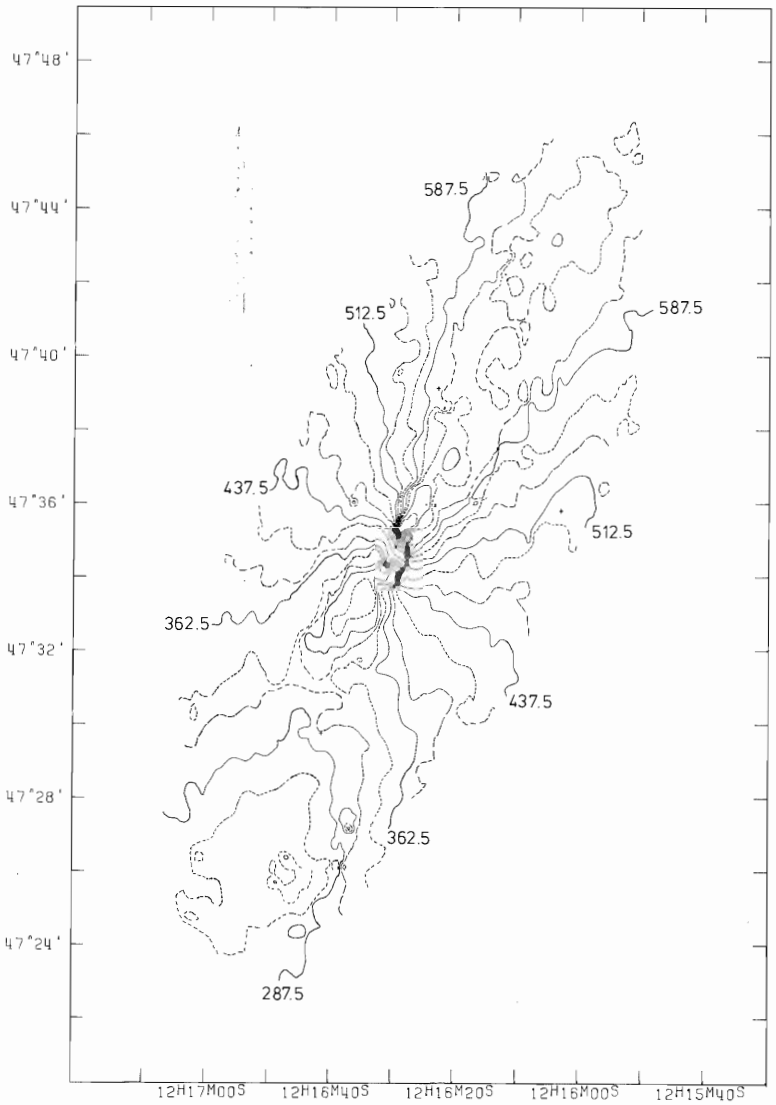

Figure 4.

The full resolution velocity field. The contour values are indicated in the figure. For the sake of clarity some of the measured points with low weight had to be deleted; the velocities at those positions have been interpolated by hand. These points lay at the outer edge of the disk and in the gaps in the HI density near the major axis.

a very steep velocity gradient. The exact nature of this velocity gradient is best studied by looking at the l-v maps (the most relevant l-v maps are shown in Fig.5 of this chapter; a more complete collection can be found in Fig.5 of chapter 2). It will be seen in sections 5 and 6 of this chapter that the observed flow-pattern can be explained by assuming that NGC 4258 is a barred spiral. A much smaller perturbation of the velocity field can also be recognized in the Southern part of the galaxy. The nature of this perturbation suggests that this part of the galaxy is warped. The warp cannot be described by a tilted-ring model, such as that of Rogstad et al. (1974) for M 83, since it is not symmetric with respect to the nucleus. Both optical photographs and the velocity field suggest that the galaxy is bent sharply along a line, more or less like a dog's-ear in a piece of paper. The warp occurs in the part of the galaxy that lies furthest away from the small companion galaxy NGC 4248, nor is there any other nearby galaxy on that side except for a very small, highly centrally condensed elliptical. No redshift is available for this elliptical. Feature "A", which may be regarded either as a normal outer arm (i.e. a long-lived feature) or as a "tail" of the type studied by Toomre and Toomre (1972), connects to the warped side of the galaxy. The velocity field will be considered in more detail in section 5.

Maps of a number of other quantities were derived simultaneously with the velocity field. The most interesting among these is the map of the peak intensities in the line profiles (Fig.6 ; the quantity shown is I_p as defined in eq. (1) of chapter 5). The spiral arms are much better visible here than in the integrated HI map, but one must be careful in interpreting the I_p map because variations in the velocity dispersion and steep velocity gradients may cause changes in the position of a feature, and may even cause it to disappear entirely, as is the case with the HI bar, which is not visible in this map.

2.2 Determination of the projection parameters and the systemic velocity

Starting from the older values for the projection parameters and the systemic velocity that were published by Van Albada and Shane (1975) some attempts were made to obtain a better fit to the observations. What I considered to be the best fit to the velocity field in Fig.3 was obtained with inclination $i = 72^{\circ}$, position angle of the line of nodes $\psi = -30^{\circ}$ (definition in chapter 5, section 3.1), and $V_{sys} = 450$ km s^{-1} (heliocentric). In obtaining these values the central region was disregarded, and for the determination of the projection parameters the S-E part of the galaxy - the region of the warp - was not used either. An eye estimate of the projection parameters applicable to the warped region, considering both the velocity field and optical photographs, leads to approximately the following values: $i = 75^{\circ}$ and $\psi = -15^{\circ}$. Since the very deviant behaviour of the iso-velocity contours in the inner region is quite probably due to large deviations from circular rotation no attempt was made to obtain a separate set of projection parameters for the region.

That quite a good fit was obtained for at least 2/3 of the galaxy can be seen from the residual velocity field in Fig.10. Using these projection parameters some deprojected maps were constructed (Figs. 7 and 8). It is evident from these figures that NGC 4258 does not have a regular spiral structure at all. The general HI distribution suggests a Θ-type barred spiral, but various other features are also present.

2.3 The rotation curve

A number of different rotation curves have been derived from the velocity field. Two of the best are presented in this chapter. Both were derived by using all measured velocities but different weighting functions.

The inclusion of all measured velocities implies that no points were rejected on basis of the fact that they lay in the anomalous arms. This is especially important in the central region where a large fraction of the measured velocities may be considered as coming from the anomalous arm regions. Since the most evidently anomalous velocities in the central region do not lie in the anomalous arms,

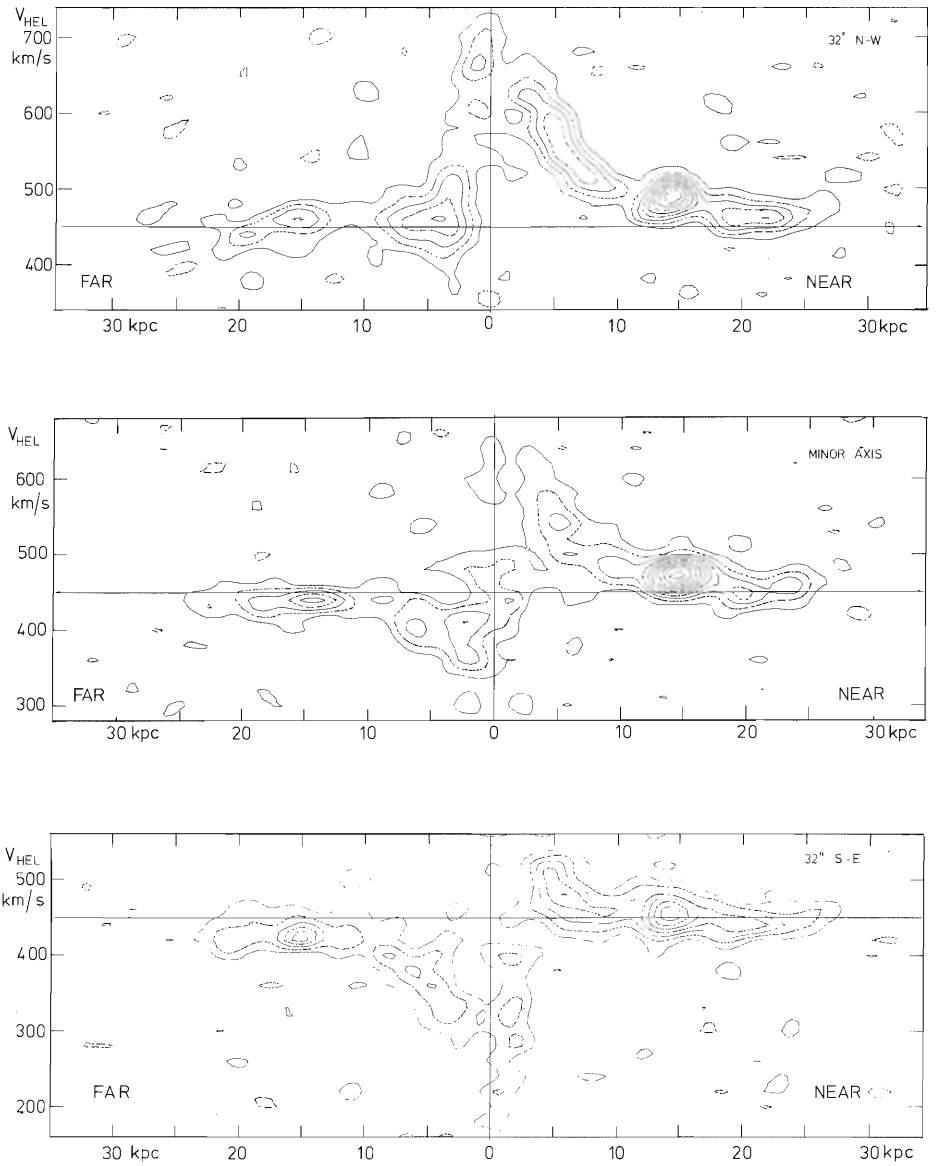

Figure 5.

Three l-v maps parallel to the minor axis. The positions relative to that axis have been indicated in each. The contours have been drawn each 2.5 K, with 0 K omitted; the maps have not been corrected for primary beam attenuation. Similar maps are shown in Fig.5 of chapter 2. The major axis and the systemic velocity have been indicated.

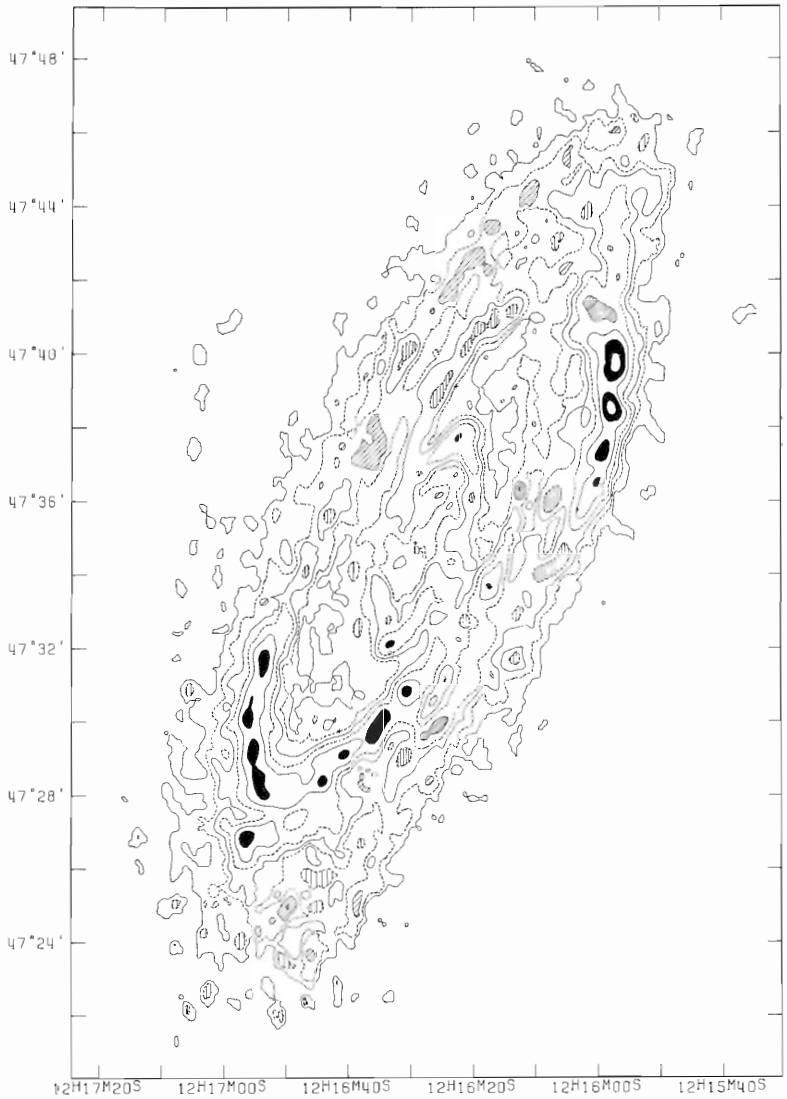

Figure 6.

Map of the peak intensities. Contours have been drawn at levels of (1, 2.5, 4, 6, 9, 12, 15) × 2.5 K. The peaks have been indicated in a similar manner as for the integrated HI map.

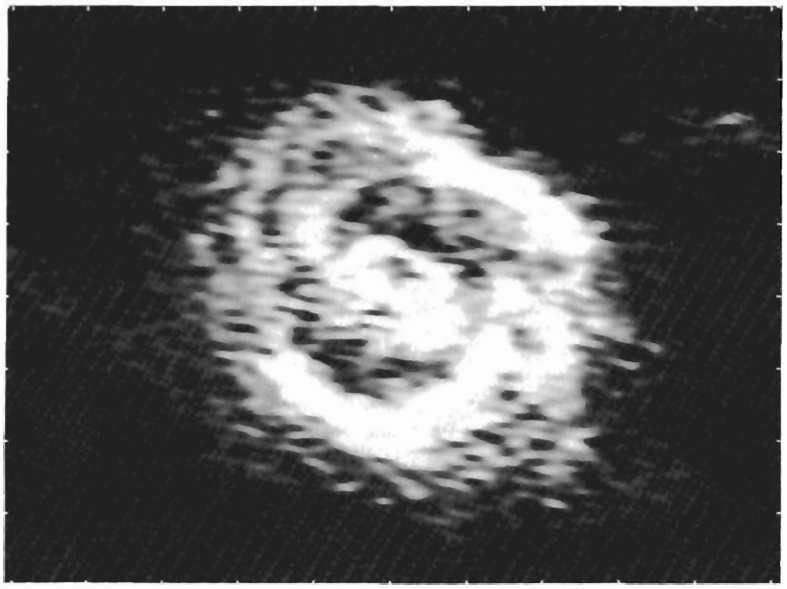

Figure 7.

Radio photo of the integrated HI map after deprojection. The same projection parameters have been used for the entire galaxy, so that the S-E side remains distorted. The line of nodes is vertical; the minor axis horizontal. Note that the Eastern side of the galaxy, where the weaker of the anomalous arms lies, also contains much less HI than the Western side.

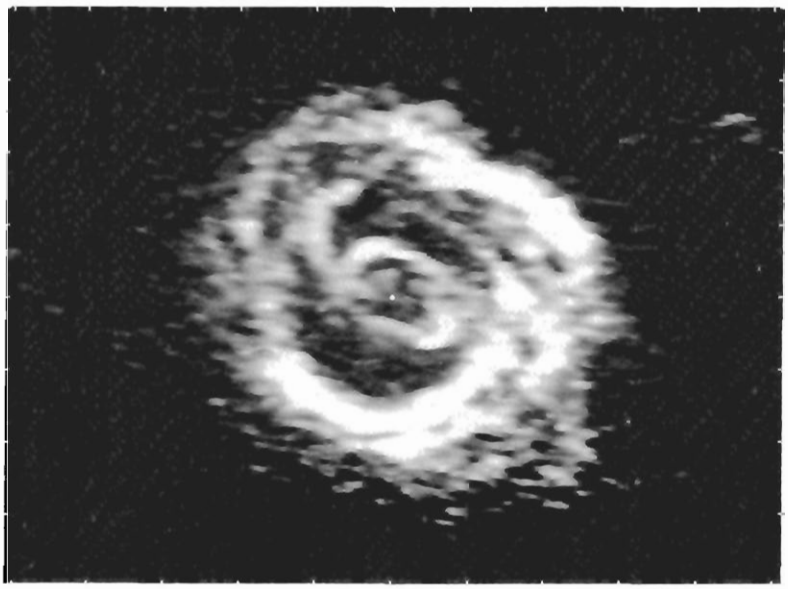

Figure 8.

Radio photo of the deprojected I_p map.

exclusion of the measurements in those arms would certainly have resulted in an erroneous rotation curve. The fact that the rotation curve presented by Van Albada and Shane is much lower in the central part than those presented here is caused by excluding these points and the resulting higher relative weight of points having anomalously low apparent rotational velocities.

The errors in the observed velocities were calculated as for intensity weighted mean velocities. This generally leads to a considerable overestimate of the actual errors. However, the dominant contribution to the error in each velocity, as a measure of the local circular velocity, is to be found in the deviations from circular rotation in the galaxy itself. Therefore terms representing such deviations were included in calculating the errors - and consequentially the weights - for each of the measured velocities (refer to chapter 5, section 2). The values of these terms were chosen independently of the radius, which evidently is an oversimplification.

Rotation curve no. 1 in Fig.9 was calculated using weights only dependent on the errors calculated as indicated. For the determination of curve no. 2 an extra factor $\sin^2(\theta)$ (θ is the central angle in the plane of the galaxy relative to the line of nodes) was included in the weights, so that zero weight was given to the points on the minor and on the major axes. Curve no. 2 is much smoother than curve no. 1. The extra factor was introduced in this case because it makes the rotation curve independent of the variations in rotational velocity associated with two-armed density-wave streaming. It does, however, increase the sensitivity to variations caused by the velocities in the r-direction associated with such streaming. Which of the two effects is the more important is dependent on the position in the disk. The former effect will be dominant near corotation, the latter near the Lindblad resonances (chapter 5). The exclusion of the points on the major axis also decreases the effective radial resolution in the determination of the rotation curve; the axes in the directions $\theta = 45^{\circ}$ are a factor $\sqrt{2}$ shorter than the major axis. This effect is, however, far too small to explain the observed smoothing. The exclusion of a number of points showing very deviant velocities near the gaps in the HI on the major axis may have played a role in causing curve no. 2 to be smoother.

From this discussion it will be clear that the increased smoothness of curve no. 2 quite probably is due to the diminished influence of certain errors, reason to include this curve.

It must be stressed that, due to the large non-circular motions in the

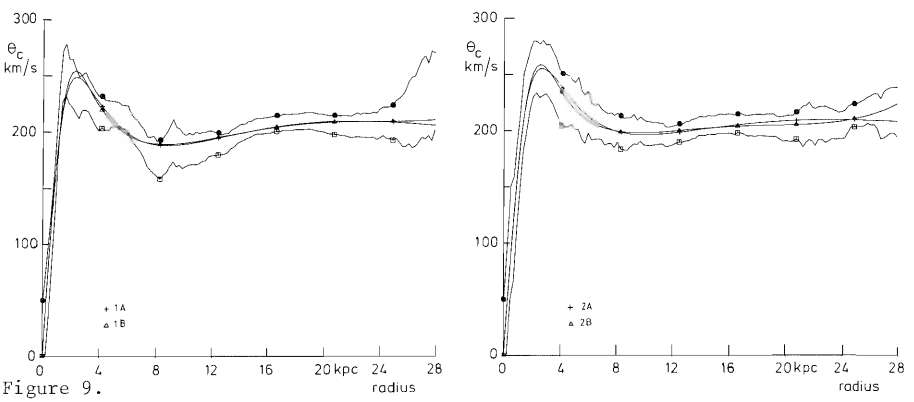

Figure 9.

Rotation curves for NGC 4258. The manner of their deviation is described in the text. The measured curves themselves are not known, but only the measured curves plus and minus the estimated errors. The model rotation curves that were fitted have been drawn in.

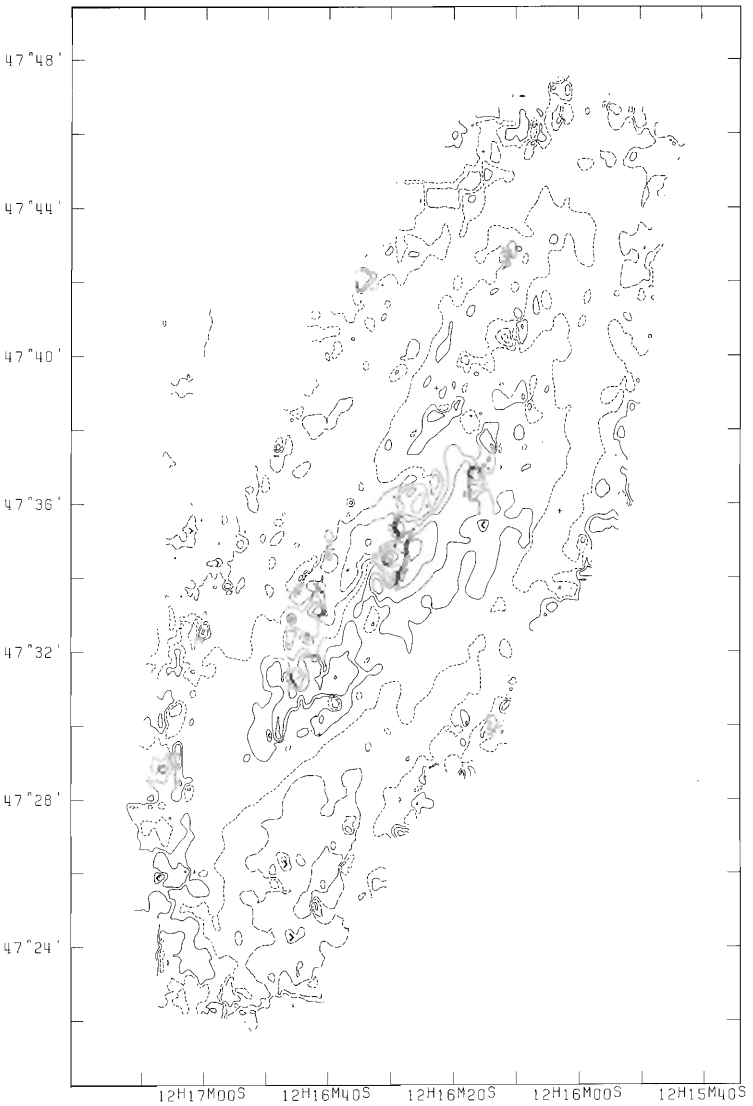

Figure 10.

Map of the residual velocities after subtraction of a model velocity field derived from rotation curve no.1a. Contours are 0 km s^{-1} (short dashes) and ± 20, ± 40, ± 70 and ± 100 km s^{-1}. Negative contours have been drawn with long dashes. If the absolute value of the residual in a small region is smaller than that in the surrounding region this has been indicated with a "<" or a ">". As in the velocity map in Fig.4, some authorial intervention has been necessary. The contours in arm "A" are all -20 km s^{-1}.

central part of NGC 4258, the circular velocities out to approximately 6 kpc are very inaccurately known. One should realize, however, that the concept of circular velocities is in fact only well defined for an axisymmetric potential. The large deviations from circular rotation in the central part of NGC 4258 indicate that the mass distribution and hence the potential may be far from axisymmetric.

The rotation curves were smoothed by fitting mass models, as discussed in the next section. The resulting model rotation curves are also shown in Fig.9. The curve labelled "1a" was used to construct a model velocity field, which was subtracted from the observed velocity field to yield a map of the residual velocities. This map is shown in Fig.10; it will be discussed in section 5.

3. Mass models

To each of the measured rotation curves two different models were fitted. The first type of model consisted of a spheroidal "disk" and a spherical "bulge". For the spherical component the mass out to a radius r was described by:

$$M(r) = M_s \cdot \{1 - \exp\left[-(r/r_s)^2\right]\}^{1.5} \qquad (1)$$

For the spheroidal component a polynomial expansion was used for the density. The relevant formulae are given by Schmidt (1965), among others.

A number of different models were fitted for both measured rotation curves, both with and without the spherical component, but it was found for both that a model with the spherical component and an expansion for the density in the disk containing terms in r^0, r^1 and r^2 gave the best fit. Such a model shows solid body rotation in the central part, which, because of the finite resolution of the observations, is always found in the measured rotation curve. It is, however, evident from the l-v map along the major axis, shown in Fig.11, that the rotational velocities near the nucleus may be significantly higher than measured, implying

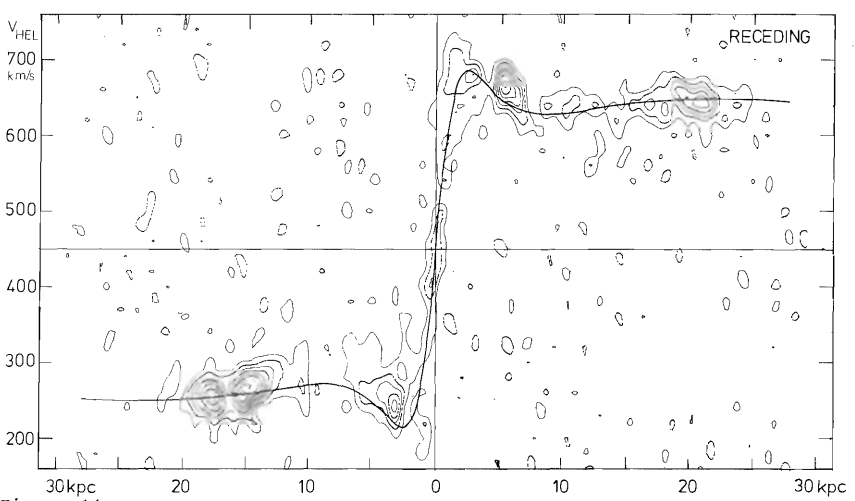

Figure 11.

l-v map along the major axis. Rotation curve no. 1a has been drawn in, after a correction for the inclination. The nucleus is indicated. Note the discrepancy between the rotation curve and the measured HI velocities on the major axis near the nucleus. This is in part due to resolution effects, but the large deviations from circular rotation near the nucleus also play a role in causing this discrepancy. The concentration of HI in the nucleus, near the systemic velocity looks very much like what would be expected from a nuclear disk as the Galaxy. Beam effects could also cause this feature.

a larger central mass concentration.

An axial ratio of 0.052 was assumed for the spheroids, by analogy to similar models of the Galaxy. The exact value does not influence the conclusions of this chapter very strongly. A larger axial ratio would have resulted in a somewhat higher estimate for the total mass of the system. The mass estimate from these "disk-bulge" models is a lower limit since no contribution due to spheroids with a semi-major axis exceeding 28 kpc was included and since the models are quite flat.

The second type of model that was fitted consisted of a sum of two flat disks as described by Toomre (1963). The surface density in such disks is described by:

$$\sigma(r) = (c^2/2\pi G)\cdot a^{2+2n} \cdot \left(\frac{\partial}{\partial a^2}\right)^n (a^2 + r^2)^{-1.5} \qquad (2)$$

The associated circular velocities are given by:

$$\Theta^2(r) = c^2\cdot a^{2+2n}\cdot \left(-\frac{\partial}{\partial a^2}\right)^n \{(r^2/a)\cdot(a^2 + r^2)^{-1.5}\} \qquad (3)$$

The constant c determines the maximum rotational velocity in the disk; a determines the linear scale. Force and density contributions of different "Toomre disks" may be added and subtracted in order to obtain composite models.[1] The factor a^{2+2n} does not occur in the formulae as given by Toomre; it is not essential, but it ensures a faster convergence in model-fitting procedures.

An advantage of models with these Toomre disks is that they allow extrapolation of the rotation curve in a rather natural, though of course not necessarily correct, way.

Also in this case a number of different models were tried for both rotation curves, with the values 0, 1 and 2 for n. Both a and c were determined using a least-squares fitting procedure. The solutions for a and c tended to become unstable if more than two disks were used.

A number of quantities derived from the different models are given in Table 2. Some other quantities are displayed graphically in Fig.12.

4. The mass to luminosity ratio

For the determination of the radial distribution of the mass to luminosity ratio the photometry of Capaccioli (1974) was used, except for the nucleus, the luminosity of which was determined from the photometry published by Chincarini and Walker (1967).

Capaccioli's photometry gives the blue surface brightness as a function of r^*, where r^* is the radius of a circle with an area equal to that enclosed by the relevant isophote. r^* is defined for any type of luminosity distribution, but only if the surface brightness decreases monotonically from the nucleus outwards and if the isophotes are nearly circular in the plane of the galaxy can r^* be converted to a true radius. It can be seen from any photograph that these conditions do not hold for NGC 4258. Since no other photometry was available, I nevertheless had to make the assumption, so that the calculated M/L distribution can only be regarded as indicative. This is all the more true because the extinction correction is not known; following Holmberg (1958) I used an estimate of 0.8 blue magnitudes at all radii.

Capaccioli's extrapolation of the nucleus clearly disagrees with the photoelectric measurements published by Chincarini and Walker. Therefore I fitted a simple model, giving the correct luminosity within the 17" diaphragm (12.76 B-magnitudes) and at the same time fitting the measured points of Capaccioli.

[1] The n-fold differentiation with respect to a^2 is in fact a special case of a repeated subtraction. Because of this it was possible to do the differentiation numerically and to use a fairly large value (0.1) for $\Delta a^2/a^2$ in the process. The advantage of using such a large difference is that the truncation errors only start to become important after the eighth differentiation.

Table 2

Parameters for, and integrated quantities derived from the different mass models.

Quantity	Rotation curve no.1	Rotation curve no.2	Units
1) The polynomial models			
r_s	1.64	1.82	kpc
M_s	4.17	4.77	10^{10} $M_\odot$
Total mass (28 kpc)	1.84	1.91	10^{11} $M_\odot$
Central density	2.4	2.0	$M_\odot pc^{-3}$
Central surface density	6.10	5.67	10^3 $M_\odot pc^{-2}$
Total rotational energy	3.7	4.1	10^{15} $M_\odot km^2 s^{-2}$
Total angular momentum	4.1	4.4	10^{17} $M_\odot$ pc km s^{-1}
2) The Toomre-disk models			
n	1 , 1	0 , 1	
a	26.3, 2.44	19.9, 2.75	kpc
Mass (out to 28 kpc)	2.07	2.25	10^{11} $M_\odot$
" " " 56 "	2.69	3.30	10^{11} $M_\odot$
Central surface density	3.23	3.0	10^3 $M_\odot pc^{-2}$
Rotational energy (28 kpc)	4.34	4.93	10^{15} $M_\odot km^2 s^{-2}$
" " (56 kpc)	5.44	6.95	10^{15} $M_\odot km^2 s^{-2}$
Potential energy (28 kpc)	-1.99	-2.50	10^{16} $M_\odot km^2 s^{-2}$
" " (56 kpc)	-2.21	-3.25	10^{16} $M_\odot km^2 s^{-2}$
Angular momentum (28 kpc)	5.4	6.0	10^{17} $M_\odot$ pc km s^{-1}
" " (56 kpc)	9.7	14.1	10^{17} $M_\odot$ pc km s^{-1}

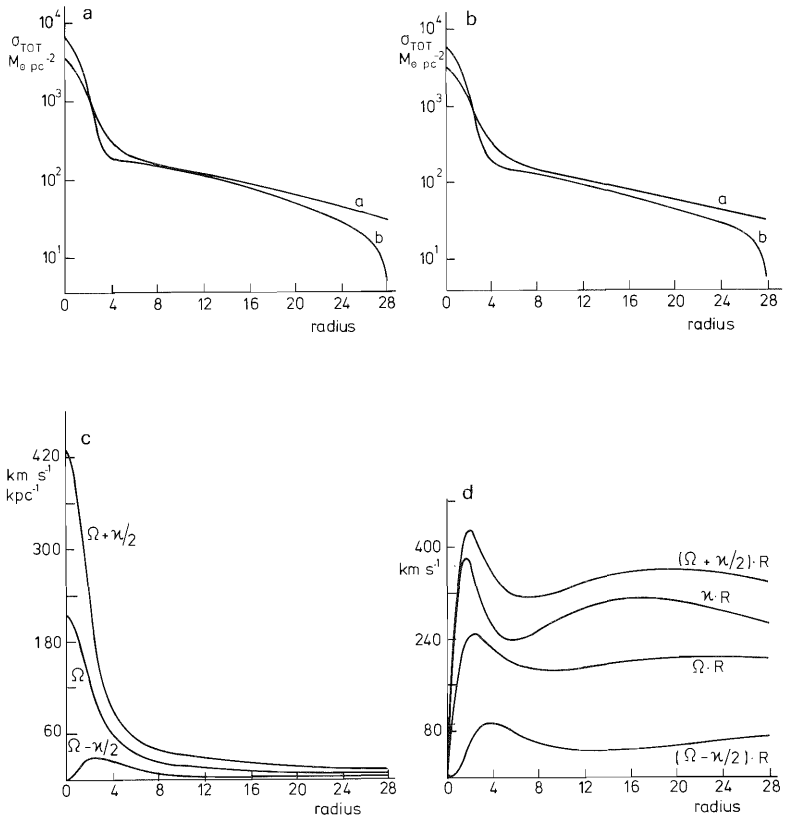

Figure 12.

A collection of curves representing different quantities derived from the mass models that were fitted. Figs.12a and 12b represent the surface densities calculated for the different models. Note that the derived surface densities are much more dependent on the type of model fitted than on the version of the rotation curve used. Also note that for all models the surface density falls off nearly exponentially outside the central mass concentration.

All other curves have been derived from model no.1a alone. Fig.12c shows the behaviour of Ω and $\Omega \pm \kappa/2$. In 12d these angular velocities have been converted to linear velocities again, for the sake of clarity, and $\kappa.r$ has also been added. Though unorthodox this representation is much easier to work with than the usual representation as in Fig.12c.

The model fitted is: $I_n = I_o \exp (-r^*/a^*)$ with $a^* = 3''.44$ and $I_o = 17.32$ B-magnitudes per square arcsec. The integrated luminosity for the nucleus then becomes 12.65 B-magnitudes.

For the mass distribution the Toomre-disk model for rotation curve no.1 was used. Two representations of the M/L distribution are given in Fig.13: the M/L ratio as observed at each radius and the ratio of M to L both integrated out to the given radius. The very low M/L in the nucleus may not be significant; the difference in resolution between the optical observations and the radio observations is much too large to trust M/L here. The peak in M/L between 0 and 4 kpc is quite probably real, but its height is very dependent on the type of mass model and on the rotation curve, which is not well-known in this region. The increase in M/L from 4 kpc outward is certainly real. One could interpret the M/L curve as showing: 1. an over-luminous nucleus; 2. a bulge dominated by older, red stars; 3. a disk with star formation in progress predominantly in the inner parts, becoming dominated by older objects and possibly gas further out.

Fig.14 shows the radial distribution of the ratio of the surface densities

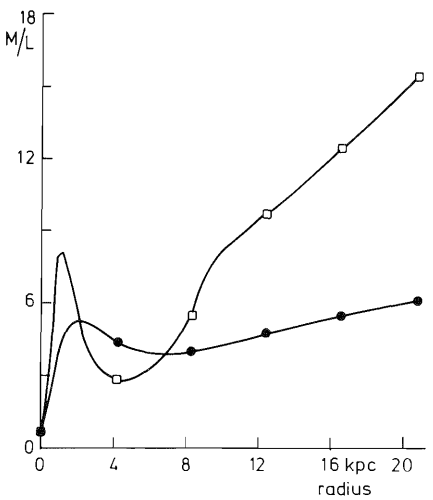

Figure 13.

M/L as a function of radius. The curve labelled with "□" is M/L as determined locally for an annulus; the other curve is the ratio of the mass to luminosity integrated over the part of the disk out to the given radius.
Cappacioli's measurements only go out to $r^* = 6'$, corresponding to r = 21 kpc.

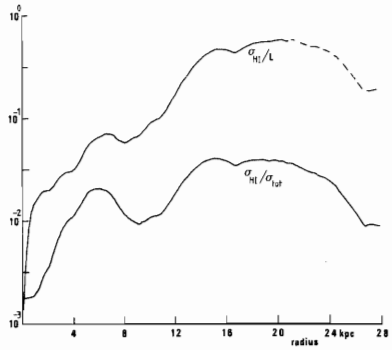

Figure 14.

The ratio of the HI surface density to the total surface density and to the blue luminosity. Neutral hydrogen clearly is only a minor constituent at all radii.

σ_{HI}/σ_{tot} and of σ_{HI}/L. Except for the uncertainties in L the latter quantity is well determined and it is independent of the galaxy's distance. Evidently the HI content of NGC 4258 is rather small even at large radii. One cannot, however, exclude the possibility that much hydrogen is in molecular form. It is also possible that a considerable fraction of the HI is concentrated in optically thick clouds in the very narrow outer arms. An indication of this may be found in the high antenna-temperatures that are observed in these arms, which range up to 40 K in practically unresolved ridges.

5. NGC 4258 as a barred spiral galaxy

5.1 The spiral structure

As can be seen from the photograph in Fig.15 and from the HI maps the spiral structure of NGC 4258 is quite irregular. Fig.16 shows how the spiral arms seem to run. It is clear that no two-sided symmetric pattern exists in NGC 4258. Even if due allowance is made for the fact that the arms may be distorted by a warp, it remains impossible to analyze the spiral structure as a bi-symmetrical pattern. This is most clearly seen when one counts the number of arms on the near and on the far side. While we find at least two arms on the near side outside the lens (arms "B", "E" and possibly a weak continuation of arm "D") only one arm is visible on the far side (arm "B"). In the following I will not try to give a complete analysis of the observed spiral structure; it is very well possible that the observed spiral arms belong to different pattern speeds and multiplicities. Nor is there any reason to assume that they have not been caused by different mechanisms. For NGC 4258 nearly every mechanism which has been proposed for the creation of spiral arms may indeed be responsible for some part of the observed structure. NGC 4258 has a bar, it has a companion, it has an active nucleus which has ejected matter into the plane and it has a warp (Dr. E. Dekker suggested to me that this would also be a possible cause of spiral structure). We will see that there is good evidence that most, or, if they are interpreted as a wave phenomenon, all spiral arms outside the lens are moving away from the center of the galaxy. If they form a long-lived pattern this means that they lie outside corotation. This seems to favour the interpretation of the arms as having been caused by the potential of the bar, or possibly by past activity of the nucleus. In these cases, however, the observed lack of symmetry is rather surprising. In the following paragraphs I will discuss each arm separately.

The spiral arms at the edge of the lens form the most nearly bi-symmetrical pattern in NGC 4258, but even here one cannot be entirely sure. The Northern arm seems to split at the end into a branch that contains only older stars and a branch containing extreme population I constituents and which may connect to the Southern arm. Deprojection shows that the Northern and Southern arms may be part of an oval ring, but that the bright regions indeed are trailing. As has been

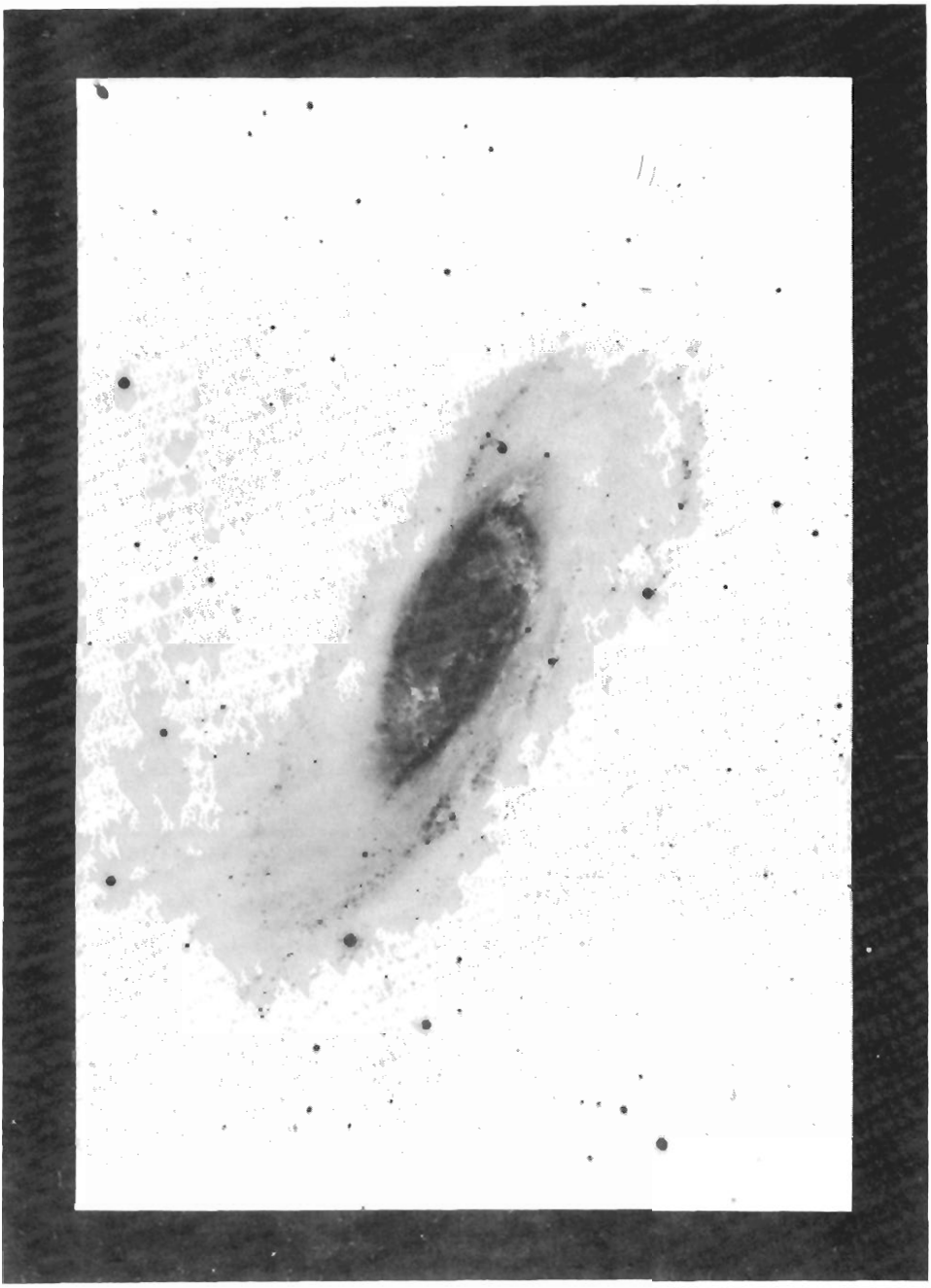

Figure 15.

The photograph used in the overlay in Fig.2 (200 inch, IaO plate, (courtesy A.R. Sandage and W.C. Miller).

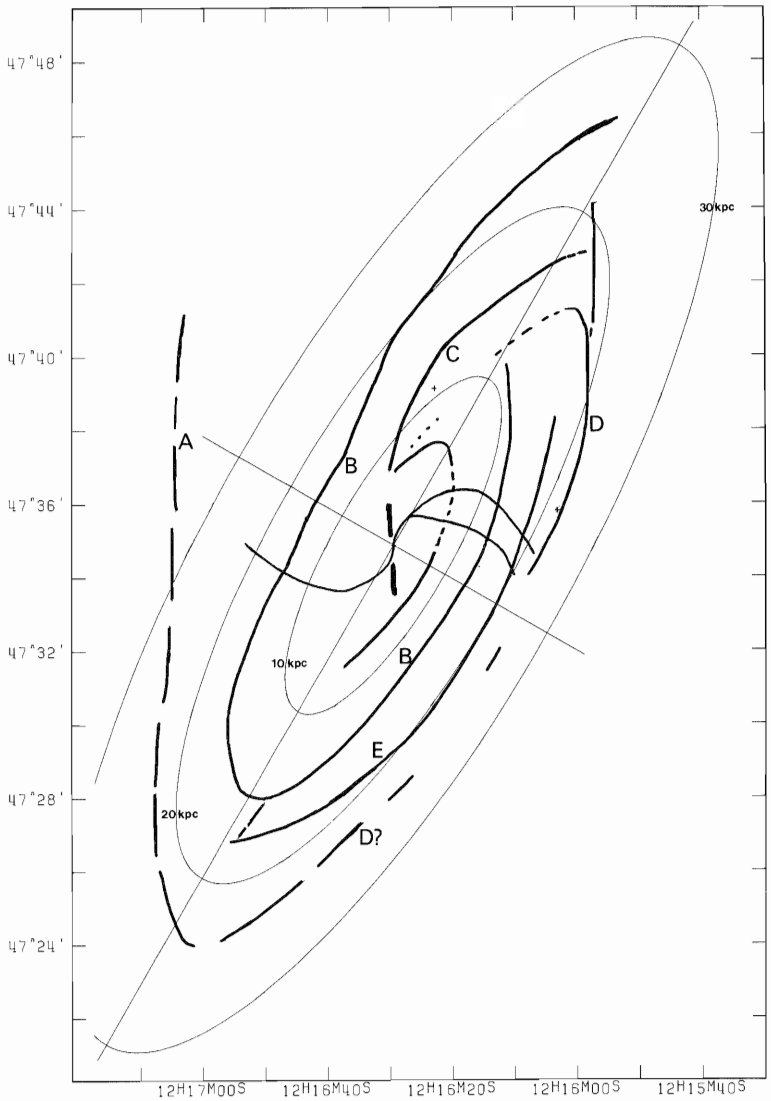

Figure 16.

A rough sketch of the positions of the spiral arms in NGC 4258. The way certain spiral arms have been connected, or not connected, is to some extent arbitrary. The anomalous arms, the bar and the distances in the plane have also been indicated. This sketch is primarily meant as a link between the text and the maps.

observed in section 1 the HI and the dust-lanes lie on the inside of these arms. This, and the fact that the arms are trailing indicates that they lie inside corotation, provided they behave as density waves. The residual velocities observed in the Southern arm, at the S-W side of the nucleus, seem to confirm this conclusion. The velocities in the arm are more positive than outside the arm, i.e. inflow is observed in the arm relative to the surrounding gas, which itself already has a considerable inflow velocity.

As observed in section 1, the dust-lanes in arm "B" seem to lie at the outside edge of the arm. Deprojection shows that this arm is probably trailing. This would indicate that it lies outside corotation. No supporting evidence is found for this conclusion in the residual velocity field, so that it is not very firmly based.

For the arms marked "C" and "D", which may or may not be connected, the situation is somewhat different. In these arms no dust-lanes are observed, but the velocities in the arms are very clearly different from those outside. The observed residuals are positive for arm "C" which lies on the far side, and negative for arm "D" which lies on the near side of the galaxy. Like the other arms in NGC 4258 "C" and "D" are trailing, but where the others are tightly wound "C" and "D" are very open, so that little doubt can exist about their sense of winding. These arms certainly lie outside corotation. This is also confirmed by the behaviour of the velocity residuals at the Northern end of arm "C"; the region with the positive residuals is seen to cross to the outside of the arm, i.e. to form a more open pattern than that of the density. This behaviour is expected outside corotation, both for trailing and for leading arms. Inside corotation the residual velocities should show a more tightly wound pattern than the densities (refer to chapter 5, section 3).

The evidence that arm "E" lies outside corotation is weaker. The velocity residuals are clearly more negative in the arm than outside and there is also evidence that the HII regions lie on the inside edge of the HI arm, but the sense of winding is uncertain.

If the spiral arms are interpreted as density waves, not only the corotation radius, but also the Lindblad resonances are important. Even if, as in NGC 4258, the rotation curve is known, and a guess can be made concerning the position of the corotation radius, it is not possible to pin-point the Lindblad resonances immediately. To determine their positions it is also necessary to know the multiplicity of the arms. Furthermore one needs to make the assumption that the density-wave pattern rotates as a solid body. In principle it must be possible to have a pattern that slowly winds up. It is interesting to note, however, that the gap between the arms "C" and "D" occurs approximately at the position where the outer Lindblad resonance is expected if arm "C" begins at the corotation radius.

5.2 The bar

Though classified SAB(s)bc by De Vaucouleurs et al. (1976) it is not generally accepted that NGC 4258 is a barred spiral galaxy. Of course, NGC 4258 presents a very different picture from a classical barred spiral like NGC 1300, but there is ample evidence that the dynamics of the central region of NGC 4258 is indeed dominated by an elongated or oval structure. In sections 1 and 2 some features have been pointed out in the integrated HI map and in the velocity field that are suggestive of a bar. However, one could also suppose that these features are related to the anomalous arms. For the HI bar such an explanation can indeed apply; in that case one has to assume that the relative maximum density of HI observed is caused only by a lack of HI in the region of the anomalous arms and the associated plateaux. It is only somewhat surprising then that the observed maximum is so narrow.

In order to obtain a better insight into the observed discontinuity in the velocity field we should study the l-v maps shown in Fig.5. From these maps it is

evident that indeed a very steep velocity gradient is present. Within approximately one beam size the velocity of the gas changes from 180 km s^{-1} to 500 km s^{-1} (map at 32" S-E). Whereas it is difficult to decide whether the former velocity differs very much from the local circular velocity, the latter can never correspond to circular rotation because the difference from the systemic velocity has the wrong sign. Even if one wants to maintain that the observed velocity discontinuity or shock is associated with the anomalous arms, the fact remains that the most evidently deviant velocities in the central region lie well away from the anomalous arms, in a region that, according to the expulsion model, can never have been influenced by the anomalous arms. This implies that, independent of the question as to whether the velocities in the anomalous arms are abnormally high, a very similar flow pattern would have been observed if these arms had not existed. Therefore I will assume in the rest of this section that the observed velocities have not been influenced by the anomalous arms.

Now that it has been shown that the anomalous arms cannot be the sole cause of the observed velocity deviations the question remains whether a bar can be the cause. Considering the present state of the theory of barred spirals and the small number of observations available it is clear that this question cannot now be answered definitively. However, a qualitative comparison with the available data certainly indicates that the bar hypothesis is promising.

It is intuitively clear that the gas, though not necessarily the stars, in a bar should move along oval stream-lines. This intuitive idea is indeed confirmed by gas-dynamical calculations, e.g. as published by Huntley, Sanders and Roberts (1978). Figure 17 shows a graphical analysis of the influence such a flow will have on the observed velocities in a galaxy: the iso-velocity contours will not be parallel to the minor axis of the galaxy, but they will tend to follow the bar. Although the exact shape of the iso-velocity lines will be strongly dependent on the details of the gas flow, the qualitative picture will be the same as for this simple model. In this interpretation the velocity discontinuity that is observed in NGC 4258 corresponds to the shock that can be recognized in the gas flow diagrams presented by Huntley et al. In section 6 a simple model for the gas flow in a bar potential will be analyzed in more detail.

Confirmation that the observed velocity field can be explained by a bar also comes from the observations of Peterson et al. (1978) of the barred spiral galaxy NGC 5383. Also in this case one observes that the iso-velocity contours closely follow the bar and that the position angle of the line of nodes that would be derived from the flow in the bar differs considerably from that which would be derived from the flow in the outer parts of the galaxy.

If the observed gas flow in NGC 4258 can indeed be explained as the response to the potential caused by an elongated structure, the question arises as to whether there is any observational evidence that such a structure exists. Indirect morphological evidence can be found in the deprojected integrated HI map in Fig.7. In this picture the HI distribution, which we have seen to follow the optical structures so closely, suggests a O-type barred spiral.

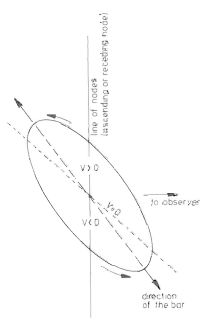

Figure 17.

A schematic representation of the oval flow expected in a bar. The flow is drawn as it would be in the plane; the observer is assumed to be to the right, but out of the plane. Since no z-motions are assumed, the radial velocities towards the observer will only contain information on the velocities perpendicular to the line of nodes.

Direct morphological evidence is found in the large discrepancy between the projection parameters that have been determined geometrically for the lens (Danver, 1942; Capaccioli, 1973) and those that have been determined from the velocity field of the outer parts of the galaxy. If we assume that NGC 4258 is perfectly flat and that the correct projection parameters are those determined from the velocity field, we can derive the shape of the lens from the apparent, geometrically derived projection parameters. If we do this exercise we find the lens to be an oval structure with an axial ratio of 3:2 and with its long axis at position angle $17^{o} \pm 3^{o}$. If we further assume that the geometrically derived inclination has been underestimated by 2^{o} due to the finite thickness of the lens we find an axial ratio of 7:5 and a position angle of $10^{o} \pm 3^{o}$.

Concluding, the following model is proposed for the gas flow in the central part of NGC 4258. An extended, slightly oval, structure that we observe as the lens causes the potential in the central region of NGC 4258 to be non-axisymmetric. The gas, which forms only a minor constituent of the total mass in this part of the galaxy, responds to this potential by forming a very narrow bar, which we observe in the HI, together with the associated large deviations from circular rotation. In this bar star formation is in progress, as may be concluded from the enhanced blue luminosity in that part of the lens (refer to the isophotes published by Capaccioli) and the HII regions that can be recognized in this region on Hα photographs (e.g. Deharveng and Pellet, 1970).

6. A model for the bar

In chapter 5, section 4 a simple method is outlined to study the gas flow in a slightly perturbed, but otherwise axisymmetric potential. In essence it is an epicyclic analysis with the inclusion of a damping term ($\ddot{\vec{x}} = -D\dot{\vec{x}}$) and a term describing the influence of pressure along a flow-line. These two terms are the simplest terms defensible on physical grounds that allow the solution to be studied near the resonances. Using this method a model was constructed resembling the bar of NGC 4258.

The unperturbed potential was derived from rotation curve no. 2a; the assumed perturbation was of the following form:

$$\Delta\Phi = \phi \cos\left[2(\theta - \theta_{o} - \omega t)\right] \cdot (r/r_{p})^{2} \cdot \left[1 + (r/r_{p})^{2}\right]^{-2.5} \qquad (4)$$

with $\phi = 2.65\ 10^{4}$ pc^{2} My^{-2}, so that $|\Delta\Phi| \leq 4.93\ 10^{3}$ pc^{2} My^{-2}; r_{p} =1420 pc and $\omega = 0.034$ My^{-1} (1 My = 10^{6} year; 1 pc My$^{-1} \simeq 1$ km s^{-1}). The value for ϕ was chosen as large as possible without severely violating linearity in order to maximize the visibility of the effects. The amplitude of the velocity deviations in the model is still much smaller than those observed in reality.

In the solution a value for the damping term D of 0.005 My^{-1} was chosen; the velocity of sound was set to 22.4 pc My^{-1}. This latter quantity determines the pressure; a rather large value had to be chosen because the effects of the pressure were only included partially. For the gas surface density in the unperturbed disk the observed annular means from Fig.3 were used.

The simulated HI map, the velocity field and the residual velocity field are shown in Figs.18 through 20. These figures are to the same scale as the observed maps in other figures; no attempt was made to simulate the effects of the WSRT beam. The flow pattern in the innermost region of the model is shown in Fig.21. The map is on a different scale and has not been projected. It clearly shows the expected oval flow.

Some features in the model bear a striking resemblance to what is observed in NGC 4258. That the bar is present in the surface density map is not really interesting; the model was designed to reproduce it. Far more interesting is the fact that the narrow spiral arms at the edge of the lens have been reproduced so accurately. In the model these arms lie at corotation and are caused by a rapid change in the orientation of the flow lines. But turning to the residual velocity field, we see that the velocities in the arms have not been reproduced. A more accurate analysis of the gas flow than that used here is needed to determine

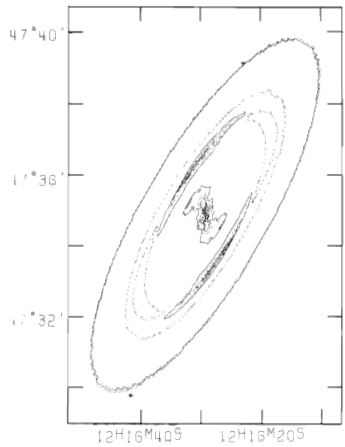

Figure 18.

The surface density map derived from the bar-model discussed in the text. The contours lie at (4.4, 8.8, 17.6, 26.4, 35.2, 44.0, 52.8) × 10^{24} H-atom m^{-2}. The position angle of the driving potential in the plane, relative to the line of nodes was chosen to be $65^{o}.3$.

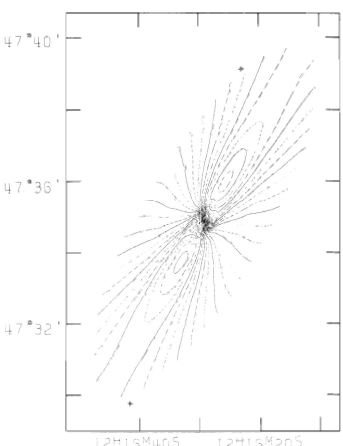

Figure 19.

The bar-model velocity field. Contours have been drawn at -237.5(19)237.5 km s^{-1}.

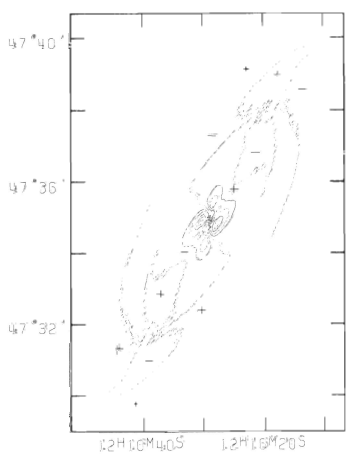

Figure 20.

The residual velocity field for the bar-model. This velocity field has been calculated by subtracting the velocity field of a model with a zero-amplitude driving potential from the velocity field in the previous figure. The contour values are the same as used in Fig.10.

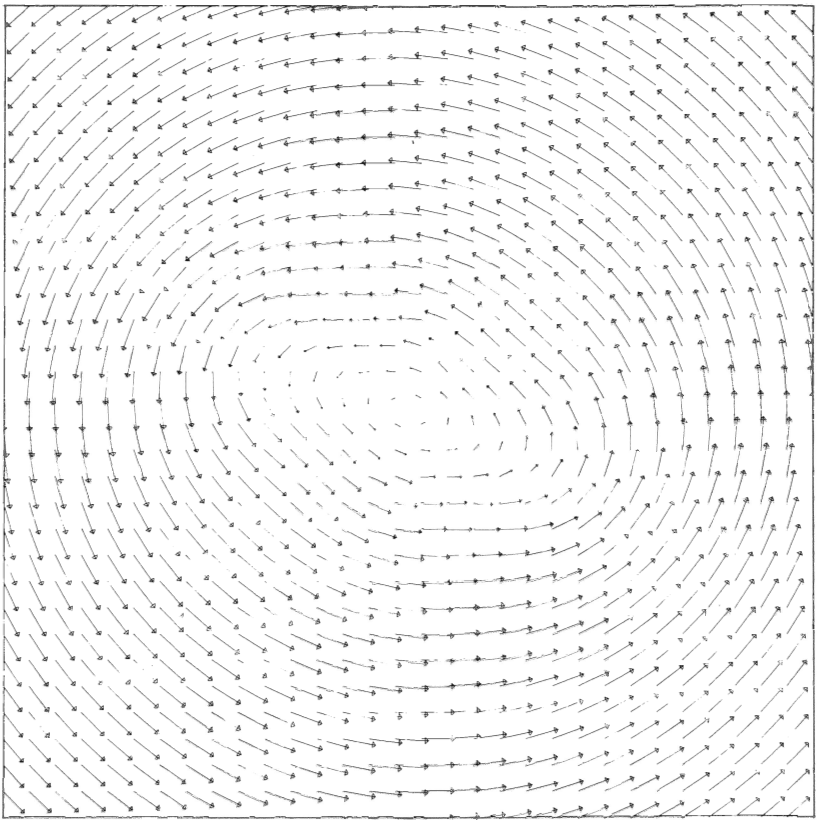

Figure 21

A vector plot of the velocities associated with the bar-model. Each arrow has its base at a grid-point and a length and a direction proportional to the velocity at that grid-point.

whether the observed arms are indeed related to the oval structure. The residual velocity field shows one more interesting detail: the residuals near the nucleus are such that, if a rotation curve had been determined from the model velocity field, it would have given higher velocities near the nucleus than were used as input to the model.

Though far more regular than the observed velocity field, the model velocity field shows a similar behaviour in the region of the bar. Because a linear model was used the "shock" has not been reproduced, but the iso-velocity contours show a similar inclination to the minor axis. If one compares the velocity fields in detail one can even identify the "bumps" on the contours near the nucleus. These bumps are very clear in the Hα velocity field published by Van der Kruit (1974), but although it seems possible to explain them qualitatively as being due to the bar, I am not sure that they can be explained entirely in this manner. It may be that not the very low rotational velocities in the central region are related to the anomalous arms, as Van der Kruit suggests, but the very high velocities. Ballistic models as in the example in chapter 4, section 4, suggest that these high velocities could be due to the gas in the anomalous arms passing the

pericenter in highly elongated orbits. This interpretation would also seem to fit in better with the relative position of velocities and arms.

7. Conclusion

We have seen that, slightly adapting Bosma's statement quoted in chapter 1, NGC 4258 can be considered "the type example of an oval distortion in a galaxy", anomalous arms, or no anomalous arms. NGC 4258 is not unique in this respect, however. The Seyfert galaxy NGC 4151 as described by Bosma et al. (1977, 1978) for instance is strikingly similar in appearance. Except for the obvious difference in inclination ($i = -21^{\circ}$ for NGC 4151) and resolution, the integrated HI map, the velocity field and the flat rotation curve are very much like those of NGC 4258. Even the optical picture with the bright, oval lens showing some spiral structure and the narrow, irregular outer arms is similar to what is seen in NGC 4258. Moreover, if, in view of the small inclination, anything of the sort can be inferred from the velocities in the outer arms of NGC 4151 it would appear that they lay outside corotation. Bosma's remark concerning the association of activity and bars in spirals at the end of his section IV is given extra significance by the bar in NGC 4258. It seems that two ingredients are necessary for the spectacular activity observed in Seyfert galaxies and inferred for NGC 4258. The first of these is an energy source, or at least a machine that can produce the necessary energy if properly fuelled. Here one could think of one of the variety of condensed, massive objects proposed by various authors. The other would be an amount of gas near the nucleus sufficiently large to provide the fuel and to produce the spectacular effects. In the process the amount of gas in the nuclear region will diminish as some of it is consumed as fuel and some is expelled. A bar seems to be able to replenish the gas as it can pump gas from the disk into the nucleus.

De Bruyn (1976) reports that M 81 contains a variable, i.e. very small radio source, which indicates that M 81 may be an example of a galaxy that does contain a machine, which is fuelled albeit at a relatively low level, but where the amount of gas in the central parts is much too small to produce phenomena as spectacular as in NGC 4258 or in Seyfert nuclei. M 81 lacks a bar that could pump gas into the central region.

References

Albada, G.D. van; Shane, W.W.: 1975, *Astron. Astrophys. 42*, 433

Beaujardière, O. de la; Kazès, I.; Squéren, A.M. le; Ngyn-Quang-Rieu: 1968, *Ann. Astrophys. 31*, 387

Bruyn, A.G. de: 1976, Ph.D. dissertation, Leiden University

Bruyn, A.G. de: 1977, *Astron. Astrophys. 58*, 221

Burbidge, E.M.; Burbidge, G.R.; Prendergast, K.H.: 1963, *Astrophys. J.138*, 375

Capaccioli, M.: 1973, *Mem. del. Soc. Astron. It. 44*, 417 [(BBP)

Chincarini, G.; Walker, M.F.: 1967, *Astrophys. J. 149*, 487

Danver, C.G.: 1942, *Ann. Obs. Lund 10*

Deharveng, J.M.; Pellet, A.: 1970, *Astron. Astrophys. 9*, 181

Heeschen, D.S.; Wade, C.M.: 1964, *Astron. J. 69*, 277

Holmberg, E.: 1958, *Medd. Lunds Astron. Obs., Serie II*, 136

Huntley, J.M.; Sanders, R.H.; Roberts, W.W.: 1978, *Astrophys. J. 221*, 521

Jong, M.L. De: 1965, *Astrophys. J. 142*, 1333

Kruit, P.C. van der: 1974, *Astrophys. J. 192*, 1

Kruit, P.C. van der; Oort, J.H.; Mathewson, D.S.: 1972, *Astron. Astrophys. 21*, 169 (KOM)

Lequeux, J.: 1971, *Astron. Astrophys. 15*, 30

Maslowski, J.: 1972, *Acta Astron. 22*, 227

Peterson, C.J.; Rubin, V.C.; Ford, W.K. Jr.; Thonnard, N.; 1978, *Astrophys. J. 219*, 31

Rogstad, D.H.; Lockhart, I.A.; Wright, M.C.; 1974, *Astrophys. J. 193*, 309

Rogstad, D.H.; Rougoor, G.W.; Whiteoak, J.B.: 1967, *Astrophys. J. 150*, 8

Rots, A.; Shane, W.W.: 1975, *Astron. Astrophys. 45*, 25

Schmidt, M.: 1965, *Galactic Structure= Stars & Stellar Systems V*, ed. A. Blaauw, M. Schmidt, Univ. of Chicago Press, Chicago & London

Toomre, A.: 1963, *Astrophys. J. 138*, 385

Toomre, A.; Toomre, J.: 1972, *Astrophys. J. 178*, 623

Vaucouleurs, G. de; Vaucouleurs, A. de; Corwin, H.G. Jr.: 1976, *Second Reference Catalogue of Bright Galaxies*, Univ. of Texas Press, Austin & London (RCBG II)

CHAPTER 4 THE ANOMALOUS ARMS

Summary

An analysis of the anomalous arms is given. It is demonstrated that the observed properties of these arms are consistent with the expulsion hypothesis for their origin, but the kinematical data being sparse, the verification of the theory is necessarily incomplete.

1. Introduction

This chapter is devoted to the analysis of the available data on the anomalous arms of NGC 4258. As we have seen in chapter 3 the large deviations that are evident both in the HI and in the optical observations can for a large part be explained by assuming that NGC 4258 is a barred spiral, an assumption for which there is additional supporting evidence. This complicates matters considerably as far as the anomalous arms are concerned because it means that it is very difficult to separate the deviations from circular rotation associated with the anomalous arms and those that are due to an aspect of NGC 4258 that does not make it exceptional. It is clear from the narrow-band Hα observations of Courtès et al. (1965) that the amplitude of the velocity deviations in the anomalous arms does not exceed that of those observed in the bar region. In chapter 6 we shall see that if much larger velocity differences with the surrounding medium occur anywhere in the anomalous arms we cannot expect to observe Hα emission from the region concerned; the gas would either be too hot and too tenuous, or too highly compressed and hence too cold to emit observable Hα radiation. This means that two types of velocity deviations have to be separated that both have a comparable amplitude of the order of 200 km s^{-1}. Neither of the effects concerned is completely understood to date, but we have the advantage that for one the velocity deviations should be correlated with an emission feature (the anomalous arms) and that for the other (the bar) at least the general features can by now be predicted theoretically. Optical measurements with a good velocity resolution and a complete coverage of the central region will be needed to separate both components and to determine the amplitude of each individually. We have seen that already, from the combined results of HI observations, model fitting for the bar and the Hα observations of Van der Kruit, some indications concerning the dynamics of the anomalous arms have been obtained. Strangely, not the apparently deviant velocities, but the seemingly normal velocities in the central region would have to be linked with the anomalous arms... As will be demonstrated, this and all other observed features of the anomalous arms can be explained with the expulsion hypothesis. Since no other plausible explanation is available I will adhere to this hypothesis in the rest of this chapter.

In section 2 of this chapter the morphology of the anomalous arms as observed in 1412 MHz continuum with the WSRT is discussed. Though these are in principle the same kind of data as those obtained by KOM, the dynamic range and the sensitivity of the WSRT have been improved so much over the past six years that a far more detailed analysis has become possible. In sections 3 and 4 the Hα data obtained by Deharveng and Pellet and those of Van der Kruit will be discussed in some detail, and a simple model will be presented. Section 5 will deal with the polarization data; section 6 with the spectral index.

2. Inferences from the anomalous arm morphology

In the continuum map published by KOM and in the new continuum map shown in Fig.1 of chapter 2 the front edge of the continuum arms appears to be unresolved. In order to obtain a better insight into the actual steepness of this edge an attempt was made to construct a map with a higher effective resolution than is achieved with the standard grading. Such an improvement can be obtained by using the clean and restore technique (Högbom, 1974; Harten, 1974), but the gain in resolution attainable in practice is severely limited by noise and dynamic range effects because of the lack of information at the higher spatial frequencies (the gain that can be attained is due to the use of information not used in the normal mapping process, namely that all sky intensities should be positive). The highest resolution that proved to be feasible with the available 1412 MHz data is 18" × 24" (full width to half power). The corresponding map is shown in Fig.1; a radio-photo of the map after deprojection is shown in Fig. 2.

From the enhanced resolution map it is clear that the front edge of the anomalous arms remains unresolved and that the apparent blending of the anomalous arms into the plateaux in the other 21 cm continuum maps is due to beam effects. The radio arms, like the associated Hα arms, are very narrow structures.

Both anomalous arms split near the edge of the bright inner region, or lens, of NGC 4258. For the S-E arm this is clear from the Hα photographs as published by Deharveng and Pellet (1970). For the N-W arm, which though the brighter in radio continuum is the weaker of the arms in Hα , this splitting is very easily visible in the 21 cm continuum maps. From the Hα photograph of Deharveng and Pellet it is clear that the separation of the branches of the S-W arm is much larger than their widths. A plausible explanation for this fact is that the two branches were created by separate events, presumably expulsions of matter by the nucleus as in the model presented by KOM.

If the nucleus can eject matter twice, there is no reason to assume that it could not do so more often. If we carefully examine the plateaux in Fig.1 we can indeed find suggestions of some radial structures. The brightest of these have been marked in the figure. If these structures are real we have in fact observed a

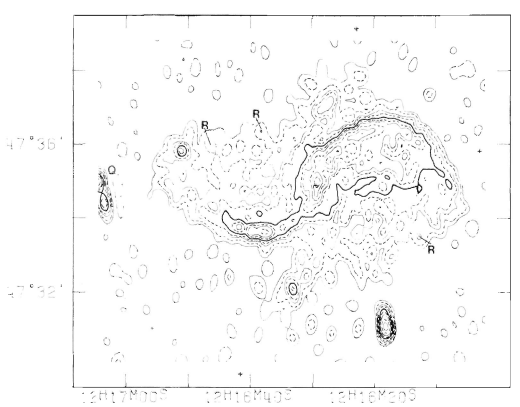

Figure 1.

The 1412 MHz enhanced resolution map (18" × 24" FWHP beam). Contours have been drawn at (-1, -0.5, 0.5, 1, 2, 3, 5 (heavy),7.5, 10, 15, 20, 25) × 1 K; alternating positive contours and all negative contours have been dashed. The double source marked Q has been identified with a 22.5 mag. quasar by De Ruyter et al. It lies in the weak outer HI arm "A". Some seemingly radial structures in the plateaux have been marked with an R.

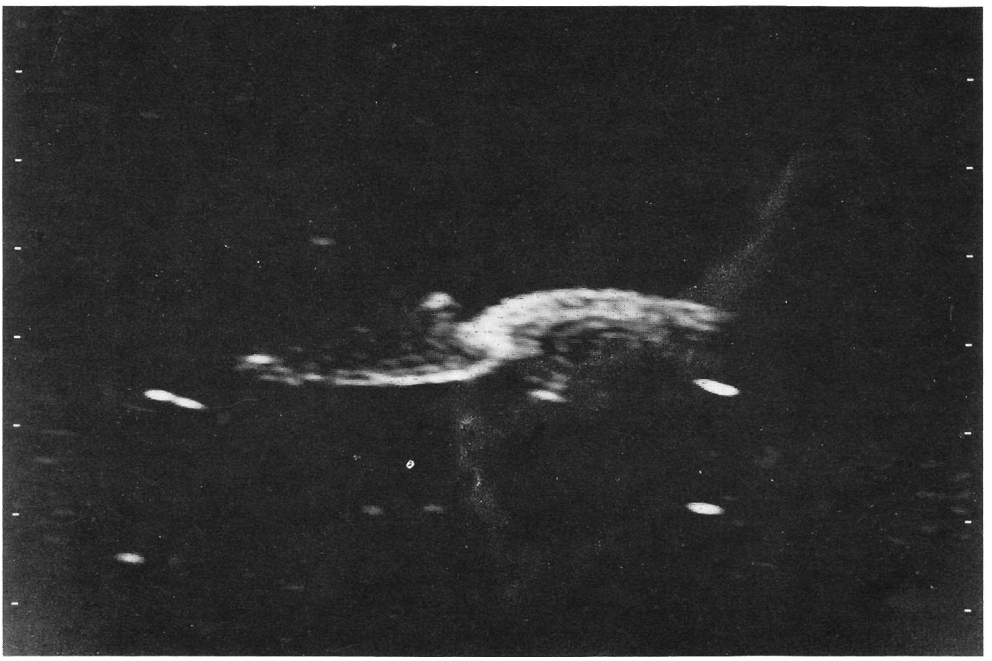

Figure 2.

Radio-photo of the deprojected enhanced resolution map of Fig.1.

phenomenon that bears a striking resemblance to what is seen in head-tail radio galaxies. Both types of galaxies display a nucleus that is intermittently active, ejecting something in two diametrically opposed directions. In both types of galaxies the time sequence of these ejections is converted into a spatial sequence because the ejecta encounter a moving medium, i.e. an intra-cluster medium for the radio-tails and a rotating disk in this case.

The phenomenon in NGC 4258 also bears some resemblance to what takes place in the collimated double radio sources. Firstly we have the narrowness of the anomalous arms, which is strongly reminiscent of a collimated double. This narrowness is, however, probably in part due to the lateral compression that the ejected matter must have experienced as it acquired angular momentum in the plane of NGC 4258 (a similar but probably unrelated phenomenon was observed by Van Breugel and Miley, 1977). The second analogy with the collimated double is the apparent constancy of the direction into which the ejection took place. Simple model calculations show that, due to the flat rotation curve of NGC 4258, the outer parts of the anomalous arms must have been displaced in such a way that they remained very nearly parallel to the direction in which the ejection took place. If the hypothesis that the plateaux are due to later ejections is correct, the back edges of the plateaux, i.e. the edges where the anomalous arms do not lie, mark the direction into which the most recent ejections took place. This direction cannot be precisely determined because the emission is too faint, but it seems no different from the direction of the original expulsion which created the bright anomalous arms. The above reasoning also requires the assumption that the ejection of matter by the nucleus has continued (nearly) to the present time.

In principle it is also possible to explain the plateaux by assuming that the direction of the expulsion rotated faster than the disk of the galaxy and that the anomalous arms were created after the plateaux. The explanation of the relatively straight back edge of the plateaux - as compared to the curved form of the anomalous arms - and the very weak and nearly radial structures in these plateaux poses some extra problems in this case.

The assumption that the direction of ejection is constant in time also poses an interesting problem. The explanation that is generally advanced for the constancy of the expulsion direction observed in double radio sources is that the expulsion takes place along the rotation axis of some massive object. In NGC 4258, however, the expulsion must have been very nearly perpendicular to the rotation axis of the galaxy as a whole (refer to chapter 1). This would then imply that the nucleus of NGC 4258 contains a massive object with an axis of rotation perpendicular to that of the galaxy itself. Such a situation probably only can arise as the chance result of some random process. The fact that out of some ten or twenty galaxies with active nuclei sufficiently nearby that we could observe the effects, only two examples are known of galaxies where bi-symmetrical ejection of matter into the plane has taken place (NGC 4258 and NGC 2146[1]) is in agreement with the conjecture that the ejection axis generally does not lie near the plane of the galaxy.

The large differences in structure between NGC 4258 and other active galaxies are not due then to the ejection mechanism but to the density of the medium encountered by the ejecta, and the total energy involved. As we will see in chapter 6 gas clouds travelling at high velocities through a dense medium suffer a violent thermal instability and will collapse very quickly to cold, small blobs of gas. It is interesting to note that molecular, i.e. dense and cold, clouds appear to be ejected from the nucleus of our own galaxy (Oort, 1977), though not with velocities as high as would be needed in NGC 4258. At extra-galactic distances such clouds are hard to detect, however. Because the gas density in spiral galaxies generally is quite high it is probable that any matter that is ejected quickly condenses into such blobs, which may travel large distances before re-expanding. Only by the damage that they do if they happen to travel through the disk of a galaxy can we know that something has been ejected. Such a collapse is much less likely to occur in the tenuous medium of an elliptical galaxy, while the composition and certainly the energy content of the ejecta in those ellipticals that are associated with strong radio-sources also seem to be very different from those in spirals.

The most puzzling aspect of the anomalous arms is their remarkable smoothness. Whether they cross a spiral arm, or an interarm region, their brightness remains nearly constant and their outline smooth. This extreme smoothness is difficult to reproduce in model calculations, quite probably due to numerical effects. It seems, however, to be a natural consequence of the expulsion of matter by the nucleus: if the ejecta travel more than one wavelength of the spiral pattern radially through the disk the effects on the resulting anomalous arm of each individual normal arm, or interarm region should largely average out.

Concluding we can state that the appearance of the anomalous arms and the associated plateaux is consistent with the assumption that they have been created by a repeated expulsion of matter out of the nucleus into the plane of the galaxy. Each of the later, smaller expulsions that created the plateaux must have had approximately the same spatial direction as the two initial large expulsions in which the anomalous arms find their origin.

3. An estimate of the age of the anomalous arms

Fig.3 shows a sketch of the region around the S-E anomalous arm as visible on the Hα photograph published by Deharveng and Pellet. One of the remarkable features

[1] Refer to De Bruyn (1976, 1977) who also includes NGC 3079 as an example.

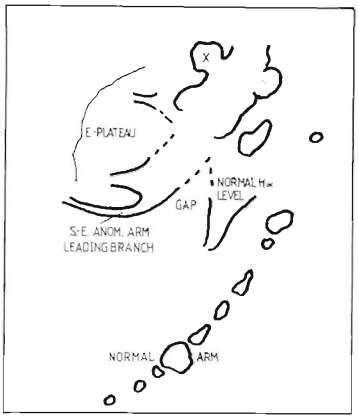

Figure 3.

Sketch made from Hα photograph published by Deharveng and Pellet (1970). The nucleus lies approximately between X and Y.

in their photograph is the sharp boundary between the gap in front of the anomalous arm and the region indicated as having a normal Hα emission level. These characterizations of the observed features follow naturally from the expulsion hypothesis. Before the expulsion of matter from the nucleus took place the Hα emission level in the entire lens around 4 kpc from the nucleus must have been comparable to that of the region said to have a normal emission level. When a powerful jet of matter with very little angular momentum was expelled from the nucleus, the gas in front of the region (in the sense of rotation of NGC 4258) where the gas travelled through remained uninfluenced. While the matter in the jet was being slowed by the interaction with the gas in the disk, it in turn slowed the rotation of the gas with which it collided. From the appearance of the anomalous arms and the gap in front one would say that in fact little gas was able to flow through the foremost branches of the anomalous arms. In this way the anomalous arms were created as very narrow ridges, rotating slowly at first and picking up speed as more matter ran into them from behind. Due to the lack of angular momentum the gas in the inner region would describe very excentric orbits, bringing it close to the nucleus again, overtaking the initially unperturbed gas and thus closing the inner part of the gap in front of the arms. While this process was taking place smaller discharges from the nucleus created the plateaux.

It will be clear from the above description that the boundary between the gap and the region with normal emission must have lain there where the jet passed when the anomalous arms were formed. As argued earlier, this direction can be inferred from the present morphology of the arms. Since the angle through which the boundary has rotated and the local angular velocity are known an estimate can be made of the time elapsed since the original expulsion: 45 ± 20 My. The very large uncertainty has a number of causes: the distance to most external galaxies is inaccurately known; the rotation curve around 4 kpc is not very well determined due to the large non-circular motions in the region and these same non-circular motions cause the rotation curve to be a dubious measure for the travel time between two positions in the plane; the large inclination of NGC 4258 greatly enlarges the error of any angle in the plane measured near the major axis.

This age is comparable to, although somewhat larger than, the time required for radiation losses to show up in the spectrum (De Bruyn, 1976, p.54). The spectrum at higher frequencies is not well enough known to permit us to decide whether such losses have been compensated by more recent (in-situ) acceleration.

4. A model for the anomalous arms

Some calculations have been made in order to get a better insight into the behaviour of gas ejected from the nucleus of a spiral galaxy. From the analysis in chapter 6 it is concluded that the gas injected into the medium of a disk galaxy would probably very quickly condense into a large number of small, cold cloudlets. Such a collection of cloudlets can be described more accurately with a ballistic, snow-plow type model than by gas-dynamical calculations that generally lack so much in resolution that the behaviour of such cloudlets cannot be simulated. The ideal combination would be a ballistic model for the ejecta and a gas-dynamical model for the disk medium.

The scheme used contains a model for the disk based on the analysis in chapter 5, section 3 combined with a simple model for the z-distribution of the gas. Into this model a narrow stream of "cloud complexes" can be injected any number of times at an arbitrary angle with the plane and with an arbitrary mass and velocity distribution. The orbits of the cloud complexes are calculated, taking into account the fact that the disk is swept clean in the process. It is assumed that at the injection each complex has an expansion velocity equal to two percent of its translational velocity. If a complex expands beyond a certain diameter, which is always smaller than the smallest scale-size in the disk model, it is split into five new complexes. If the total number of cloud complexes exceeds a specified maximum, their number is reduced by combining complexes that differ sufficiently little in position and velocity into one new complex. The maximum number of complexes allowed generally is chosen to be quite large. In the example presented below it had been set to 3600.

Figs.4 and 5 show the velocity field and the density distribution in a disk with one anomalous arm in one of the models calculated, 30 My after the injection of the clouds from the nucleus. Only the inner 12 kpc were included in the calculation in order to obtain optimal (100 pc) resolution, and only one anomalous arm was introduced in order to save computer time. Since the background disk is treated as two identical halves the effects of the sweeping are visible on both sides of the disk. The arm was created by ejecting 50 cloud complexes with velocities uniformly distributed between 500 and 1186 km s^{-1} and masses proportional to V^3 and 40 complexes with velocities between 400 and 1180 km s^{-1} and masses proportional to V^2 , in the direction ϑ=260°, at an angle of 4° with the plane into the model galaxy. The total mass of the injected clouds was 6.4 $10^6 M_\odot$, the total momentum 6.2 10^9 $M_\odot$ km s^{-1} and the total kinetic energy 3.0 10^{12} $M_\odot km^2 s^{-2}$ = 6.1 10^{48}J. The following results are noted:

-- As in Van der Kruit's measurements, the velocity in the simulated anomalous arm, near the nucleus, is more like that expected for circular rotation than is that in the surrounding medium.

-- In the model the velocity difference between the gas in the disk and that in the anomalous arm is rather smaller than that observed by Van der Kruit. This is probably due to the velocity deviations associated with the bar in the disk model not being high enough, and to the gas in the anomalous arm in the model having gathered too much angular momentum per unit mass, so that the orbits of this gas are not sufficiently eccentric to lead to really high velocities at the peri-centers.

-- The inner part of the anomalous arm in the model does not come as close to the nucleus as observed in the actual galaxy. This also indicates that the orbits are not sufficiently eccentric. More eccentric orbits could have been created by injecting more gas at lower velocities or at a somewhat larger angle with the plane, so that it would have gathered less angular momentum per unit mass before falling back towards the nucleus.

-- Like the real anomalous arms, the model arm is very smooth even though it runs through regions with widely varying densities. It is also very narrow.

-- The bulk of the ejecta quickly forms a large cloud complex travelling through the disk. This complex has only just left the zone of computation, which indicates that the highest velocities in the originally ejected clouds were much

too low; the ejecta could never yet have reached the edge of the real galaxy, which is approximately 28 kpc. As this large cloud complex travels through the disk it leaves behind a debris of clouds at both sides. The debris at the trailing side creates the anomalous arm, that at the leading side creates a short-lived arm fragment that still is visible at the front edge of the gap near the edge of the galaxy.

-- Beyond approximately 6 kpc the gas in the anomalous arm still shows considerable outward motion. The available observations are not sufficiently detailed and do not go sufficiently far out to make a comparison.

The conclusion that the anomalous arms can be explained in most details, both morphological and kinematical as far as observations are available, by the expulsion hypothesis seems justified. It will be evident from the above discussion that the parameters selected for this model represent a less energetic explosion than must actually have taken place: only one arm was created, only the HI constituent in the disk was taken into account, more matter should have been ejected to shape the inner part of the arm and matter at a much higher velocity to form the outer part.

It is interesting that the seemingly normal rotation observed by Van der Kruit ends in a rather steep velocity gradient near the minor axis of the galaxy. The region where this velocity gradient is observed coincides exactly with the HII regions marked "X" and "Y" in Fig.3. I suggest that in these regions the infalling gas in the anomalous arms collides with the more slowly rotating gas in the disk. This would mean that these HII regions should be excited predominantly by shocks, although they may also contain young stars. Thus these

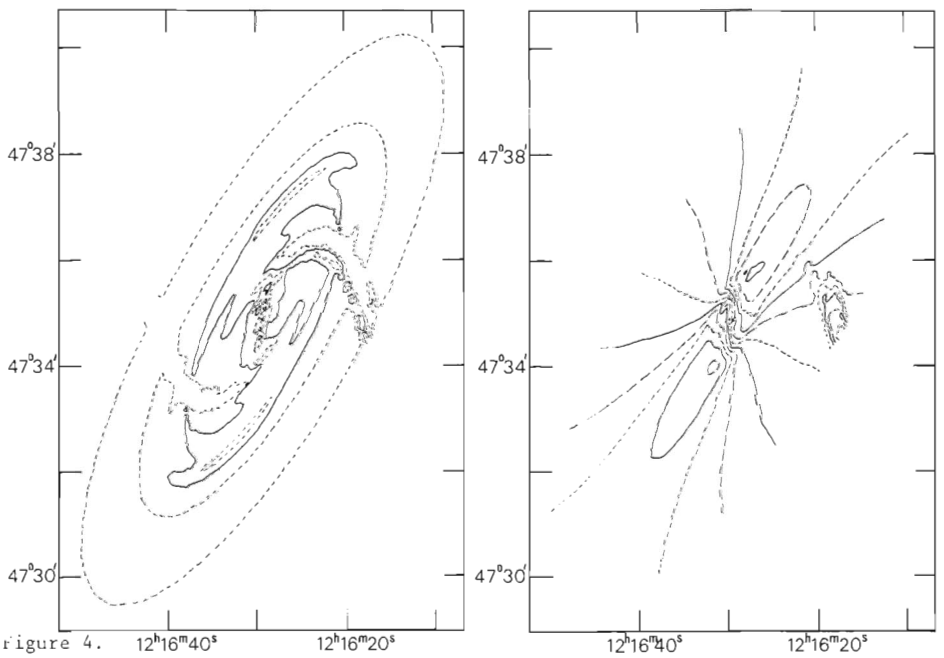

Figure 4.

Surface density of matter in the disk with simulated anomalous arm. Note that the plotted surface density is not directly related to the brightness in any one wave-length region. Contours have been drawn at (1, 2, 4, 6)·2.2 10^{24} H atom m^{-2} (face-on).

Figure 5.

Mean line-of-sight velocity of the matter in disk and anomalous arm. Contours have been drawn at 50 km s^{-1} intervals.

two HII regions in the central region may be expected to show a high excitation. If this is in fact observed, it may also be rewarding to look for soft X-rays.

5. Polarization

Fig.6 shows the full resolution map of the electric vector of the polarized component of the 1412 MHz radiation. Significant polarization is visible at the very ends of both anomalous arms; the percentage polarization in the Eastern anomalous arm may be as high as 50%. De Bruyn (1976) found approximately 25% polarization in p.a. 85^{o} at the tip of the Eastern anomalous arm at 610 MHz. The high percentage polarization observed at both frequencies implies that no significant depolarization can have occurred and that the magnetic field in that region must be quite regular on scales at least comparable to the 610 MHz beam size (56" × 76" or about 5.5 kpc × 2.5 kpc in the plane of NGC 4258).

Though it is clear that the intrinsic rotation measure in the region must be quite small (not more than π radians at 50 cm or about 10 rad m^{-2}), it is not possible to determine it exactly because the contribution from the Galaxy is not known with sufficient accuracy. From this upper limit for the intrinsic rotation measure and the observed HI surface density near the anomalous arm we can derive an approximate upper limit for $H_{\parallel}$, the component of the magnetic field parallel to the line of sight:

The surface density of thermal electrons in the anomalous arm region must be of the same order of magnitude as the mean HI surface density in the nearby unperturbed disk, which is in the order of $5\ 10^{24}$ H-atoms m^{-2}, since these electrons must originate mainly from the ionization of this hydrogen. Thus we find an upper limit for $H_{\parallel}$ of approximately 10^{-11}T(=10^{-7}G), which is a fairly low interstellar value in our neighbourhood in the Galaxy.

The strong decrease of the polarization with increasing intensity does not necessarily mean that that magnetic field becomes less regular in the brighter regions; it can very well be due to an increase of the magnetic field strength and the electron density, resulting in a strong Faraday depolarization.

6. The spectral index map and the radiation mechanism

A spectral index map has been constructed using the 610 MHz observations of De Bruyn and the 1412 MHz observations discussed in this chapter. Using the

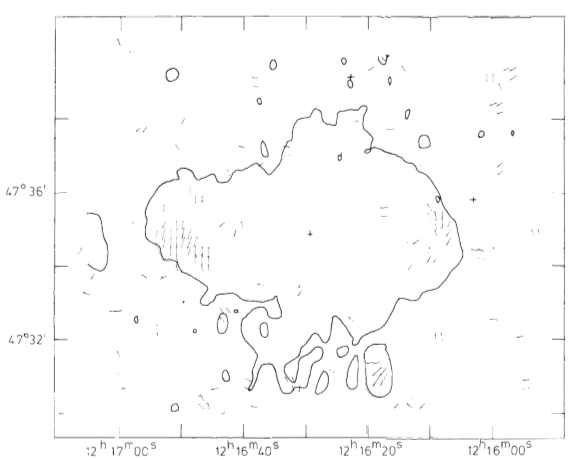

Figure 6.

clean and restore technique a 26" × 36" resolution version of both maps was constructed. The reason for making maps with such a small beam was two-fold. The primary reason was that the outward shift of all sources caused by the primary beam corrections that had to be applied to match the maps is minimized in this way. Secondly, by convolving the maps step by step an attempt could be made to obtain a spectral index map with a somewhat higher resolution than that published by De Bruyn. Though this indeed proved to be possible the resultant map differed very little from the one in Fig.7 which has a 56" × 76" FWHP beam like that of De Bruyn. The advantage of the larger beam is that the signal to noise ratio for the lower intensity levels is better.

The spectral index distribution is not essentially different from that published by De Bruyn. The HII regions in the normal arms show quite clearly, though their positions have been shifted a bit due to beam effects. The spectrum in the Western plateau steepens to the South; in the Eastern plateau very little real structure seems to be present. The large gradient observed in the source off the end of the Eastern plateau ("Q" in Fig.1) seems to indicate that the calibration of at least one of the two observations is not quite good enough. This implies that the spectral index near steep gradients in the intensity may be less reliable than would be inferred from the noise in the 610 and 1412 MHz maps individually.

The spectral index and the observed polarization indicate that the radio emission of the anomalous arms is due to synchroton radiation. If we compare the average brightness temperature at 1412 MHz in the anomalous arms, which is in the order of 5 K with peaks of at least 25 K, with that in the base disk, for which a brightness temperature of the order of 0.15 K was inferred in chapter 3, we see that the anomalous arms are between 35 and 100 times brighter. De Bruyn (1976, p.56) states that this can in principle be explained as the result of turbulent motions caused by the interaction of the ejected and the disk matter amplifying the magnetic field. The high observed relative polarization in the tips of the anomalous arms, however, seems to exclude turbulent amplification of the magnetic field, at least for that region.

Though the high degree of polarization indicates that the magnetic field is very regular, it does not necessarily indicate that it is uni-directional. One can very well imagine mechanisms whereby the magnetic field is arranged in narrow flux tubes with alternating field directions by the passage of the ejecta. This magnetic field could either be that of the disk, after a certain compression

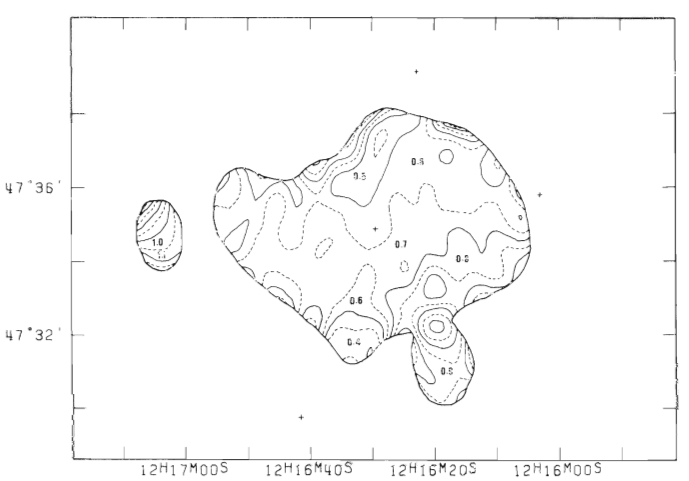

Figure 7.

as it passed the shock into the anomalous arms, or a magnetic field transported by the ejected matter. Reconnection of the field lines in situations as described above is a mechanism that is often suggested to explain particle acceleration.

Both mechanisms described above ascribe the high synchroton emission level to the effects of the passage at a high velocity through the disk medium of clouds that need not contain a magnetic field or relativistic electrons. It is also possible, however, that the relativistic particles that emit the observed radiation originated in the nucleus and have been transported to their present positions as a constituent of the ejecta. If this latter mechanism has provided the relativistic electrons, ageing effects should be observable in the spectrum at high frequencies. The high spectral index in the Western plateau between 21 and 50 cm cannot be due to such ageing, since the plateau certainly cannot be sufficiently much older than the arms for ageing effects to show up in that frequency range. It seems possible to explain this steepening by assuming that the electrons from the base disk, which have a very steep spectrum according to De Bruyn (1976, 1977), contribute approximately 30% of the observed emission from the back edge of the plateau at 50 cm. Judging from De Bruyn's 50 cm map this seems well possible.

As we have seen from the polarization data the magnetic field, at least in the tip of the anomalous arms, seems to be quite small so that it probably is not necessary to assume that more than the normal post-shock enhancement of the magnetic field has occurred there.

References.

Breugel, W.J.M. van; Miley, G.K.: 1977, *Nature 265*, 315

Bruyn, A.G. de: 1976, Ph.D. dissertation, Leiden University

Bruyn, A.G. de: 1977, *Astron. Astrophys. 58*, 221

Courtès, G; Viton, M; Véron, P.: 1965, *Quasi Stellar Sources and Gravitational Collapse*, ed. Robinson et al., University of Chicago Press, Chicago, p. 307

Deharveng, J.M.; Pellet, A.: 1970, *Astron. Astrophys. 9*, 181

Harten, R.H.: 1974, *Synthesis Radio Telescope Project, ITR no.121* (revised 1975)

Högbom, J.A.: 1974, *Astron. Astrophys. Suppl. 15*, 417

CHAPTER 5 ANALYSIS OF VELOCITY DATA IN A SPIRAL GALAXY

Summary

In this chapter I will discuss certain aspects of the analysis of velocity data, in particular HI data, of spiral galaxies. Many of the methods discussed in this chapter are not new--sometimes similar methods have been described elsewhere, as e.g. by Bosma (1978, chapter 3, section 3; chapter 6 and references therein), sometimes the methods are widely used, but have not been described so that they have to be rediscovered by each new student of the field--, other methods are slight modifications of older ones. This chapter is included for easy reference for the readers of this thesis and, hopefully, as an aid to others setting out on similar investigations. The methods described here have not always been used in the work presented in previous chapters.

1. Analysis of the line profiles

The two most important quantities that can be derived from a line profile are the total amount of HI present and the velocity of that HI. The derivation of each of these quantities will be discussed separately. First, however, I will describe a method of reducing the noise that is useful for both: the use of masks of zeros and ones by which the maps are multiplied.

The HI emission in each single-velocity map and in each line profile usually will be localized; the noise contribution will be distributed more or less uniformly. This means that if a quantity is derived from a line profile, without further restriction, a large contribution to the noise comes from a part of the profile that contains no signal. If, for each profile, we locate the points that may contain signal and delete the rest, the noise in the line profile as a whole will be reduced without loss of information. It is necessary to realize when using this procedure that low level emission that is extended in velocity or spatially may not show up above the noise in the full resolution maps and line profiles, but may nevertheless be significant. In order to detect such emission and to include it in the selected regions, it is necessary not only to study the full resolution data, but also data that have been convolved spatially and/or in velocity when determining the masks to be used.

The masking method is not only useful for reducing the noise, it can sometimes be used in place of the clean and restore technique to remove grating responses or the effects of missing short base-lines. Removal of grating responses can only be accomplished with the masking method if grating responses and signal do not coincide in a single-velocity map, but the method can nevertheless be very useful if signal is found at the position of the grating responses in other single-velocity maps. It must be realized that, e.g. for the WSRT, the grating response often is more than just a well-defined narrow ring; it may cause significant variations in the zero-level over a much larger area of the map. If signal and grating responses coincide the clean technique (Harten, 1974; Högbom, 1974; Schwartz, 1978) should be used, or extra observations obtained.

Short spacing information can be derived with the masking method in the following way: from the signal inside the masked area calculate the response expected for the missing base-line(s), then correct the unmasked map and re-determine the masks. If significantly more signal is now found inside the new masks, the process should be repeated. The method is especially useful if the zero-spacing

is sought: if in constructing the first generation masks allowance is made for the zero-level offset in the map, iteration is generally not necessary. Examples of the use of this method can be found in Van Albada and Shane (1975) and Rots and Shane (1975).

In practice the masks can be determined in different ways, from manually selecting the desired parts of the maps or profiles to highly automated methods. Manual methods have the advantage that spurious features can readily be recognized and rejected, but the definition of the masks will be less precise than for automated methods. A combination often will give the best results. Bosma (1978, p.13 ff.) discusses some methods for determining masks for each profile separately. These methods are useful if the zero-level in the profile still has to be corrected for instrumental effects and the continuum distribution, but when they are used only for data with full spatial resolution low level emission can readily be missed. Here, as in all other cases, convolved data should be used beside the full resolution data in determining the masks, even though the masks may be used only for the full resolution data.

1.1 The integrated HI map

For the derivation of the integrated HI map the use of masks is very desirable. Except for the determination of the masks the construction of a good integrated HI map is straightforward. There is, however, a method of further reducing the effects of the noise. This method is based on the assumption that the a-priori probability that a certain measured signal corresponds to a certain true signal is the same for all points in the sample. This should essentially be true for the region defined by carefully chosen masks. If the assumption does not hold, it will be found that the low-level signal is lost or evenly spread out over all points. In the method as described below use is further made of the assumption that the real signal should be positive, but this assumption is not essential.

If we have a collection of independent, infinitely accurate measurements of the amount of HI at each point on an (α,δ,V) grid, obtained with a finite, positive definite beam, the probability of the true antenna temperature at a certain point having a value between T_s and $T_s + dT_s$ is given by $P_s(T_s)dT_s$, where P_s has the following properties (assuming that no absorption occurs):

$$P_s(T_s) = 0 \quad ; \quad T_s < 0 \tag{1a}$$

$$P_s(T_s)dT_s = \lambda \quad ; \quad T_s = 0, \quad 0 < \lambda < 1 \tag{1b}$$

$$P_s(T_s) = \mu(T_s) \quad ; \quad T_s > 0, \quad 0 < \mu < 1, \int_0^\infty \mu dT_s = 1-\lambda \tag{1c}$$

In practice each observation also contains a noise contribution T_n, the distribution of which is given by $P_n(T_n)$. P_n generally is assumed to be Gaussian. We can now calculate the probability of measuring a certain $T_o = T_s + T_n$:

$$P_o(T_o) = \int_{-\infty}^{+\infty} P_s(T_o - T_n)\cdot P_n(T_n)\, dT_n = \{P_s * P_n\}(T_o) \tag{2}$$

P_o can be determined from the observed intensities in the regions defined by the masks; P_n can be determined from the remainder of the points, but regions with grating responses must not be used. P_s can be determined in a number of ways from P_o and P_n. Probably one of the best ways to accomplish this deconvolution is to assume an appropriate functional form for $\sqrt{\mu(T_s)}$, such as a combination of two or more exponential functions, and subsequently to make a least-squares solution for the free parameters in this functional form and for $\sqrt{\lambda}$. In this way positivity is automatically enforced. Once P_s is known we can calculate $P(T_s|T_o)$, which is the probability of T_s, given the fact that T_o was measured:

$$P(T_s|T_o) = P_s(T_s)\cdot P_n(T_o - T_s) \,/\, P_o(T_o) \tag{3}$$

We can now calculate the mean value of T_s for all points where we measured T_o:

$$\overline{T}_s(T_o) = \int_0^\infty T_s \cdot P(T_s|T_o)\, dT_s \qquad (4)$$

If we replace T_o by $\overline{T}_s(T_o)$ the noise is not independent of the intensity anymore, but we can easily see that the following quantity, which can be considered to be a measure of the noise is minimized:

$$\sigma^2(T|T_o) \equiv \int_0^\infty (T - T_s)^2 \cdot P(T_s|T_o)\, dT_s \qquad (5)$$

if we substitute $\overline{T}_s(T_o)$ for T.

1.2 Determination of the velocity of the HI

It is always possible to define a velocity for the HI observed in a line profile, e.g. by determining the intensity weighted mean velocity. In the following I will discuss three methods of finding a velocity. Each may lead to a different velocity, even for noise-free profiles. One cannot say, however, that in general one method is essentially better or physically more meaningful than another. For simple symmetric profiles all three methods lead to the same result.

i. The use of the intensity weighted mean velocity has some obvious advantages. The most important of these is that, once the appropriate masks have been determined, it always leads to a unique velocity. Another great advantage is that, in case the optical depths are small, the derived velocity is the mean velocity of the hydrogen. However, the method is very sensitive to noise in channels that lie far away from the mean velocity and also to variations in the zero-level of the profile. Therefore it is essential when using this method to exercise great care in selecting the points on each profile that are to be used. (See Bosma, 1978, p.13 ff.) The sensitivity to the zero-level can be diminished by iteratively selecting a mask for each profile that is symmetric with respect to the calculated mean velocity, even if this means that more noise points are included. Like all other methods the use of the intensity weighted mean velocity works well for simple profiles but gives results that are difficult to interpret for double peaked profiles and other complex profiles. It can give a velocity that lies in the empty region between the peaks of a double peaked profile, a property that may or may not be considered desirable.

ii. The velocity of the peak intensity. This method is very simple and as in the case of the intensity weighted mean velocity, the relation between the derived velocity and the observed profile is clear and well defined. The method is very different from the previous one in that it is not at all sensitive to zero-level offsets or to noise in any of the channels except for the two or three with the highest signal. For very broad profiles the method deteriorates. Masks defined in the map plane can help to reduce the number of spurious determinations. The disadvantages are that only discrete velocities can be obtained and that most of the profile is neglected.

iii. Profile fitting combines some of the advantages of both previously mentioned methods. Like method (ii) it is not sensitive to zero-level offsets and noise in other parts of the profile; like method (i) it uses more than just the few highest points. A model profile is fitted, described by a number of free parameters; each of the parameters is maximally sensitive to the measured brightnesses in a certain part of the profile. The velocity parameter generally is most sensitive in the flanks of the model profile. A major disadvantage of the method is the need for a predetermined model profile. In practice the method also has the disadvantage that for big galaxies it is quite expensive in computer time; this means that the number of spurious determinations must be limited to an absolute minimum in this case. Therefore masks should be used, but if the zero-level is not accurately known, all points in a profile for which the velocity is to be determined must be included. It is also necessary to choose the starting values for each solution with care, both to limit the number of iterations necessary per profile and to obtain a consistent solution for neighbouring profiles in certain difficult cases such as double peaked profiles.

For the velocities as presented in this thesis the last method was chosen because it was found to give the most consistent velocities for the largest number of profiles. The following model profile was used:

$$I(V) = I_o + I_p / \{ 1 + (V - V_o)^2 / D^2 \}^2 \qquad (6)$$

For the starting value for V_o the velocity of the peak in the profile after a convolution in velocity was chosen. Masked maps were used. Since the zero-level in the profiles had been determined with greater precision than would have been possible with the profile fitting procedure the zeros in the places of the rejected points in each profile were retained. (The reduction of the HI data has been described in chapter 2.) The noise in the profiles was not uniform anymore, however, so that the errors that were calculated for each of the parameters became meaningless.

2. The construction of a model of circular rotation

In this section I shall describe how a model of circular rotation can be constructed for a spiral galaxy and discuss some of the problems that may arise. The following symbols will be used:

i - the inclination of the plane of the galaxy relative to the plane of the sky. $i>0$ for counter-clockwise rotation; $-90^o<i<90^o$.

ψ - the position angle of the ascending or receding node, i.e. the position angle of the half-line on which the highest positive velocity would be measured if the galaxy were in pure circular rotation.

V - a heliocentric radial velocity.

Θ - a tangential velocity in the plane of the galaxy relative to the nucleus of the galaxy. $\Theta>0$ for counter-clockwise rotation.

Π - a radial velocity in the plane of the galaxy.

ϑ - a counter-clockwise angle in the plane of the galaxy relative to the direction of the ascending node.

r - the distance from the nucleus in the plane of the galaxy.

(x,y) a right-handed rectangular coordinate system in the plane of the sky with the origin at the nucleus. The positive x-axis coincides with the half-line of the ascending node. If a distance is available x,y and r can be converted to linear distances.

In this chapter generally no distinction will be made between the dynamical center of the galaxy and the optical nucleus; both will be called the nucleus. Although the two need not necessarily coincide, it is often found that the optical nucleus, the position of which can usually be determined very accurately, and the dynamical nucleus, the position of which generally is difficult to determine, coincide to within the error.

Certain relations exist between the quantities defined above:

$$V(r,\vartheta) = \sin(i)\cdot\{\cos(\vartheta)\cdot\Theta(r,\vartheta) + \sin(\vartheta)\cdot\Pi(r,\vartheta)\} + V_{sys} \qquad (7)$$

$$x = r\cdot\cos(\vartheta)\ ; \qquad y = r\cdot\sin(\vartheta)\cdot\cos(i) \qquad (8)$$

2.1 The desired model

The aim of this section is to describe the derivation of a model representing the galaxy as a differentially rotating disk. This means that $\Pi(r,\vartheta)$ is assumed to be zero, and $\Theta(r,\vartheta) = \Theta(r)$. The model is characterized by the values i_m, ψ_m and $V_{sys,m}$ for i, ψ and V_{sys}, the position of the nucleus and by the rotation curve $\Theta_m(r)$.

A galaxy never shows pure circular rotation; the deviations from circular rotation can usually be described in part by a perturbation theory such as that formulated by Lin et al. (1969), or the theory described in section 3 of this chapter. The desired model of circular rotation is one that can be used in combination with such a perturbation theory in order to represent the observed velocities with maximal

accuracy. It will be demonstrated in the following sub-sections that the perturbations, especially those due to the density-wave streaming that is associated with the spiral structure, can influence the derived parameters and that this influence can be reduced by an appropriate assignment of the weights to the observed velocities. The extra $\sin^2(\vartheta)$ factor introduced in the weights for the determination of rotation curve no.2 in chapter 3 is an example of an attempt to reduce this influence. We will see in section 2.6 how a knowledge of errors and perturbations can be applied in order to determine the best choice of weights for the determination of the rotation curve. In sections 2.2 to 2.5 I will discuss the derivation of the other parameters and the effect on the observed velocity field--and hence on the derived parameter values--of certain perturbations.

2.2 The effect of errors in the assumed parameters for the model

If the observed galaxy shows only pure circular rotation, but we have determined the parameters for our model incorrectly so that the true inclination of the galaxy $i = i_m - \Delta i$, the true position angle $\psi = \psi_m - \Delta\psi$, the dynamical center lies at $(-\Delta x, -\Delta y)$ instead of at (0, 0) and the true rotational velocity is $\Theta_c(r) = \Theta_m(r) - \Delta\Theta_c(r)$ we will find the following, to first order, for $\Delta V(r,\vartheta) = V_m(r,\vartheta) - V_{obs}(r,\vartheta)$:

$$\begin{aligned}\Delta V(r,\vartheta) = {} & \Delta\psi \cdot \sin(i) \cdot \sin(\vartheta) \cdot \left[\cos^2(\vartheta) \cdot tg^2(i) \cdot \left[\Theta_c(r) - r\,\frac{d\Theta_c(r)}{dr}\right] + \Theta_c(r)\right] \\ & - \Delta i \cdot \cos(\vartheta) \cdot \left[tg(i) \cdot \sin(i) \cdot \sin^2(\vartheta) \cdot \left\{\Theta_c(r) - r\,\frac{d\Theta_c(r)}{dr}\right\} - \cos(i) \cdot \Theta_c(r)\right] \\ & + \frac{\Delta x}{r} \cdot \sin(i) \cdot \left[\cos^2(\vartheta) \cdot \left\{\Theta_c(r) - r\,\frac{d\Theta_c(r)}{dr}\right\} - \Theta_c(r)\right] \\ & + \frac{\Delta y}{r} \cdot tg(i) \cdot \sin(\vartheta) \cdot \cos(\vartheta) \cdot \left\{\Theta_c(r) - r\,\frac{d\Theta_c(r)}{dr}\right\} \\ & + \Delta\Theta_c(r) \cdot \sin(i) \cdot \cos(\vartheta) \quad + \quad \Delta V_{sys} \end{aligned} \tag{9}$$

A graphical representation of some of these terms is given in Fig.1. It is evident that in the case of solid-body rotation only the position angle, a combination of

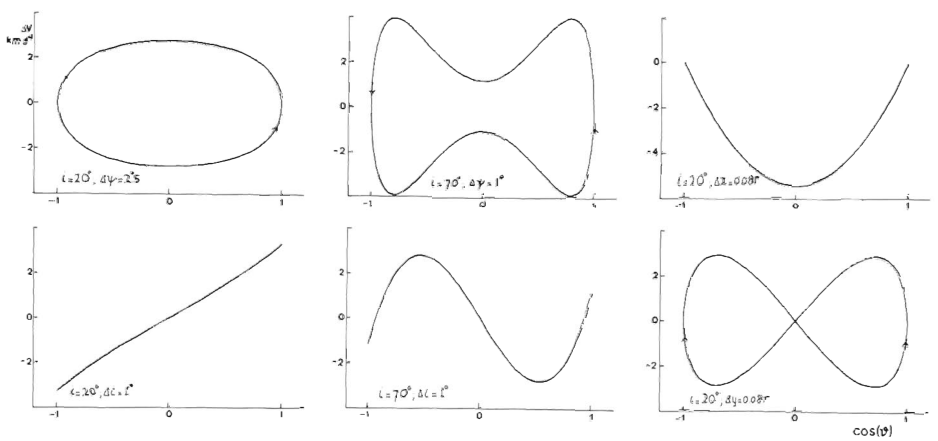

Figure 1.

The velocity deviations associated with different errors in the projection parameters for a flat rotation curve Θ_c = 200 km s^{-1} plotted against cos(ϑ). The values for the inclination and the specific error are given in the figure.

Δi and $\Delta\Theta_c$ and a combination of Δx and ΔV_{sys} can be determined; for a flat rotation curve all parameters can be determined. If the galaxy shows deviations from circular rotation difficulties may arise in the derivation of the different parameters.

2.3 The effect of circularly symmetric radial streaming

Circularly symmetric radial streaming introduces a term $\Pi(r)\sin(i)\sin(\vartheta)$ in the observed velocities which, especially for small inclinations, may be difficult to distinguish from an error in the position angle.

2.4 Warps

The existence of a warp implies that the disk of the galaxy under consideration is not flat so that the derived projection parameters apply only to a part of the galaxy. It also implies that the galaxy will show systematic motions in the direction perpendicular to its mean plane, the z-direction.

Following Rogstad et al. (1974) one can try to derive separate projection parameters for different parts of the disk. The model Rogstad et al. use consists of a set of rings of different radii for each of which a model of circular rotation is determined. Such rings will necessarily precess, but the z-motions that are associated with this precession are disregarded. Especially for galaxies that are nearly face-on this procedure is clearly unsatisfactory. It can easily be seen that the z-velocities associated with the precession will, especially for small inclinations, lead to errors primarily in the position angle of a ring and in the rotational velocities. Using an appropriate model for the precession of the rings it must generally be possible to iterate to a more accurate tilted-ring model. According to Dr. E. Dekker (private communication) it will also be necessary to take into account that, due to the variations in the radial and tangential forces associated with an inclined orbit, deviations from circular rotation should occur in the ring.

For the dynamics of the abrupt bend that seems to occur in the disk of NGC 4258 no theory is yet available.

2.5 Velocity deviations associated with a density wave

With any density wave, be it self-consistent or driven by an external mechanism, deviations from pure circular rotation will be associated. In the linear approximation the velocities in the plane of the galaxy, associated with a density wave with multiplicity m (an m-armed density wave) can be described by:

$$\Theta(r,\vartheta) = \Theta_c(r) + \cos(m\vartheta)\cdot\Delta_1\Theta(r) + \sin(m\vartheta)\cdot\Delta_2\Theta(r) \qquad (10)$$

$$\Pi(r,\vartheta) = \cos(m\vartheta)\cdot\Delta_1\Pi(r) + \sin(m\vartheta)\cdot\Delta_2\Pi(r) \qquad (11)$$

For a tightly wound pattern the following approximate relation holds:

$$\Delta_1\Theta(r)\cdot\Delta_1\Pi(r) + \Delta_2\Theta(r)\cdot\Delta_2\Pi(r) \simeq 0 \qquad (12)$$

Well inside corotation $\Delta_1\Theta$ and $\Delta_2\Pi$ will approximately be of the same magnitude and have the same sign; close to corotation $\Delta_1\Theta$ will dominate and outside corotation the signs will be opposite. If the surface density $\sigma(r,\vartheta)$ for a tightly wound pattern can be described by:

$$\Delta\sigma(r,\vartheta) = \Delta_0\sigma(r)\cdot\cos\left[m\left[\vartheta+\vartheta_0(r)\right]\right] \qquad (13)$$

we furthermore have the following approximate relation:

$$\cos\left[m\cdot\vartheta_0(r)\right]\cdot\Delta_1\Theta(r) - \sin\left[m\cdot\vartheta_0(r)\right]\cdot\Delta_2\Theta(r) \simeq 0 \qquad (14)$$

If we have a one-armed spiral structure (m=1) we find the following deviations in the velocity field:

$$\Delta V(r,\vartheta) = \sin(i)\cdot\left[\Delta_1\Theta(r)\cdot\cos^2(\vartheta) + \left[\Delta_2\Theta(r)+\Delta_1\Pi(r)\right]\cdot\sin(\vartheta)\cdot\cos(\vartheta) + \Delta_2\Pi(r)\cdot\sin^2(\vartheta)\right] \qquad (15)$$

which we may also write as:

$$\Delta V(r,\vartheta) = \Delta_1 V(r) + \cos(2\vartheta)\cdot\Delta_2 V(r) + \sin(2\vartheta)\cdot\Delta_3 V(r) \qquad (16)$$

If evaluated at a single r these disturbances are indistinguishable from an offset in the position of the nucleus combined with an error in the systemic velocity.

For a two-armed spiral we find:

$$\Delta V(r,\vartheta) = \sin(i)\cdot\left[\Delta_1\Theta(r)\cdot\cos(2\vartheta)\cdot\cos(\vartheta) + \Delta_2\Theta(r)\cdot\sin(2\vartheta)\cdot\cos(\vartheta) + \Delta_1\Pi(r)\cdot\cos(2\vartheta)\cdot\sin(\vartheta) + \Delta_2\Pi(r)\cdot\sin(2\vartheta)\cdot\sin(\vartheta)\right] = \Delta_1 V(r)\cdot\cos(\vartheta) + \Delta_2 V(r)\cdot\sin(\vartheta) + \Delta_3 V(r)\cdot\cos(3\vartheta) + \Delta_4 V(r)\sin(3\vartheta) \qquad (17)$$

Δ_1V and Δ_2V will be dominant inside corotation; Δ_3V and Δ_4V outside. If evaluated at a single radius Δ_1V and Δ_3V together will appear as a combination of errors in the inclination and the rotation curve; Δ_2V and Δ_4V as a combination of expansion or contraction and an error in the position angle. If averaged over a sufficiently large range in r the effects on the derived projection parameters may average out. For the rotation curve, which is a function of radius, the problem is more severe since each arm occupies a considerable range in the radius of the disk.

Beside the kinematical effects of density wave streaming that were discussed above, systematic variations in the fraction of the gas observable as HI can occur along a stream-line. Such variations can lead to errors in the measured gas-density and hence to systematic effects in the derived velocities.

Fig.2 depicts the characteristic patterns for the residual velocities expected for two-armed density waves, both leading and trailing and inside and outside corotation. These pictures illustrate the following general rule:
The pattern in the residual velocity field has the same sense of winding as the pattern in the density, but its multiplicity is one lower than that of the density-pattern inside corotation, and one higher outside corotation.
The most accurate method of determining whether the velocity residuals at any one position should be counted as positive or negative is by comparing them to the residuals at neighbouring positions.

2.6 The rotation curve and its errors

If we have determined the projection parameters and the systemic velocity as accurately as possible we can determine the rotation curve. Each measured velocity can be converted to a rotational velocity, the corresponding radius can be calculated and the errors in the calculated rotational velocities can be evaluated.

The calculation of the errors can serve two purposes, namely to evaluate the errors in the final result and to determine the best way to combine the available data, i.e. to determine the weights.

In the following I will analyze only some of the errors that may influence the derived rotation curve; how the knowledge of the errors can be used to determine optimal weights will be discussed in section 2.7. I will assume that the rotation curve is calculated as follows:

$$\Theta_m(r) = \sin^{-1}(i)\sum_{\vartheta}\left[V_{obs}(r,\vartheta) - V_{sys}\right]\cdot\cos^{-1}(\vartheta)\cdot G(r,\vartheta) \qquad \text{with} \qquad (18)$$

$$\sum_{\vartheta} G(r,\vartheta) = 1 \qquad (19)$$

The summation is assumed to be over independent points, i.e. over points separated by a beam-size and not by a grid-interval. I will distinguish two types of errors,

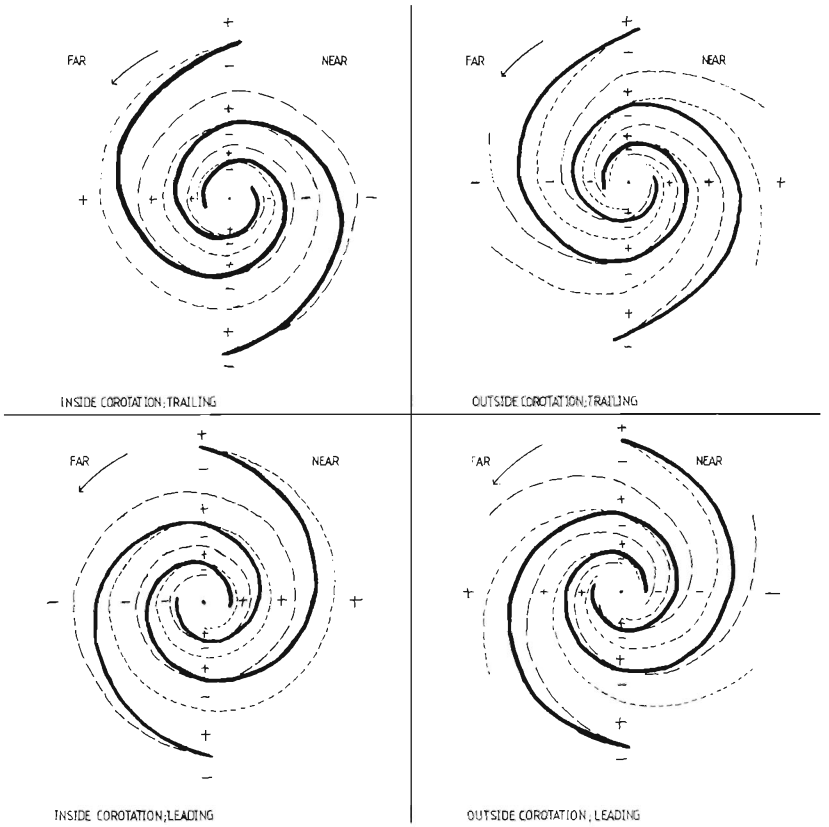

Figure 2.

Characteristic patterns in the residual velocity field for tightly wound two-armed spirals. The heavy lines represent the spiral arms, the dashed lines are the lines of zero residual velocity. The signs of $(V_{obs} - V_m)$ are indicated.

namely in quantities that differ from point to point, like those in the measured velocities, and errors in quantities that are the same for all points in the summation, like those in the systemic velocity and the projection parameters. Errors in slowly varying quantities can, depending on their characteristic scales, generally be treated either as errors of the first type, or as a combination of errors of the second type (as e.g. errors due to density wave streaming).
Errors of the first type are:

Ia. Errors in the measurement of the velocity. For HI measurements these errors are generally quite small so that they will not dominate the error in the derived rotation curve. The contribution to the total error is described by:

$$\Delta^2 \Theta_m(r) = \sin^{-2}(i) \sum_{\vartheta} \Delta^2 V_{obs}(r,\vartheta) \cdot \cos^{-2}(\vartheta) \cdot G^2(r,\vartheta) \qquad (20)$$

Ib. Random motions in the galaxy itself. Though these cannot, strictly speaking, be called true errors their influence on the derived rotation curve can be analyzed in the same way. They often are at least as large as the measuring errors; their importance is further increased by the fact that their characteristic linear scale may be much larger than one beam-size so that fewer independent points will be included in each summation. There is no reason to suppose that the amplitude of the

random motions ΔZ in z is equal to that of those in ϑ or r so that their combined effect is described by:

$$\Delta^2\Theta_m(r) = \sum_{\vartheta} \left[\Delta_r^2\Theta(r)\cdot\cos^2(\vartheta) + \Delta_r^2\Pi(r)\cdot\sin^2(\vartheta) + \Delta_r^2 Z\cdot\cot g^2(i) \right]\cdot\cos^{-2}(\vartheta)\cdot G^2(r,\vartheta) \qquad (21)$$

To the errors of the second type belong those in the projection parameters, in the systemic velocity, and the errors caused by density wave streaming:

IIa. Errors in the projection parameters. These lead to variations in the shape of the annulus corresponding to a certain radius. The influence of this effect on the calculated rotation curve can only be evaluated if certain assumptions are made concerning the changes in the velocities measured in the annulus, caused by the change in the shape of the annulus. I will assume that the velocity field can be described with sufficient accuracy by a preliminary model of circular rotation with rotation curve $\Theta_p(r)$. I will further neglect the fact that the weights will be dependent on the projection parameters themselves, and not, as for the errors in the velocities, on the errors alone. Leaving the derivations to the critical reader we then find:

$$\begin{aligned}\Delta^2\Theta_m(r) = {} & \left(\Delta\gamma \sum_{\vartheta} tg(\vartheta)\cdot\cos^{-1}(\vartheta)\cdot\left[tg^2(i)\cdot\cos^2(\vartheta)\cdot\left\{\Theta_p(r) - r\frac{d\Theta_p(r)}{dr}\right\} + \Theta_p(r)\right]\cdot G(r,\vartheta)\right)^2 \\ & \left(\Delta i \sum_{\vartheta} \left[tg^2(i)\cdot\sin^2(\vartheta)\cdot\left\{\Theta_p(r) - r\frac{d\Theta_p(r)}{dr}\right\} - \sin^{-1}(i)\cdot\cos(i)\cdot\cos^{-1}(\vartheta)\cdot\left[V_{obs}(r,\vartheta) - V_{sys}\right]\right]\cdot G(r,\vartheta)\right)^2 \\ & \left(\frac{\Delta x}{r}\sum_{\vartheta}\left[\cos(\vartheta)\cdot\left\{\Theta_p(r) - r\frac{d\Theta_p(r)}{dr}\right\} - \cos^{-1}(\vartheta)\cdot\Theta_p\right]\cdot G(r,\vartheta)\right)^2 \\ & \left(\frac{\Delta y}{r}\sum_{\vartheta}\cos^{-1}(i)\cdot\sin(\vartheta)\cdot\left\{\Theta_p(r) - r\frac{d\Theta_p(r)}{dr}\right\}\cdot G(r,\vartheta)\right)^2 \end{aligned} \qquad (22)$$

The errors in x and y described here are those due to an erroneous choice of the position of the nucleus. Similar errors are caused by the positional inaccuracies due to the finite size of the observing beam, but those are errors of the first type and must be treated as such (first squaring and subsequently adding).

IIb. An error in the systemic velocity. For this error we find:

$$\Delta^2\Theta_m(r) = \left(\Delta V_{sys}\sum_{\vartheta}\cos^{-1}(\vartheta)\cdot\sin^{-1}(i)\cdot G(r,\vartheta)\right)^2 \qquad (23)$$

IIc. Errors caused by density wave streaming. These will often be the dominant cause of errors in the rotation curve. In this case, however, we can to a certain degree predict what the velocity deviations will be. Sometimes it is even possible to construct a model that will reproduce the effects of the density wave streaming, e.g. as was done by Visser (1978) for M 81. Most galaxies are not as regular as M 81 so that such model fitting cannot be done in general. The description that should be used for the effects of a density wave depends critically on how much we know about the wave pattern. If the pattern is irregular and multiple-armed the associated velocities can best be described as random motions; if it is regular, tightly wound and two-armed with known phase $\vartheta_0(r)$ we can use the description (see section 2.5):

$$\begin{aligned}\Delta^2\Theta_m(r) = {} & \left(\Delta_v\Theta(r)\cdot\sum_{\vartheta}\sin\left(2\left\{\vartheta + \vartheta_0(r)\right\}\right)\cdot G(r,\vartheta)\right)^2 \\ & + \left(\Delta_v\Pi(r)\sum_{\vartheta}\cos\left(2\left\{\vartheta + \vartheta_0(r)\right\}\right)\cdot\sin(\vartheta)\cdot\cos^{-1}(\vartheta)\cdot G(r,\vartheta)\right)^2 \end{aligned} \qquad (24)$$

where

$$\Delta_v\Theta(r) = \sin\left(2\vartheta_0(r)\right)\cdot\Delta_1\Theta(r) + \cos\left(2\vartheta_0(r)\right)\cdot\Delta_2\Theta(r) \qquad (25a)$$

$$\Delta_v\Pi(r) = \cos\left(2\vartheta_0(r)\right)\cdot\Delta_1\Pi(r) - \sin\left(2\vartheta_0(r)\right)\cdot\Delta_2\Pi(r) \qquad (25b)$$

The total error in Θ_m can be calculated in the usual way. In order to minimize this error the appropriate weights should be used. I will use a slightly more general notation in discussing how the weights can be calculated: Assume that we want to calculate the weighted mean of a quantity F_j calculated in J different points. F_j is a function of N quantities $x_{n,j}$ measured in each of

the J points, each having an error $\Delta x_{n,j}$ and M quantities y_m that are the same for all J points, but that do have an error Δy_m. We thus have:

$$\bar{F} = \sum_j F(x_{1,j},\ldots,x_{N,j}, y_1,\ldots,y_M)\cdot G_j \qquad (26)$$

$$\sum_j G_j = 1 \qquad (27)$$

Writing $f_{n,j}$ for $\partial F_j/\partial x_{n,j}$ and $f_{m,j}$ for $\partial F_j/\partial y_m$ we obtain for the error in $\bar{F}$:

$$\Delta^1\bar{F} = \left\{\sum_n\left[\sum_j(\Delta x_{n,j}\cdot f_{n,j}\cdot G_j)^2\right]\right\} + \left\{\sum_m\left[\Delta y_m\cdot\sum_j f_{m,j}\cdot G_j\right]^2\right\} \qquad (28)$$

Using Lagrange's method of undetermined multipliers (Courant, 1936, p.188 ff.) we find that the condition that this error be minimal, under the subsidiary condition of equation (27), leads to the following set of J linear equations:

$$G_j\cdot\left\{\sum_n \Delta^1 x_{n,j}\cdot f_{n,j}^2\right\} + \sum_m\left\{\Delta^1 y_m\cdot f_{m,j}\cdot\sum_k\left(f_{m,k}\cdot G_k\right)\right\} + \lambda = 0 \qquad (29)$$

where the G's and λ are the unknowns (equation (27) is the J+1st equation). This set of equations can in principle be solved with Gauss elimination, but it may be necessary to use some other algorithm for large J's.

The inclusion of the $\sin^2(\vartheta)$ in the weights used for rotation curve no.2 in chapter 3 was an attempt to reduce the influence of $\Delta\Theta$ on Θ_m, but it was not based on the rigorous error analysis described here.

3. A simple method for the analysis of the gas flow in a spiral galaxy

The aim of the theory to be developed in this section is to give an insight into the behaviour of the gas in the potential of a spiral galaxy. It is essentially an epicyclic analysis of the gas response to a perturbation in the axisymmetric potential of a disk galaxy, such as is often used. The inclusion of a linear dissipative term is new, however. This term allows the theory to be used in the neighbourhood of the Lindblad resonances, but it is sufficiently simple that an analytic solution remains possible.

Using this theory some models for the gas-response to a bar-like potential have been calculated, one of which was presented in chapter 3, section 6. As in the numerical gas-dynamical models presented by Huntley et al. (1978) it was observed that in order to obtain a density maximum in the gas near the minimum of the bar-potential, a high pattern speed had to be chosen relative to the maximum in $\Omega-\kappa/2$, i.e. the pattern should have no inner Lindblad resonance. Also similar to their findings is the maximum in the response that occurs near corotation. It must be stressed, however, that although the theory leads to qualitatively correct results, quantitatively correct results can only be obtained with a rigorous gas-dynamical analysis such as that of Huntley et al. The main advantage of the theory to be presented here is its general applicability combined with its mathematical simplicity. It should prove useful for the construction of simple models, for qualitative parameter studies and for the definition of initial conditions for gas-dynamical calculations.

I will use, as far as possible, the same notation as in the earlier sections of this chapter; a number of new symbols will be defined at the appropriate places in the text. Derivatives with respect to r will be indicated by a prime "'", those with respect to time by a dot "$\cdot$".

Let the undisturbed potential be $\Phi_o(r)$, the pressure $P_o(r)$ and the density in the plane of the galaxy $\rho_o(r)$. The unperturbed motion of the gas in circular orbits is then described by:

$$\left\{r\dot{\vartheta}(r)\right\}^2\cdot r = \Theta_c^2(r)\cdot r^2 \equiv \Omega_c^2(r)\cdot r \equiv \Phi_o'(r) + P_o'(r)\cdot\rho_o^{-1}(r) \qquad (30)$$

Since the contribution due to P_o generally is small and is automatically included in the potential derived from a rotation curve--because the rotation curve is

always determined from the gas constituent, either Hα or HI, in a galaxy--I will further neglect its effect on the unperturbed motion of the gas.

The perturbation of the potential will be assumed to be of the following form:

$$\Delta\Phi(r,\vartheta) = \varphi(r)\cdot\cos\left(m\cdot\left[\vartheta-\Omega_p\cdot t+\vartheta_o(r)\right]\right) \tag{31}$$

$\varphi(r)$ determines the amplitude of the perturbation; the cosine factor its shape. In this cosine factor m is the multiplicity of the pattern, Ω_p its angular velocity, and $\vartheta_o'(r)$ determines the sense of winding and the pitch angle. For $\vartheta_o'(r)=0$ a bar-potential is obtained, for $\vartheta_o'(r)>0$ that of a trailing wave. Note that the sign of the perturbing potential is positive in local density minima.

In the following I will study the behaviour of the gas around an arbitrary radius $r=r_o$. Dropping the r-dependence of a certain quantity will imply that its value at r_o should be used, e.g. $\Omega_c=\Omega_c(r_o)$. The cosine factor in equation (31) will be written as "C"; for the corresponding sine term an "S" will be used.

Let the position of a gas element in absence of a perturbation be given by $(r_o,\ \vartheta_u(t))$, and its position in presence of a perturbation by $(r(t),\vartheta(t))$. Then the solution of the equations of motion, in the linear approximation, with the inclusion of a damping term and the exclusion of secular terms is known to be of the following form:

$$\vartheta_u(t) = \vartheta_u(0)+\Omega_c\cdot t \tag{32}$$

$$\vartheta(t) = \vartheta_u(t)+\Delta\vartheta(\vartheta_u(t),t) \tag{33}$$

$$\Delta\vartheta(\vartheta_u(t),t) = \alpha\cdot C+\beta\cdot S \tag{34}$$

$$r(t) = r_o+\Delta r(\vartheta_u(t),t) \tag{35}$$

$$\Delta r(\vartheta_u(t),t) = a\cdot C+b\cdot S \tag{36}$$

The density in the plane is then given, again in the linear approximation and omitting all written time and place dependences:

$$\rho = \rho_o\cdot r_o\cdot r^{-1}\cdot\left(\frac{\partial r}{\partial r_o}\cdot\frac{\partial\vartheta}{\partial\vartheta_u}-\frac{\partial\vartheta}{\partial r_o}\cdot\frac{\partial r}{\partial\vartheta_u}\right)^{-1} =$$
$$\rho_o\cdot\left\{1-C\cdot\left(a\cdot r_o^{-1}+\vartheta_o'\cdot m\cdot b+a'+m\cdot\beta\right)-S\cdot\left(b\cdot r_o^{-1}-\vartheta_o'\cdot m\cdot a+b'-m\cdot\alpha\right)\right\} \tag{37}$$

The equations that determine a, b, α and β now have to be derived. In order to simplify the notation I will use $\omega = m\cdot(\Omega_c-\Omega_p)$. The motion of a gas element will be influenced by forces due to:

a) The unperturbed potential and the inertial forces for the non-Cartesian coordinate system used.
b) The potential perturbation.
c) Dissipation.
d) Pressure gradients.
e) Several other effects, such as self-gravitation, I shall neglect.

The accelerations $\ddot{r}$ and $\ddot{\vartheta}$ derived from equations (32) to (36) must be equal to those derived from the sum of the force contributions, so that:

$$-\omega^2\cdot(a\cdot C+b\cdot S) \doteq \ddot{r}(\text{forces}) \tag{38}$$

$$-\omega^2\cdot(\alpha\cdot C+\beta\cdot S) \doteq \ddot{\vartheta}(\text{forces}) \tag{39}$$

I shall now treat each force contribution separately.

a) The unperturbed potential and the inertial forces. These force contributions are generally known; I therefore give them without further comment, omitting all

time and place dependences of the variable:

$$\ddot{r}_a = -\Delta r \cdot \bar{\Phi}'' + 2\Omega_c \cdot r_o \cdot (\Delta\dot{\vartheta}) + \Omega_c^2 \cdot \Delta r \tag{40}$$

$$\ddot{\vartheta}_a = -2\Omega_c \cdot (\Delta\dot{r}) \cdot r_o^{-1} \tag{41}$$

The epicyclic frequency κ associated with this potential is given by:

$$\kappa^2 = 3\Omega_c^2 + \bar{\Phi}_o'' = 4\Omega_c^2 + 2\Omega_c \cdot \Omega_c' \cdot r_o \tag{42}$$

b) The potential perturbation. Since φ should be small we can use, to the first approximation, the accelerations at $r = r_o$ and $\vartheta = \vartheta_u$. We then find:

$$\ddot{r}_b = \vartheta_o' \cdot m \cdot \varphi \cdot S - \varphi' \cdot C \tag{43}$$

$$\ddot{\vartheta}_b = m \cdot \varphi \cdot S \cdot r_o^{-2} \tag{44}$$

If we only include the forces due to the entire potential and the inertial forces, and disregard dissipation, pressure and the rest we find the following solution for a, b, α and β:

$$a = -\frac{2m \cdot \varphi \cdot \Omega_c + \varphi' \cdot \omega \cdot r_o}{\omega \cdot r_o \cdot (\kappa^2 - \omega^2)} \tag{45}$$

$$b = \frac{\vartheta_o' \cdot m \cdot \varphi}{(\kappa^2 - \omega^2)} \tag{46}$$

$$\alpha = \frac{2\vartheta_o' \cdot m \cdot \varphi \cdot \Omega_c}{\omega \cdot r_o \cdot (\kappa^2 - \omega^2)} \tag{47}$$

$$\beta = \frac{m \cdot \varphi \cdot (\omega^2 + 4\Omega_c^2 - \kappa^2) + 2\Omega_c \cdot \varphi' \cdot \omega \cdot r_o}{\omega^2 \cdot r_o^2 \cdot (\kappa^2 - \omega^2)} \tag{48}$$

All these coefficients have singularities at the Lindblad resonances; all except b have a singularity at corotation. The apparent singularity at $r_o = 0$ can be prevented by the altogether reasonable choice of $\varphi(r) \propto r^2$ for small r. The dissipative and the pressure terms will, as can easily though not quickly be verified, suppress the other singularities.

Evidently the term $C \cdot \vartheta_o' mb$ in equation (37) will dominate the solution for the density in the tightly wound limit ($\vartheta_o' \to \infty$); in order to keep the compression finite and non-zero φ should be equal to $\varepsilon \cdot m^{-2} (\vartheta_o')^{-2} (\kappa^2 - \omega^2)$ for large values of ϑ_o', where ε is a constant much smaller than one.

If we calculate $\{\omega^2 \cdot r_o \cdot (a \cdot \alpha + b \cdot \beta)\}$, which is in fact the left-hand side of equation (12) in section 2.5 of this chapter, we find:

$$\omega^2 \cdot r_o^2 \cdot (a \cdot \alpha + b \cdot \beta) = -m \cdot \varphi^2 \cdot \vartheta_o' \cdot r_o^{-1} \cdot (\kappa^2 - \omega^2)^{-1} \tag{49}$$

which is not generally equal to zero, but which is in case of a bar-potential and in the tightly wound limit.

c) Dissipation. Although the choice of a linear dissipative term is physically unrealistic, it is certainly better than none at all, while it has the advantage that analytically simple solutions remain possible. If we require that the unperturbed solution remain unaltered we can, for instance, include the following terms in the equations of motion:

$$\ddot{r}_c = -D \cdot (\Delta\dot{r}) \tag{50}$$

$$\ddot{\vartheta}_c = -D \cdot (\Delta\dot{\vartheta}) \tag{51}$$

D^{-1} is the damping time for a perturbation. The solution of the equations for

a, b, α and β still is straightforward and numerically simple, but the analytical expression for each of the coefficients becomes fairly complicated on inclusion of the damping term.

d) Pressure gradients. The acceleration due to a pressure gradient is given by:

$$\ddot{r}_d = -\rho^{-1} \cdot \frac{\partial P}{\partial r} \tag{52}$$

$$\ddot{\vartheta}_d = -\rho^{-1} \cdot r^{-2} \cdot \frac{\partial P}{\partial \vartheta} \tag{53}$$

The pressure itself is given by:

$$P = P_o \cdot \left[\frac{\rho}{\rho_o}\right]^{\gamma} \tag{54}$$

P_o may be dependent upon r, but, since the pressure gradient in the absence of perturbations has already been included in the equations of motion for that case, P_o' should be subtracted from P' to find the effect of the perturbation in the pressure distribution. We thus have in the linear approximation:

$$\Delta P = \gamma \cdot P_o \cdot \left[\frac{\rho}{\rho_o} - 1\right] = c^2 \cdot \Delta\rho \tag{55}$$

The local density is given by equation (37). It is evident that since this equation contains derivatives of a and b with respect to r that an entirely correct incorporation of the pressure would render the solution of the equations for the wanted coefficients much more complicated. This is at odds with the aim of obtaining a simple solution. For that reason I decided to evaluate the compression and the resultant acceleration for each stream-line separately.
This leads to the following formulae:

$$\rho = \frac{\rho_o \cdot r_o}{r \cdot \frac{d\vartheta}{d\vartheta_o}} = \rho_o \cdot \left[1 - \frac{a \cdot C + b \cdot S}{r_o} - m \cdot b \cdot C + m \cdot \alpha \cdot S\right] \tag{56}$$

$$\ddot{r}_d = 0 \tag{57}$$

$$\ddot{\vartheta}_d = -\frac{c^2}{r_o^2} \cdot \left\{ \frac{a \cdot m \cdot S - b \cdot m \cdot C}{r_o} + m^2 \cdot \beta \cdot S + m^2 \cdot \alpha \cdot C \right\} \tag{58}$$

This approximation is very crude, of course; it necessitates the use of a very large value for c^2, e.g. 500 pc^2 My^{-2} as in the example in chapter 3, section 6.

References.

Albada, G.D. van; Shane, W.W.: 1975, *Astron. Astrophys. 42*, 433

Bosma, A.: 1978, Ph.D. dissertation, University of Groningen

Courant, R.: 1936, *Differential & Integral Calculus, Vol. II*, Blackie & Son, Ltd., Glasgow and London, reprinted 1964

Harten, R.H.: 1974, *Synthesis Radio Telescope Project, ITR no. 121* (revised 1975)

Högbom, J.A.: 1974, *Astron. Astrophys. Suppl. 15*, 417

Huntley, J.M.; Sanders, R.A.; Roberts, W.W. Jr.: 1978, *Astrophys. J. 221*, 521

Lin, C.C.; Yuan, C.; Shu, F.H.: 1969, *Astrophys. J. 155*, 721

Rogstad, D.H.; Lockhart, I.A.; Wright, M.C.H.: 1974, *Astrophys. J. 193*, 309

Rots, A.H.; Shane, W.W.: 1975, *Astron. Astrophys. 45*, 25

Schwarz, U.J.: 1978, *Astron. Astrophys.* *65*, 345
Visser, H.C.D.: 1978, Ph.D. dissertation, University of Groningen

CHAPTER 6 THE BEHAVIOUR OF GAS CLOUDS MOVING AT A HIGH VELOCITY THROUGH A MEDIUM

Summary

In this chapter I analyze some of the properties of a cloud of gas moving at a high velocity through a cold medium. I derive a simple model for such a cloud and subsequently examine whether such a cloud is stable and what processes will be important if it is not. Some numerical examples are presented and the consequences of this analysis for the expulsion model are discussed.

1. The cloud model

The model adopted is a very simple ram-pressure model. Fig.1 shows a sketch of such a model cloud.The coordinate system used is indicated. It is assumed that the cloud is moving with a velocity v through a cold, i.e. pressureless medium having a density ρ. The gas in the cloud is assumed to be monatomic with standard abundances and density $\rho_c(h)$. It is further assumed that the cloud has a uniform temperature corresponding to an internal energy ε per unit mass. The pressure in the cloud is then given by:

$$P_c(h) = \tfrac{2}{3}\,\rho_c(h)\cdot\varepsilon \qquad (1)$$

The cloud will experience a deceleration a due to the interaction with the medium, so that the density is that of an exponential atmosphere:

$$\rho_c(h) = \rho_c(0)\cdot\exp\left(-\frac{3a\cdot h}{2\varepsilon}\right) \qquad (2)$$

The ram-pressure exerted by the external medium is of the order of:

$$P_r(h) = \rho\cdot v^2\cdot\cos^2(\vartheta) \qquad (3)$$

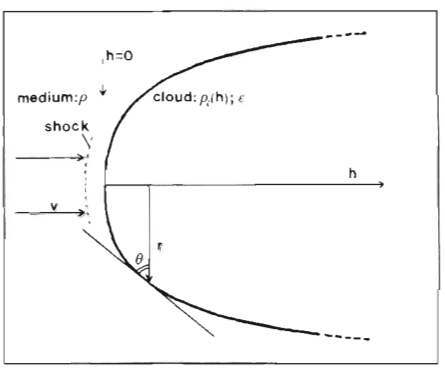

Figure 1.

Sketch of the cloud model described in section 1.

The precise value of the ram-pressure depends somewhat on what happens to the gas that has collided with the cloud. $P_i(h)$ and $P_r(h)$ must be equal, so that:

$$\rho \cdot v^2 \cdot \cos^2(\vartheta) = 2/3\ \varepsilon \cdot \rho_i(o) \cdot \exp\left(-\frac{3a \cdot h}{2\varepsilon}\right) \tag{4}$$

From $\frac{dr}{dh} = \cot g(\vartheta)$ we can now derive:

$$r(h) = \frac{4\varepsilon}{3a} \cdot \arccos\left[\exp\left(-\frac{3a \cdot h}{4\varepsilon}\right)\right] \tag{5}$$

$$r_{max} = \frac{2\pi\varepsilon}{3a} \tag{6}$$

The mass of the cloud can now be found:

$$m = \int_0^\infty \pi r^2(h) \cdot \rho_i(h)\, dh = \frac{2\pi(\pi^2 - 4)}{9a^3} \cdot \rho \cdot v^2 \cdot \varepsilon^2 \equiv K \cdot \frac{\rho \cdot v^2 \cdot \varepsilon^2}{a^3} \tag{7}$$

($K = 4.10$). We can now express the radius and the deceleration in terms of the other quantities:

$$r_{max} = \frac{2\pi}{3} \cdot \left(\frac{m \cdot \varepsilon}{K \cdot \rho \cdot v^2}\right)^{1/3} \tag{8}$$

$$a = \left(\frac{K \cdot \rho \cdot v^2 \cdot \varepsilon^2}{m}\right)^{1/3} \tag{9}$$

The knowledge of a as a function of v does not suffice to describe the time dependence of the velocity of the cloud; the time derivatives of m and ε must also be known for this purpose. To determine these a more elaborate model should be used.

2. Characteristic time scales

Though the model presented in the previous section is very crude we can deduce a number of interesting facts concerning the behaviour of a gas cloud by studying the time scales on which changes would occur in the model cloud. In the following a number of such time scales are discussed.[1]

a) The stopping time τ_{stop}. This is the time needed for the cloud to lose a significant fraction of its original velocity. The maximum distance d_{max} that a cloud can travel is closely related to this stopping time.

$$\tau_{stop} \equiv \frac{v}{a} = \left(\frac{m \cdot v}{K \cdot \rho \cdot \varepsilon^2}\right)^{1/3} \tag{10}$$

$$d_{max} \simeq \left(\frac{m \cdot v^4}{8K \cdot \rho \cdot \varepsilon^2}\right)^{1/3} \tag{11}$$

b) The time scale for Raleigh-Taylor instabilities $\tau_{R.T.}$. If the matter in the cloud is much denser than that in the surrounding medium a situation will develop at the tip of the cloud in which Raleigh-Taylor type instabilities are likely to occur. In a frame of reference comoving with the cloud we see that in this case the denser gas is supported by the more tenuous gas. If we assume that the latter component, i.e. the medium, has passed through an adiabatic shock before coming into contact with the cloud gas, its density will be 4ρ. The growth time for an

[1] For the sake of numerical simplicity the units $M_\odot$, pc, My (= 10^6 year) were adopted for this section; the following conversion can be used: 1 pc My^{-1} = 1 km s^{-1}; 1 $M_\odot$ pc^{-3} = 40.8 H-atom cm^{-3}; 1 pc^2 My^{-2} ∿120 K for HI, ∿ 60 K for HII.

an R-T instability with a wavelength λ now becomes approximately:

$$\tau_{R\cdot T} = \left(\frac{\lambda}{a}\cdot\frac{\delta\varepsilon + 3v^2}{3v^2 - \delta\varepsilon}\right)^{1/2} \qquad (12)$$

Generally v^2 will be much larger than ε so that we may write:

$$\tau_{R\cdot T} = \left(\frac{\lambda}{a}\right)^{1/2} = \left(\frac{3\lambda\cdot r_{max}}{2\pi\varepsilon}\right)^{1/2} \qquad (13)$$

Though the short-wavelength disturbances grow much faster initially, those with a large λ may be important in the end since they contain more mass. Equating λ to r_{max} we find a value for $\tau_{R.T}$ approximately equal to the sound-crossing time $\tau_s \approx r_{max}\cdot\varepsilon^{-\frac{1}{2}}$:

$$\tau_{R\cdot T} \leq \tau_{R\cdot TM} = r_{max}\cdot\left(\frac{3}{2\pi}\cdot\varepsilon^{-1}\right)^{1/2} = \tau_{stop}\cdot v^{-1}\cdot\left(\frac{2\pi}{3}\cdot\varepsilon\right)^{1/2} < \tau_{stop} \qquad (14)$$

c) The free-fall time τ_{f-f}. If the cloud is compressed to a smaller radius than its Jeans-radius it will collapse under the influence of its self-gravitation. This is the case if the free-fall time to the center of the cloud becomes smaller than the sound-crossing time, or for that matter $\tau_{R.TM}$. The free-fall time is approximately equal to:

$$\tau_{f\cdot f} \approx \left(\frac{\varepsilon}{\rho\cdot v^2\cdot G}\right)^{1/2} \quad ; \quad G = 4.5\ 10^{-3}\ M_\odot^{-1}\ pc^3\ My \qquad (15)$$

d) The heating time τ_{heat}. As the motion of the cloud is slowed by the interaction with the surrounding medium, kinetic energy will be transformed into heat. It is not possible to say what fraction of this energy will be used to heat the cloud, but we can derive a lower limit for the heating time:

$$\tau_{heat} \geq \frac{\varepsilon}{v\cdot a} = \tau_{stop}\cdot v^{-2}\cdot\varepsilon \ll \tau_{stop} \qquad (16)$$

e) The cooling time τ_{cool}. While the cloud is being heated due to the deceleration it is at the same time being cooled by radiation processes. Two different regimes can be distinguished. On the one extreme the cloud can be optically thin at all wavelengths. In this case we can use the cooling coefficients $\Lambda(\varepsilon)$ as presented in the literature (e.g. Dalgarno and McCray, 1972[2]). The cooling rate is proportional to the density in this case. On the other exteme the cloud may be optically thick at all wavelengths. In that case we can use the black-body approximation. The actual cooling time will be longer than that calculated from either assumption.

Since the density in the cloud is very non-uniform and the cooling rate is very much dependent on the density, the cooling of the cloud will be non-uniform and consequently the assumption of a uniform temperature will cease to hold.

For the optically thin case we find:

$$\tau_{cool} = 2.3\ \frac{\varepsilon^2}{\Lambda(\varepsilon)\cdot\rho\cdot v^2} \qquad (17)$$

[2] The cooling curve presented in their Fig.2 must be multiplied by 8 10^{28} in order to conform with the units in this section.

The effective radius for the cloud is not very well defined, but the cooling time for the optically thick case is of the order:

$$\tau_{cool} \approx \frac{B \cdot \rho \cdot v^2}{m \cdot c^4} \quad ; \quad B = 10^{-11}\ pc^9\ M_y^{-5} \qquad (18)$$

3. Consequences

In Fig.2 the effect on the characteristic times of variations in the different parameters of a cloud model are illustrated. The medium density and the velocity

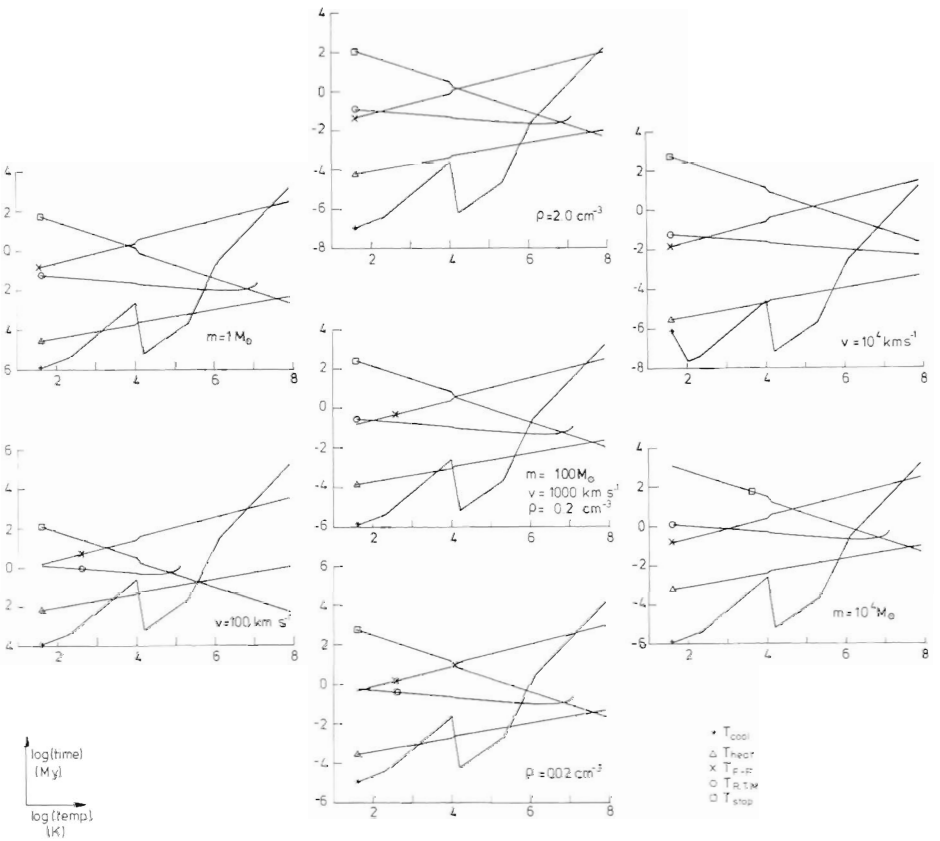

Figure 2.

Characteristic time scales for different model clouds plotted as a function of temperature. For the central graph all relevant parameters are indicated. For each of the others only one parameter was varied with respect to the central graph; this parameter is indicated.

of the cloud have been chosen in the range relevant to NGC 4258; the cloud mass is much smaller than the total mass that must have been ejected. It is evident that in all cases illustrated cooling and heating are the fastest processes. A cloud will be approximately thermally stable in those cases where heating is dominant at the lower temperatures and cooling at the higher. For many clouds in the example this is the case near a temperature of approximately 10000 K, where the cooling rate strongly increases with temperature due to the ionization of the hydrogen, but for the clouds that could be thermally stable at 10000 K the stopping time in the disk medium would be so short that they could not travel the 30 kpc through that medium necessary to create the anomalous arms. If we now turn to the most massive cloud illustrated in Fig.2, which still has a mass that is much smaller than the total mass that would be needed to create the anomalous arms, we see that it has no such stable temperature. It seems unlikely that the ejected clouds are initially very cold--ejection is a violent process--so that they must either heat up after ejection, in which case they will not be able to reach 30 kpc, or cool. In the latter case the strongly diminished internal pressure and small scale Raleigh-Taylor instabilities will lead to a rapid fragmentation of the cloud so that a complex of small cloudlets will be created. The volume of space filled by this complex will not be much smaller than that occupied by the original cloud; the matter in the region will only be less evenly spread. The precise behaviour of such a cloud complex has not been analyzed, but from the behaviour of individual clouds some inferences can be made concerning that of the complex as a whole:

-- Most clouds in the complex will be cold (possibly only slightly warmer than 3 K), though some may have a temperature near 10000 K.

-- The clouds in front will evolve more rapidly than the rest. They will either suffer Raleigh-Taylor instabilities or be gravitationally unstable. In the former case they will rapidly fall apart into even smaller clouds. These clouds will be slowed down quickly and may heat up in the process. However, they may also be overtaken by the bulk of the complex before that can happen and be resorbed in some way. If the clouds collapse their interaction with the medium virtually ceases.

-- The effective cross-section for interaction with the medium encountered by the complex is dependent on too many unknowns to allow an estimate to be made. The expected further fragmentation of the cloudlets--$\tau_{R.TM}$ is always much shorter than τ_{stop}--will help to keep this cross-section comparable to the whole complex surface.

-- The medium will be shock-heated when it collides with a cloud complex. For the velocities relevant in NGC 4258 the temperature attained will generally be so high that the gas will not be able to cool (cf. cooling time for a hot cloud). It will expand and much of it may even be lost to the galaxy.

-- The complex will leave behind a debris of very hot gas and probably also cold clouds.

-- Due to the interaction with the medium the complex will be quite turbulent, so that gravitational instabilities will be counteracted. When, however, the complex leaves the galaxy and the medium becomes more tenuous, gravitational instabilities may become important. Possibly only very low-mass stars will be formed due to the shredding of the cloud as it passed through the disk medium.

-- Pressure effects probably will be unimportant for the expansion or contraction of the complex.

The following conclusions may be drawn:

i. Individual clouds cannot travel sufficiently far through the disk medium and retain a sufficiently large cross-section for interaction with that medium to have created the anomalous arms.

ii. A complex of clouds that collectively tunnel out their path through the disk medium probably can have created the anomalous arms.

iii. The behaviour of the individual clouds is strongly influenced by their membership of the complex.

Reference.

Dalgarno, A.; McCray, R.A.: 1972, *Annual Review of Astronomy and Astrophysics 10*, 375

CHAPTER 7 CONCLUDING REMARKS AND SUGGESTIONS FOR FURTHER RESEARCH

It has been demonstrated in chapters 3 and 4 that in NGC 4258 we probably observe the combined kinematical and morphological effects of an oval structure or *fat bar* and the ejection of a large amount of gas at high velocities from the nucleus. Both of these mechanisms have also been suggested to explain the large deviations from circular rotation observed in several other galaxies, among which is the Galaxy (for a discussión of the features observed in the central region of the Galaxy the reader is referred to Oort, 1977). As for NGC 4258, both mechanisms seem to be responsible for part of the observed features. If, as suggested in chapter 3, section 7, active nuclei in spiral galaxies are often associated with bar-like structures, a very careful study of any galaxy where nuclear activity is suspected is necessary before ascribing deviations from circular rotation to such activity.

NGC 4258 is interesting as a barred spiral for several reasons. Firstly, because the gas motions in the region of the bar can be studied reasonably well due to the large angular size of the galaxy and its favourable inclination. Secondly, because of the strong evidence that at least some of the spiral arm pattern outside the lens lies outside corotation. Though there is no certainty that these arms are actually driven by the bar, it is notable that such a high pattern speed as suggested by the model calculations of Huntley et al. (1978) is indeed found in at least one barred spiral.

For a more detailed study of the region of the bar and of the dynamics of the spiral arms HI line observations with the future 3 km version of the WSRT are indicated. The 5120 channel digital cross-correlator back-end offers the possibility to obtain a good sensitivity even at the higher resolution in far fewer observing days than spent on the observations described in this thesis. In order to obtain as low an overall noise figure as possible an attempt may be made to combine all observations.

The 1.5 km configuration of the WSRT should be used for a morphological study of the anomalous arms in the continuum at 6 cm. The resolution that can be obtained with this configuration should be high enough to obtain a better insight into the shape of the anomalous arms in the central region and to study the relation between the anomalous arms and the plateaux, while the sensitivity is high enough to guarantee detection. The 6 cm continuum data could be combined with 21 cm continuum data obtained with the 3 km configuration to yield a high resolution spectral index map. It is essential that both the 21 cm and the 6 cm data be supplemented with short spacing information derived from well calibrated single dish maps. The spectral index between 6 cm and 21 cm should yield important information concerning the age of the relativistic electrons in the anomalous arms and hence concerning the origin of these electrons.

If, as suggested in chapter 6, compact cold clouds are an important constituent of the anomalous arms, CO emission may be detectable. Since no information is available yet concerning the temperature of these clouds and the effective area covered by them, it is not possible to say at what level this emission might be expected.

In the optical domain a mapping of the excitation parameters of the HII regions in the lens would be interesting in view of the scenario for the behaviour of the anomalous arms sketched in chapter 4. A spectrographic study

of the velocities both of the gaseous and the stellar components is essential for our understanding of the anomalous arms and of the bar. Velocity gradients on a small linear scale are expected to be the most interesting features, so that the observations should be obtained in such a manner that a good spatial resolution ($\sim$7") is obtained in the entire lens and possible systematic errors in the velocities affect these gradients as little as possible.

An attempt to follow the anomalous arms further out from the nucleus may be made by observing NGC 4258 in the high excitation oxygen lines.

In conclusion, it may be stated that the expulsion hypothesis has been strengthened by the data and the analysis presented in this thesis, but that further observations as well as more refined theoretical models still are needed before the puzzle of NGC 4258 may be considered solved.

References.

Huntley, J.M.; Sanders, R.H.; Roberts, W.W.: 1978, *Astrophys. J. 221*, 521

Oort, J.H.: 1977, *Ann. Rev. Astron. Astrophys. 15*, 295

SYNOPSIS

NGC 4258 was already discovered at the end of the eighteenth century by Méchain, but it has become clear only recently that it has some very unusual properties. In 1961 Courtès and Cruvellier reported that on a photograph, obtained in Hα with the aid of a focal ratio reducer, a pair of unique arms were visible, which cut through the normal spiral arms. These so-called anomalous arms contain no young stars that could have ionized the gas; the observed ionization seems to be due to shocks. The anomalous arms are much smoother than the normal arms.

The enormous size and the remarkable properties of the anomalous arms were only fully recognized after the publication in 1972, by Van der Kruit, Oort and Mathewson (KOM), of 21 cm continuum observations obtained with the Westerbork Synthesis Radio Telescope (WSRT). In their map the anomalous arms are the dominant feature in NGC 4258. They extend all the way from the central region to the edge of the galaxy, or approximately 28 kpc (assuming a distance of 6.6 Mpc for NGC 4258). The anomalous arms, which are unresolved in KOM's observations, are associated with extended plateaux of emission. KOM proposed that the anomalous arms were created by the expulsion of matter from the nucleus into the plane of the galaxy.

The aim of the research described in this dissertation was to verify this "expulsion hypothesis". A study has been made both of the more normal aspects of NGC 4258 and of the anomalous arms. Chapter 1 contains a review of the relevant literature. Observations have been obtained of the 21 cm line and continuum emission, both with the WSRT and the 100 m telescope of the Max Planck Institut für Radioastronomie in Bonn. The reduction of these observations is described in chapter 2. Maps of the distribution of the neutral hydrogen and the continuum are presented; an analysis is given in later chapters.

In chapter 3 the normal aspects of NGC 4258 are discussed. This analysis is primarily based on the 21 cm line observations. Very large deviations from circular rotation are observed in the central region, but these do not seem to be associated with the anomalous arms. They can be explained very well by assuming that NGC 4258 is a barred spiral. In this connection it is worth noting that some of the spiral arms lie outside corotation, in good agreement with the theoretically predicted high pattern speeds for bars (Huntley, Sanders and Roberts, 1978). The large, and only partly understood, velocity deviations associated with the bar make it more difficult to recognize and analyze those that might be associated with the anomalous arms. Moreover, it proved that in the 21 cm line the latter type of deviation can not be detected as the anomalous arms contain very little HI.

Therefore the analysis of the anomalous arms, in chapter 4, is based entirely on the 21 cm continuum observations and on the velocity measurements in the Hα line published by Van der Kruit (1974). From the morphology of the anomalous arms it is concluded that, if the anomalous arms were indeed created by expulsion of matter from the nucleus, the expulsion mechanism must closely resemble that in double radio sources. The bi-directionality, the high degree of collimation, the repeated activity and the constancy of the direction of the ejections observed for the double radio sources are also found in NGC 4258; the differences in the appearance of the objects must be attributed to the smaller amount of energy involved in NGC 4258 and especially to the much denser medium encountered by the ejecta. The velocity field observed by Van der Kruit can also be explained very well from the expulsion hypothesis. It is remarkable that the large deviations from circular rotation he observes seem to be associated with

the bar, while the gas in the anomalous arms has more apparently normal velocities. A model is presented that qualitatively reproduces the observations.

The polarization observed in the anomalous arms and the spectrum indicate that the observed emission is due to the synchrotron mechanism. The magnetic field in the anomalous arms, near the rim of the galaxy, is very regular, but not very strong ($\sim 10^{-7}$ G), otherwise no polarization would have been observed.

In chapter 5 methods for the reduction and analysis of HI observations are reviewed. A simple technique for the analysis of the gas flow in a (barred) spiral galaxy is also presented.

Chapter 6 contains a discussion of how the ejected matter in NGC 4258 may have behaved; it is concluded that the ejecta probably condensed into complexes of cold, small clouds as they travelled through the disk medium.

In chapter 7 some suggestions are made for further, mainly observational, research.

References.

Courtès, G.; Cruvellier, P.: 1961, *Compt. Rend. Acad. Sci. Paris 253*, 213

Huntley, J.M.; Sanders, R.H.; Roberts, W.W.: 1978, *Astrophys. J. 221*, 521

Kruit, P.C. van der: 1974, *Astrophys. J. 192*, 1

Kruit, P.C. van der; Oort, J.H.; Mathewson, D.S.; 1972, *Astron. Astrophys. 21*, 169

SAMENVATTING

NGC 4258 is al sedert het eind van de 18^{e} eeuw als object bekend, maar pas gedurende de laatste decennia is het duidelijk geworden dat het stelsel heel bijzondere kenmerken vertoont. In 1961 meldden Courtès en Cruvellier dat op een, met speciale optiek in het licht van de rode waterstoflijn Hα gemaakte, foto een paar unieke armen te zien waren die de normale spiraalstructuur doorsneden. In tegenstelling tot de normale armen bevatten deze z.g. anomale armen geen jonge sterren die verantwoordelijk zouden kunnen zijn voor de ionisatie van het aanwezige gas. Veeleer lijkt schok-ioisatie hiervoor verantwoordelijk. De anomale armen hebben een veel egalere structuur dan de normale armen.

De enorme afmetingen en de opmerkelijke eigenschappen van de anomale armen werden echter pas goed onderkend na de publicatie, in 1972, door Van der Kruit, Oort en Mathewson (KOM) van met behulp van de Westerbork Synthese Radio Telescoop (WSRT) verkregen waarnemingen aan de continuümstraling op een golflengte van 21 cm. Op deze golflengte overheersen de anomale armen het beeld van NGC 4258 geheel. Vanuit het centrale deel strekken ze zich uit tot aan de rand van het stelsel, oftewel zo'n 90.000 lichtjaar. Naar aanleiding van deze waarnemingen stelden KOM hun z.g. expulsie-hypothese op, die de anomale armen verklaart als zijnde het gevolg van de uitstoting met hoge snelheden door de kern van geweldige hoeveelheden gas.

Het in dit proefschrift gerapporteerde onderzoek werd opgezet om deze expulsie-hypothese nader te toetsen. Het is gefundeerd op waarnemingen aan de 21 cm lijn- en continuümstraling, verkregen met de WSRT en de 100 m telscoop van het Max Planck Institut für Radioastronomie te Bonn. Na een overzicht van de literatuur betreffende NGC 4258 (hoofdstuk 1) wordt in hoofdstuk 2 een beschrijving gegeven van de reductie van deze waarnemingen. Kaarten van de verdeling van de neutrale waterstof en de continuümstraling zijn in dit hoofdstuk opgenomen; een analyse wordt in de volgende hoofdstukken gegeven.

In hoofdstuk 3 wordt uitgebreid ingegaan op de normale aspecten van NGC 4258. Deze analyse is vooral gebaseerd op de uit de 21 cm lijn-waarnemingen verkregen gegevens. Het blijkt dat NGC 4258 in het centrale deel zeer grote afwijkingen van cirkelrotatie vertoont, die echter niet met de anomale armen in verband lijken te staan. Ze kunnen evenwel goed worden verklaard door aan te nemen dat NGC 4258 een balkspiraal is; hiervoor zijn ook andere argumenten aan te voeren. Deze verstoring van het snelheidsveld maakt het herkennen en analyseren van verstoringen die wel met de anomale armen in verband staan veel moeilijker. Overigens blijkt de waterstof in de anomale armen steeds grotendeels geioniseerd te zijn, zodat de waarnemingen aan de 21 cm lijn geen informatie over de snelheden in deze armen bevatten.

De analyse van de anomale armen in het vierde hoofdstuk is dan ook uitsluitend gebaseerd op de 21 cm continuümwaarnemingen en op de snelheidsmetingen in de Hα lijn gepubliceerd door Van der Kruit (1974). Het blijkt dat de waarnemingen inderdaad zeer goed te verklaren zijn met de expulsie-hypothese. In de kern van NGC 4258 moeten zich processen hebben afgespeeld die veel overeenkomst vertonen met die in de kernen van de vaak zeer heldere dubbele radiobronnen, zowel wat betreft de sterke gerichtheid, de tweezijdigheid , het zich herhalen en de constante richting van de uitstoting. Het verschil moet gezocht worden in de geringere hoeveelheid energie die is vrijgekomen in NGC 4258 en vooral ook in het veel dichtere medium waar het uitgestoten gas in terecht is gekomen. Het verrassende feit doet zich voor dat die snelheden die het meest afwijken van de zuivere cirkelrotatie in het centrale deel van NGC 4258 waarschijnlijk met de balk in

verband staan, terwijl de snelheden in de anomale armen juist niet zoveel lijken af te wijken. In hoofdstuk 4 wordt tevens een eenvoudig model gepresenteerd, dat qualitatief goede overeenkomst met de waarnemingen vertoont.

In hoofdstuk 5 worden aanwijzingen gegeven voor de analyse en de reductie van HI waarnemingen in het algemeen. Ook wordt een eenvoudige methode gepresenteerd om het gedrag van het gas in een (balk-)spiraal te beschrijven.

Hoofdstuk 6 bevat een beschouwing over het gedrag van de uitgestoten materie in NGC 4258; het blijkt dat het uitgeworpen gas zich waarschijnlijk als een complex van kleine, zeer koude wolkjes een weg heeft gebaand door de schijf.

In hoofdstuk 7 worden enige suggesties gedaan voor verdere waarnemingen.

Referenties.

Courtès, G.; Cruvellier, P.: 1961, *Compt. Rend. Acad. Sci. Paris 253*, 218

Kruit, P.C. van der: 1974, *Astrophys. J. 192*, 1

Kruit, P.C. van der; Oort, J.H.; Mathewson, D.S.: 1972, *Astron. Astrophys. 21*, 169

STUDIE OVERZICHT

Na het behalen van het einddiploma HBS-B aan het Spinoza Lyceum te Amsterdam begon ik in 1968 met de sterrenkunde studie aan de Leidse Universiteit. In september 1971 behaalde ik het candidaats examen sterrenkunde en natuurkunde met wiskunde. Tijdens de doctoraal fase volgde ik onder meer colleges bij Prof. R.G. Conway, Prof. H.C. van de Hulst, Prof. H. van der Laan, Prof. P. Mazur en Dr. Th. Walraven. Van september 1972 tot juli 1974 was ik als student assistent werkzaam aan de Leidse Sterrewacht. Het doctoraalexamen sterrenkunde met theoretische natuurkunde behaalde ik in juni 1974 (cum laude). Van 1 juli 1974 tot 1 juli 1977 was ik in dienst bij Z.W.O.; van 1 januari tot 1 oktober 1978 was ik aangesteld bij de Rijksuniversiteit te Leiden. Gedurende de vier jaar sedert het behalen van mijn doctoraal ben ik bezig geweest met het in dit proefschrift beschreven onderzoek. De volgende scholen en conferenties werden door mij bezocht:

Young European Radio Astronomers' Conference (1973 in Cambridge, England; 1974 in Göteborg, Zweden).

International School of Physics „Enrico Fermi" over „Physics and Astrophysics of Neutron Stars and Black Holes" (1975 in Varenna, Italië).

Sixth Advanced Course van de Swiss Society of Astronomy and Astrophysics over „Galaxies" (1976 in Saas-Fee, Zwitserland).

IAU Symposium No. 77 over „Structure and Properties of Nearby Galaxies" (1977 in Bad Münstereifel, West-Duitsland).

DANKBETUIGING

Allereerst wil ik Dr. W.W. Shane bedanken voor de wijze waarop hij mij heeft begeleid bij het schrijven van dit proefschrift en bij het daaraan ten grondslag liggende onderzoek. Dit heeft hij steeds met veel bekwaamheid en geduld gedaan.

Mijn echtgenote, Petra, heeft me steeds fantastisch geholpen bij het schrijven van dit proefschrift. Het goed verzorgde typewerk is slechts het meest zichtbare deel van haar bijdrage.

Mijn promotor, Prof. H. van der Laan, dank ik voor zijn plezierige en efficiente begeleiding bij het tot stand komen van dit proefschrift.

Prof. J.H. Oort heeft met zijn getoonde belangstelling het onderzoek zeer gestimuleerd.

Van al diegenen die op de één of andere wijze een bijdrage hebben geleverd aan de WSRT waarnemingen noem ik slechts hen die voor mij het meest zichtbaar zijn geweest: J. Brotherhood, B. Doove, Dr. H.W. van Someren-Gréve en Dr. T.A.Th. Spoelstra. De anderen ben ik er niet minder dankbaar om.

Voor de waarnemingen met de 100 m telescoop dank ik het Max Planck Institut für Radioastronomie in Bonn en Dr. R.H. Harten, die niet alleen de waarnemingen, maar ook een groot deel van de reductie ervan heeft verzorgd.

Hulp en begeleiding bij verschillende onderdelen van het onderzoek heb ik gehad van: Dr. E. Bajaja, Dr. E. Dekker, T. Hoekema, Prof. H.C. van de Hulst, Dr. B. van Leer, K.W.C. Lugtenborg, Dr. P.R. Woodward en vele, vele anderen.

Voor de uitstekende en vlotte verzorging van de vele illustraties dank ik J.J. Ober (tekeningen), W.J. Brokaar en L.A. Zuyderduin (fotografie en verkleining en vermenigvuldiging van de tekeningen) en M. Flohr (radio-fotoos).

Het proefschrift werd gedrukt bij Beugelsdijk B.V. te Leiden.

STELLINGEN BEHORENDE BIJ HET PROEFSCHRIFT VAN GEERT DICK VAN ALBADA

1) De grote hoeveelheden gas die de voorste anomale armen in NGC 4258 hebben veroorzaakt zijn waarschijnlijk vrijwel loodrecht op de balk uitgestoten.

2) De in sectie 1.1 van hoofdstuk 5 beschreven waarschijnlijkheidsverdeling $\mu(T_s)$ kan voor NGC 4258 goed worden beschreven door $\exp\{-(T_s/T_{s,o})^{-0.44}\}$.

3) Zelfs grote afwijkingen van cirkelrotatie in spiraalnevels zijn slechts hoogst zelden het directe gevolg van activiteit in de kernen van die nevels.

4) De veronachtzaming van de wet van behoud van zwaartepuntsbeweging ($\Sigma m \cdot \vec{x} - t\Sigma\vec{p} = \vec{Z}$) in bepaalde zogeheten conservatieve gasdynamische rekenschema's duidt op een algemene leemte in het onderricht in de klassieke mechanica.

5) De wijze waarop Kreisler geladen tachyonen trachtte te vinden duidt op een gebrek aan inzicht in de speciale relativiteitstheorie. (M.N. Kreisler: 1973, *American Scientist 61*, 201).

6) De door Barker voorgestelde versie van de theorie van Milne geeft geen aanleiding tot meetbare effecten. (K.D. Barker: 1974, *Astron. Astrophys. 31*, 461, Issue April I).

7) Het vaak ten gunste van de bestudering van de geschiedenis aangevoerde argument dat wij ervan kunnen leren op welke wijze conflicten kunnen worden opgelost of vermeden, is in strijd met de dagelijkse ervaring dat historische argumenten veelal worden gebezigd om conflicten te scheppen of in stand te houden.

8) Ook het Seyfert stelsel 140-G43 is waarschijnlijk een balkspiraal met een „fat bar". (R.M. West; A.C. Danks; G. Alciano: 1978, *Astron. Astrophys. 65*, 151)

9) Het door elkaar gebruiken van M- en NGC-nummers werkt verwarrend. Het verdient aanbeveling M-nummers te gebruiken indien aanwezig, met het NGC-nummer en eventuele andere aanduidingen als toevoeging. Nieuwe catalogi dienen steeds de oude nummering intact te laten.

10) Geometrische bepalingen van de projectie-parameters van spiraalstelsels zijn onbetrouwbaar; spiraalstelsels zijn niet axi-symmetrisch.

Leiden, oktober 1978.